TRANSITION DIPOLE MOMENT AND LIFETIME STUDY OF Na_2 AND Li_2 ELECTRONIC STATES VIA AUTLER-TOWNES AND RESOLVED FLUORESCENCE SPECTROSCOPY

A Dissertation

Submitted to

the Temple University Graduate Board

In Partial Fulfillment

of the Requirements for the Degree of

Doctor of Philosophy

---

by

Aydin Sanli

May, 2017

Examining Committee Members:

Marjatta Lyyra, Advisory Chair, Department of Physics

Nikolaos Sparveris, Department of Physics

Martha Constantinou, Department of Physics

John Huennekens, Lehigh University, Department of Physics

Eric Borguet, Department of Chemistry

ABSTRACT

This dissertation consists of three major studies. The first study, described in Chapter 3, focuses on the experimental work we carried out; experimental study of the electronic transition dipole moment matrix elements (TDMM) for the $5^1\Sigma_g^+ \rightarrow A^1\Sigma_u^+$ and $6^1\Sigma_g^+ \rightarrow A^1\Sigma_u^+$ electronic transitions of the sodium dimer molecule. Here we obtained the electronic transition dipole moments through Autler-Townes and resolved fluorescence spectroscopy and compared them to the theory. The second study, described in Chapter 4, is on sodium dimer ion-pair states. In this work, we calculated the radiative lifetimes and electronic transition dipole moments between Na_2 ion-pair states ($3^1\Sigma_g^+$, $4^1\Sigma_g^+$, $5^1\Sigma_g^+$, $6^1\Sigma_g^+$) and $A^1\Sigma_u^+$ state. This study was published in 2015. The last study, described in Chapter 5, is the total lifetime (bound-bound plus bound-free) and transition dipole moment calculations of the ion-pair electronic states, $(3-6)^1\Sigma_g^+$, of the lithium dimer molecule.

ACKNOWLEDGEMENTS

I would like to express my deepest appreciation to my advisor Professor Marjatta Lyyra for being an amazing mentor throughout my doctorate. She has always been patient, helpful and accessible whenever I needed assistance. Her generosity to give back to the physics community has always impressed and inspired me. I will follow the noble example she set for us and give back to the community whenever the opportunity arises. I would also like to thank to Prof. Lyyra's husband Prof. Benedict Stavis for his hospitality and good company at our usual gatherings at their house.

I would also like to thank to Dr. Ergin Ahmed for his guidance in research and great help in the laboratory. Dr. Ahmed helped me understand the inner workings of various lasers we used and encouraged me to take initiative. I would like to thank our group members Xinhua Pan for her collaboration and cooperation and Sam Beecher for his assistance with my computational work. Thank you Dr. Metz for your guidance throughout the thesis preparation process. I would like to thank my committee members Prof. Martha Constantinou, Prof. Nikolaos Sparveris, Prof. Eric Borguet and Prof. John Huennekens for taking their time and giving feedback on my dissertation.

TABLE OF CONTENTS

LIST OF TABLES

LIST OF FIGURES

CHAPTER 1

INTRODUCTION

Diatomic molecules have a more complicated structure than atoms. In addition to their translational motion, rotational and vibrational degrees of freedom are involved. A diatomic molecule can rotate as a whole about an axis passing through the center of gravity and perpendicular to the line joining the nuclei (internuclear axis). The atoms can vibrate relative to each other along the internuclear axis [1]. Due to this fundamental difference between atoms and diatomic molecules, one cannot use the atomic model to explain the behavior of diatomic molecules.

The focus of the research described here involves analyzing and extracting information on alkali dimer molecules such as lifetimes, transition dipole moment matrix elements, Einstein coefficients, Franck-Condon factors etc. by using both computational and experimental methods. The key motivating factor here is the effect of the interaction of the ion-pair Coulomb potential energy curve on other electronic states. At small internuclear distance the potential energy curves of the alkali dimers exhibit parabolic behavior. As the internuclear distance increases, the interaction with the ion-pair Coulomb potential causes the formation of shoulders and additional wells in the potential energy curves which in return drastically changes the overlap integrals of the wavefunctions belonging to the upper and lower states. In addition, the transition dipole moment matrix elements and the lifetimes of the electronic states show abrubt changes around shoulders and additional wells. Figure 1 shows some of the electronic potential

energy curves of the sodium dimer molecule. The red dashed line is the Coulomb interaction potential, which affects the $3^1\Sigma_g^+$, $4^1\Sigma_g^+$ and $5^1\Sigma_g^+$ electronic states of Na_2.

Alkali dimer molecules have been actively studied by both theoretical and experimental physicists due to several reasons. The atoms forming these molecules have only one electron in the valence shell and these molecules can be treated as two-electron systems which makes them easier to model compared to other molecules. Alkali dimer molecules form in an alkali vapor which is easy to produce. Their electronic states can be probed by excitation with tunable dye, Ti: Sapphire, and diode lasers because the transitions are within the visible or near-infrared spectral regions. Since alkali dimers are ideal simple models for theoretical and experimental studies, the data regarding the molecular constants such as lifetimes, transition dipole moment matrix elements and Einstein coefficients can be extracted for various states. However, determining the experimental and computational data for states with multiple wells caused by the interaction with the ion-pair Coulomb potential is a challenging process. There is simply not enough information to obtain spectroscopic constants for those states [2]. With this motivation, we have carried out a computational study on the transition dipole moment values as a function of internuclear distance for the $(3,4,5,6)^1\Sigma_g^+ \rightarrow A^1\Sigma_u^+$ transitions of the Na_2 molecule [3]. This computational work on sodium dimer electronic states was largely focused on radiative lifetimes associated with bound-bound transitions. For the Li_2 molecule, we have calculated the spectroscopic constants for bound- bound and bound-free transitions for the $(3,4,5,6)^1\Sigma_g^+ \rightarrow A^1\Sigma_u^+$ systems. Besides the computational work, we have also carried out an experimental study on the transition dipole moment

functions for the $5^1\Sigma_g^+ \rightarrow A^1\Sigma_u^+$ and $6^1\Sigma_g^+ \rightarrow A^1\Sigma_u^+$ electronic transitions of the sodium dimer molecule and compared the experimental results to the theory from the literature.

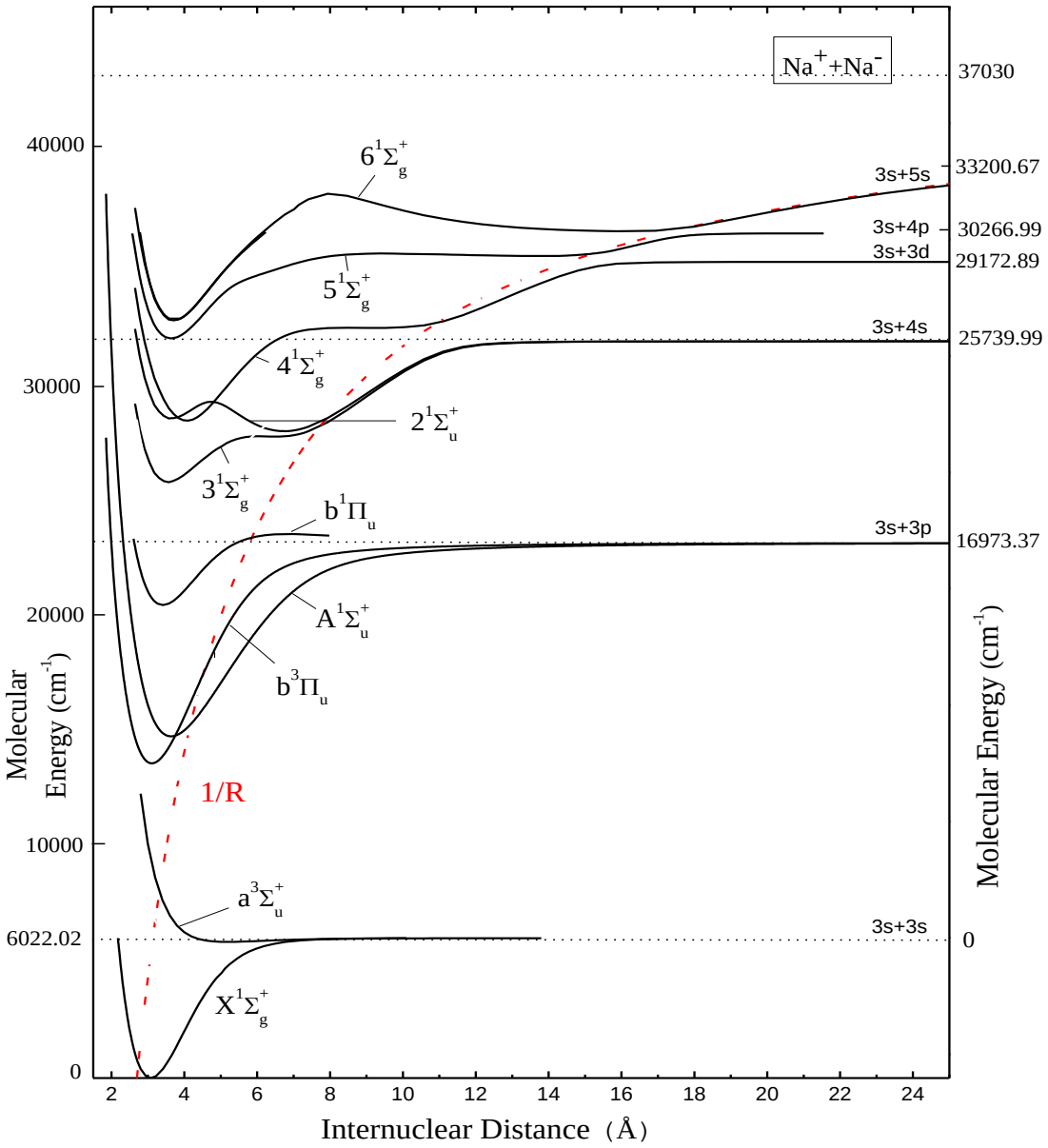

Figure 1.1 Selected potential energy curves of the Na_2 molecule. The dotted line is the ion pair $Na^+ + Na^-$ Coulomb interaction function $e^2/(4\pi\varepsilon R)$, which crosses the region of the electronic states of the neutral molecule and causes the secondary wells and shoulders to these potential energy functions. The potential energy curves are taken from references [4-14].

References

[1] G. Herzberg, Spectra of Diatomic Molecules, 1966.

[2] L. L. Magnus, Perturbation-Facilitated Optical-Optical Double Resonance Studies of NaK, Physics, Lehigh University, 2005.

[3] A. Sanli, B. Beser, J.R. Edwardson, S. Magnier, E.H. Ahmed, A. Marjatta Lyyra, Electronic transition dipole moment and radiative lifetime calculations of sodium dimer ion-pair states, The Journal of Chemical Physics 143 (2015) 104304.

[4] O. Babaky, K. Hussein, Canadian Journal of Physics 67 (1989) 912-918.

[5] V.S. Ivanov, V.B. Sovkov, L. Li, The Journal of Chemical Physics 118 (2003) 8242-8247.

[6] P. Qi, J. Bai, E. Ahmed, A.M. Lyyra, S. Kotochigova, A.J. Ross, C. Effantin, P. Zalicki, J. Vigue, G. Chawla, R.W. Field, T.J. Whang, W.C. Stwalley, H. Knoeckel, E. Tiemann, J. Shang, L. Li, T. Bergeman, Journal of Chemical Physics 127 (2007).

[7] P. Kusch, M.M. Hessel, Journal of Chemical Physics 68 (1978) 2591-2606.

[8] E. Tiemann, Z. Phys. D-Atoms Mol. Clusters 5 (1987) 77-82.

[9] C.C. Tsai, T.J. Whang, J.T. Bahns, W.C. Stwalley, Journal of Chemical Physics 99 (1993) 8480-8488.

[10] S. Magnier, P. Millie, O. Dulieu, F. Masnouseeuws, Journal of Chemical Physics 98 (1993) 7113-7125.

[11] C.C. Tsai, J.T. Bahns, H. Wang, T.J. Whang, W.C. Stwalley, Journal of Chemical Physics 101 (1994) 25-30.

[12] C.C. Tsai, J.T. Bahns, W.C. Stwalley, Journal of Chemical Physics 100 (1994) 768-774.

[13] C.C. Tsai, J.T. Bahns, W.C. Stwalley, Journal of Molecular Spectroscopy 167 (1994) 429-436.

[14] T. Laue, P. Pellegrini, O. Dulieu, C. Samuelis, H. Knockel, F. Masnou-Seeuws, E. Tiemann, European Physical Journal D 26 (2003) 173-185.

CHAPTER 2

THEORETICAL BACKGROUND

2.1 The Born-Oppenheimer Approximation

The total energy of a molecule (neglecting spin and magnetic interactions) consists of the potential and kinetic energies of the electrons and the potential and kinetic energies of the nuclei. The nonrelativistic Hamiltonian of a diatomic molecule is expressed as

$$\hat{H} = \frac{\hbar^2}{2}\sum_{\alpha=1,2}\frac{1}{M_\alpha}\nabla_\alpha^2 + \frac{\hbar^2}{2m_e}\sum_{i=1}^{N}\nabla_i^2 + \sum_i\sum_{j>i}\frac{e^2}{4\pi\pi_o r_{ij}} + \sum_\alpha\sum_i\frac{Z_\alpha e^2}{4\pi\pi_o R_{\alpha i}} + \frac{Z_1 Z_2 e^2}{4\pi\pi_o R_{12}}, \qquad (2.1)$$

$$\hat{H} = \hat{T}_N(\boldsymbol{R}) + \hat{T}_e(\boldsymbol{r}) + \hat{V}_{ee}(\boldsymbol{r}) + \hat{V}_{eN}(\boldsymbol{r},\boldsymbol{R}) + \hat{V}_{NN}(\boldsymbol{R}) \text{ [1].} \qquad (2.2)$$

Here $\boldsymbol{R}$ stands for the nuclear coordinates and $\mathbf{r}$ is for the electronic coordinates.

$\hat{T}_N$ = kinetic energy operator of all the nuclei

$\hat{T}_e$ = kinetic energy operator of all the electrons

$\hat{V}_{ee}$ = potential energy operator for electron-electron Coulomb interaction

$\hat{V}_{eN}$ = potential energy operator for Coulombic interaction of all electrons and all nuclei

$\hat{V}_{NN}$ = Coulombic repulsion between nuclei [1]

The total nonrelativistic Hamiltonian in Eqn. 2.2 cannot be separated into nuclear and electronic parts because the $\hat{\mathrm{V}}_{\mathrm{eN}}(\boldsymbol{r},\boldsymbol{R})$ term depends on both nuclear and the electronic coordinates. The Born-Oppenheimer approximation relies on the fact that the nuclei are massive compared to the size of the electrons and their speed is negligible compared to the electrons [2]. Hence they can be assumed to be stationary relative to the motion of the electrons and thus the $\boldsymbol{R}$ coordinate is fixed and the nuclear and electronic wavefuctions can be separated as $\Psi(r,R) = \psi(r)\kappa(R)$. When the nuclei are fixed, the nuclear kinetic energy term $\hat{\mathrm{T}}_{\mathrm{N}}(\boldsymbol{R})$ can be neglected. Thus, for a fixed nuclear configuration Eqn. (2.2) can be written as

$$\hat{\mathrm{H}}_{el} = \hat{\mathrm{T}}_{\mathrm{e}}(\boldsymbol{r}) + \hat{\mathrm{V}}_{\mathrm{ee}}(\boldsymbol{r}) + \hat{\mathrm{V}}_{\mathrm{eN}}(\boldsymbol{r},\boldsymbol{R}). \tag{2.3}$$

The $\hat{\mathrm{V}}_{\mathrm{NN}}(\boldsymbol{R})$ term in the new Hamiltonian is left out since it is merely a constant now. It shifts the eigenvalues a constant amount. The Schrodinger equation can be written as a combination of electronic and nuclear parts as $(\hat{\mathrm{H}}_{el} + \hat{\mathrm{V}}_{\mathrm{NN}})\,\Psi(r,R) = E_{el}\psi(r,R)$, and the total wavefunction can be written as a product of electronic and nuclear wavefunctions as follows:

$$\Psi(r,R) = \psi_{el}(r,R)X_N(R). \tag{2.4}$$

2.2 Rotational and Vibrational Energies

For diatomic molecules, the symbols used to describe the momentum of the system are different from those used to describe atoms. For atoms, L is the total angular momentum and is conserved, whereas for diatomic molecules Λ, the projection of the total angular momentum on the internuclear distance, is conserved and taken as a reliable quantum number. The rotation perpendicular to the internuclear axis and the vibration along the internuclear axis can be handled separately. The Hamiltonian in Eqn. (2.1) can be separated into radial and rotational parts. The simplest model to describe the rotational energy of a diatomic molecule is the rigid rotor, where two atoms are assumed to be connected by a massless rigid rod. The rotational energy of this system is

$$E_{rot} = \frac{L^2}{2I}. \tag{2.5}$$

Where L is the angular momentum and I is the moment of inertia of the system. The internuclear distance between the atoms, R, is assumed to be constant in a rigid rotor, hence the derivative of the wavefunction with respect to internuclear distance, $\frac{\partial \Psi}{\partial R}$, vanishes in the Hamiltonian and the rotational energy of a diatomic molecule with rigid connection between the atoms can be found as follows :

$$E_{rot} = \frac{\hbar^2 (J)(J+1)}{2I}. \tag{2.6}$$

Here, $\frac{\hbar^2}{2I}$ is known as the rotational constant B_e in energy units. The spacing between the rotational levels is inversely correlated to the reduced mass of the system, μ, and is directly proportional to the second power of *J* which means that the spacing between the successive rotational levels increases as *J* increases and the spacing gets smaller (see Figure 2.1) for heavier molecules.

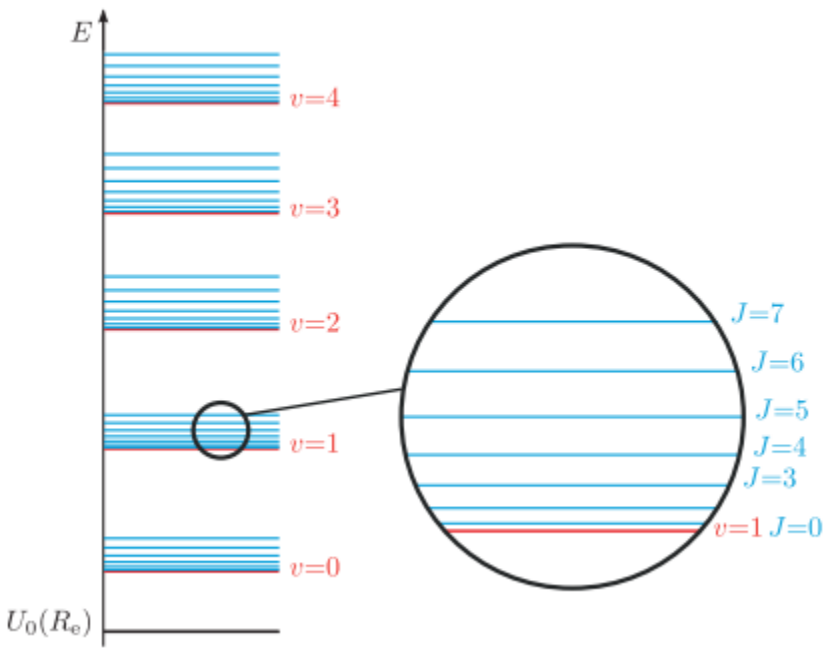

Figure 2.1 Vibrational and rotational energy level spacing of a diatomic molecule.

A model for a diatomic molecule that is a better than a rigid rod is a massless spring allowing the rotor to stretch as well as rotate. In this case, the rotational energy of the system can be described as

$$F(J)= \frac{E_{rot}}{hc} = B_e(J)(J+1)+D_e[J(J+1)]^2 \ldots \tag{2.7}$$

D_e is known as the centrifugal distortion constant [2-4]. In spectroscopy, the default unit we use is wavenumbers, cm^{-1}.

For the solution of the vibrational energy component of the total Hamiltonian, the ideal initial model is the simple harmonic oscillator. The potential of the energy function of the harmonic oscillator is

$$\mathrm{V}(R) \cong \mathrm{V}(r_{\mathrm{e}}) + \frac{1}{2}\mathrm{k}(R - R_e)^2. \tag{2.8}$$

The vibrational energy values of the harmonic oscillator are defined as follows:

$$\mathrm{G}_v = \omega_{\mathrm{e}}(v + \frac{1}{2}) \ . \tag{2.9}$$

The harmonic oscillator is the simplest prototype to define the vibrational energy levels of a diatomic molecule. For higher vibrational levels, the harmonic oscillator model is unable to define the energy levels of the system accurately [3]. A more complicated prototype that serves the purpose is called an anharmonic oscillator with extra terms in the potential. Since the potential energy of the system is the Taylor expansion of the potential energy around the equilibrium point, R_e, adding more terms from the Taylor expansion to the potential energy yields more generalized energy term values as follows:

$$\mathrm{G}_v = \omega_{\mathrm{e}}\left(v + \frac{1}{2}\right) - \omega_{\mathrm{e}}\mathrm{x}_{\mathrm{e}}(v + \frac{1}{2})^2 + \omega_{\mathrm{e}}\mathrm{y}_{\mathrm{e}}(v + \frac{1}{2})^3 + \ldots \tag{2.10}$$

Figure 2.2 shows the difference between the vibrational energy levels of a harmonic and an anharmonic oscillator (Morse potential). The vibrational spacing between two

successive states is the same for a harmonic oscillator whereas for anharmonic oscillator the spacing gets smaller as v increases.

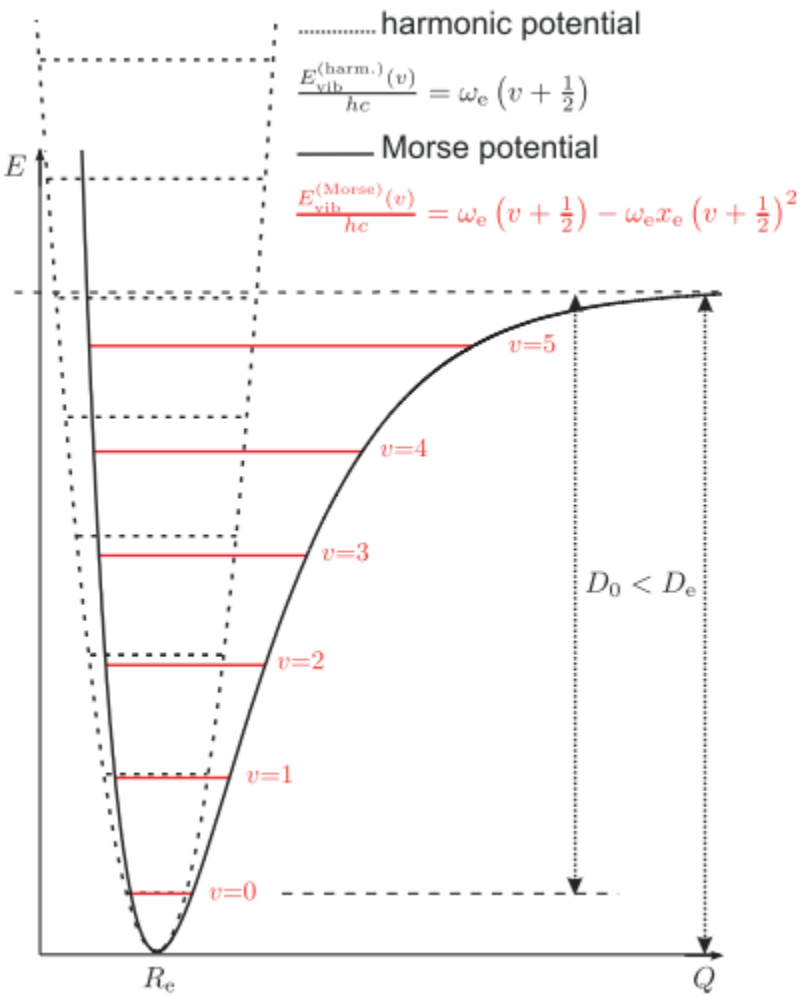

Figure 2.2 Vibrational energy levels of a harmonic oscillator versus those of an anharmonic oscillator (Morse potential).

The rotational and vibrational energies can be combined under a generalized formula (known as Dunham's formula [5]) which defines the total energy of a diatomic molecule as in Equation 2.11,

$$T_{v,J} = \sum_{l,k} Y_{lk}(v+\frac{1}{2})^{l} J^{k}(J+1)^{k} . \tag{2.11}$$

In this formula the Y_{l0} constants represent the pure vibrational terms, Y_{0k} constants are pure rotational terms and mixed terms are the ro-vibrational terms.

$Y_{00} = T_e$ is the electronic minimum potential when there is no rotation. The vibrational energy formula 2.10 is not zero when the vibrational level takes the minimum value 0. The total energy of the system is defined in reference to the minimum of the potential energy curve. T_e is an addition to the zero-point energy and must be included in the formula [2, 3, 5]. The first three pure vibrational, rotational and rovibrational coefficients are related to the spectroscopic constants as follows [5]:

$$Y_{10} \sim \omega_e \; ; \; Y_{20} \sim -\omega_e x_e \; ; \; Y_{30} \sim \omega_e y_e$$

$$Y_{01} \sim B_e \; ; \; Y_{02} \sim -D_e \; ; \; Y_{03} \sim F_e$$

$$Y_{11} \sim \alpha_e \; ; \; Y_{12} \sim -\beta_e \; ; \; Y_{21} \sim \gamma_e \tag{2.13}$$

Where Y_{i0} terms are the vibrational constants, Y_{0i} terms are the rotational constants and the mixed terms, Y_{ik}, are the rovibrational constants.

2.3 Coupling of Angular Momenta and Hund's Cases

A diatomic molecule has in general three angular momenta: electronic orbital angular momentum **L**, electronic spin angular momentum **S**, and nuclear rotation angular momentum **R**. They couple together to form the total angular momentum **J**. Nuclear spin angular momentum **I**, if present, usually couples to **J** to form **F**, but this coupling is ignored in this study. In general, **J** is conserved while **L**, **S**, and **R** are not conserved. We consider the limit **J** >> **L**, **S**, where angular momentum addition can be treated semiclassically.

The rotation of the molecule affects the interactions. Hund was the first to examine this phenomenon, and he introduced various limiting-case models [6] as described in Table 2.1. Table 2.1 shows five limiting coupling cases (Hund's cases (a)-(e)) for a given value of J at a fixed internuclear separation R. The results pertain to bound states of a molecule as well as to two atoms 'in collision' [7].

Every molecular state approaches an atomic limit for large internuclear distances as the molecule dissociates. Taking into account the dominant factors and leaving out the negligible ones, one can determine accurately to which atomic limit the molecular state belongs. In other words, Hund's coupling cases give us a road map to determine the correlation diagrams between the atomic and molecular states.

For the motion of the electrons in an atom, the constant of motion is **L**, so **L** is conserved if the spins are neglected. For molecules, **L** is not a constant of motion and it is not conserved. There is only axial symmetry for diatomic molecules and the projection of the total momentum J on the internuclear axis (Ω) is a good quantum number and is conserved. Omega, Ω, is defined as the sum of the projections of the spin angular

momentum (**S**) and the orbital angular momentum on the internuclear axis. The notation of electronic states and quantum numbers for atoms is parallel to that of diatomic molecules but the quantum numbers that are conserved are different for diatomic molecules [2]. There are 6 Hund's cases and they are categorized according to the type of coupling of angular momenta. Hund's case (a), (b) and (c) are the most important ones for our research.

In Hund's coupling case (a) the coupling of the electronic motion to the internuclear axis is strong. V_{el} as shown in Table 1 is the dominant potential. Hund's case (a) is valid for small internuclear separations and small rotational quantum numbers.

S and **L**, in this case, precess around the internuclear axis rapidly and couple to the line joining the two atoms rather than coupling strongly with each other. The orbital angular momentum component (**Λ**) and the spin angular momentum component (**Σ**) along the internuclear axis are defined as Λ=$|M_L| = 0,1,2,3 \ldots$; Σ = -S,-S+1,...S-1,S, respectively. The total angular momentum along the line connecting two atoms is defined as follows:

$$\Omega = |\Lambda + \Sigma| = |\Lambda - S|, |\Lambda - S| + 1, \ldots, \Lambda + S. \tag{2.14}$$

In Hund's case (b) the coupling of the spin angular momentum to the internuclear axis is weak**. L**, on the other hand, is coupled strongly to the internuclear axis. Hund's case (c) applies to heavy molecules. Spin-orbit coupling (**S** coupling to **L**) far outweighs the coupling of either **S** or **L** to the internuclear axis. The first four common Hund's cases diagrams are shown in Figure 2.3.

Table 2.1 The categorization of Hund's coupling cases according to electrostatic, spin-orbit, and rotational energy strengths [7].

Hund's Coupling Case	V_{el}	V_{so}	V_{rot}
a	strong	intermediate	weak
b	strong	weak	intermediate
c	intermediate	strong	weak
d	intermediate	weak	strong
e	weak	intermediate	strong
e′	weak	strong	intermediate

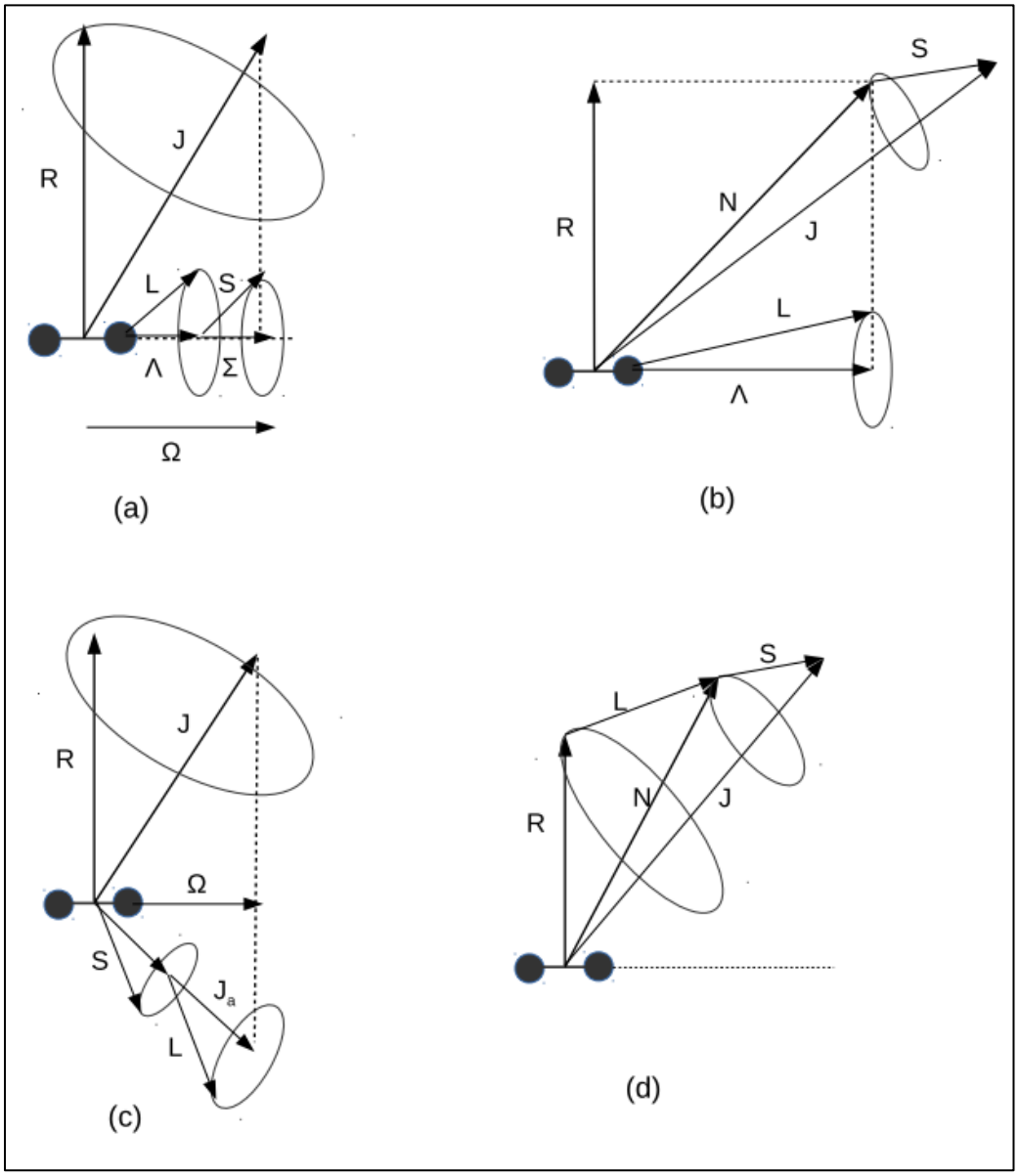

Figure 2.3 Hund's coupling cases (a), (b), (c) and (d). Figure is from Ref. [8].

2.4 Rydberg-Klein-Rees (RKR) Method Properties

The Rydberg-Klein-Rees method is a common procedure to obtain the potential energy curve of a diatomic molecule using the information of vibrational energy levels G_v, and the rotational constants B_v [9]. The analytical expression for the energy levels of a vibrating rotor is obtained by first-order semiclassical quantization via WKB (Wentzel-Kramers-Brillouin) formula [4] :

$$(2\mu/\hbar^2)^{\frac{1}{2}} \int_{R^-(E)}^{R^+(E)} \sqrt{E - V(R)}\ dR = (v + \tfrac{1}{2})\pi \tag{2.15}$$

The R^- and R^+ stand for the inner and the outer turning points of the potential energy curve of a diatomic molecule at energy E as shown in Figure 2.4. The approximate wavefunction according to this can be found as:

$$\psi = Aexp\ (\mp i \left(2\mu/\hbar^2)^{\frac{1}{2}}\right) \int_{R-}^{R+} \sqrt{E - V(R)}\, dR. \tag{2.16}$$

The analytical Dunham formula for the rovibrational energy, defines the energy levels of this solution as follows [4, 5]:

$$E_{v,J} = \sum_{l,k} Y_{lk} (v + \tfrac{1}{2})^l J^k (J + 1)^k\ . \tag{2.17}$$

The WKB quantization in equation (2.15) can be manipulated [4] to give two equations involving the inner and outer turning points:

$$R^{+} - R^{-} = \sqrt{2\hbar^2/\mu} \int_{v_{min}}^{v} \frac{dv'}{G(v) - G(v')}$$

$$\frac{1}{R-} - \frac{1}{R+} = \sqrt{8\mu/\hbar^2} \int_{v_{min}}^{v} \frac{B_{v'} dv'}{G(v) - G(v')} \tag{2.18}$$

The RKR potential represents the internuclear distance range for which there is spectroscopic data resulting for the Dunham fit of coefficients.

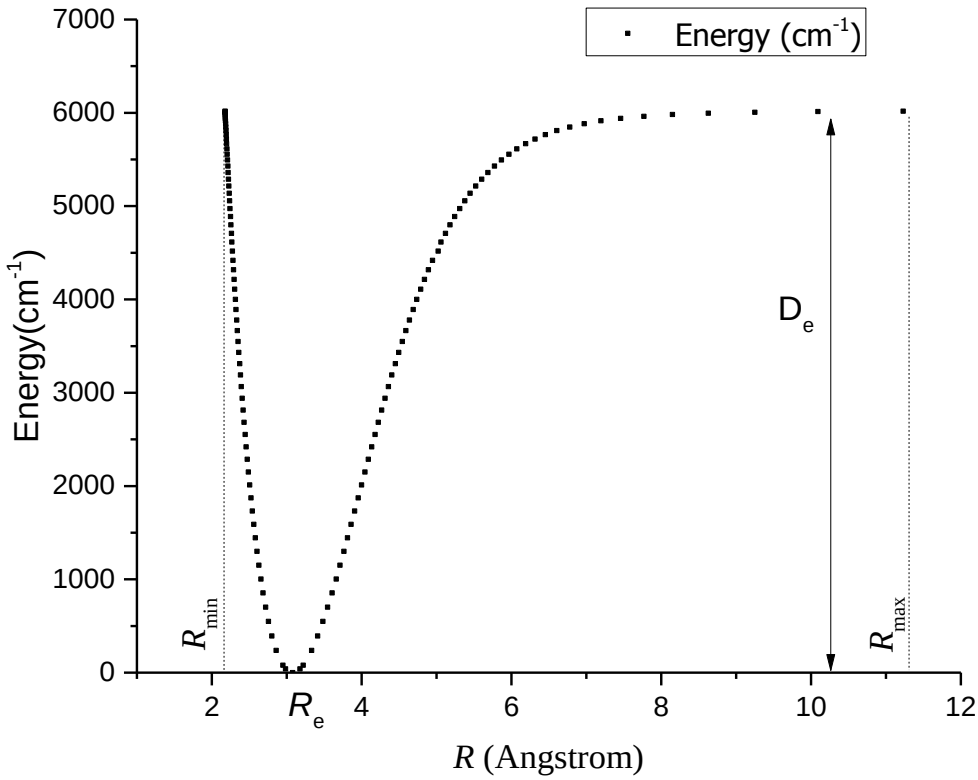

Figure 2.4 Potential energy curve of the $X^1\Sigma_g^+$ ground state [10] of Na_2 diatomic molecule. D_e is the dissociation energy, R_e is the equilibrium position.

2.5 Calculation of Molecular Properties with LEVEL 8.0

In our computational work, we heavily relied on Le Roy's [11] LEVEL 8.0 program to calculate transition dipole moments, Einstein coefficients and Franck-Condon factors. Using the Einstein coefficients we also calculated the lifetimes for sodium and lithium dimer molecular electronic states. Le Roy's LEVEL 8.0 can be used to solve numerically the radial Schrodinger Equation (Eqn. 2.19).

$$-\frac{\hbar^2}{2\mu}\frac{d^2\psi_{v,J}(R)}{dr^2} + V_J(R)\psi_{v,J}(R) = E_{v,}\psi_{v,J}(R) \quad . \tag{2.19}$$

Here $V_J(r)$ is the sum of rotationless electronic potential and the centrifugal term [11]. The centrifugal potential has the form of $\left[J(J+1) - \Omega^2\right]\hbar^2/2\mu r^2$. Omega ($\Omega$) represents the projection of the total electronic angular momentum on the internuclear axis R between the atoms of a diatomic molecule. RKR potential energy functions are input to the program to calculate corresponding rovibrational wavefunctions. The RKR potentials are available in the literature or they can be obtained using the RKR program. The "CHARGE" parameter in the LEVEL 8.0 input file defines the total charge on the molecule. If the molecule is neutral, this parameter is set to zero. NUMPOT is the number of potentials used for the calculations. LEVEL works for a single potential curve as well as multiple potentials to calculate different parameters. For a single curve, LEVEL determines the energy levels of a single potential. For two curves, on the other hand, it calculates the transition dipole moment matrix elements, Franck-Condon factors and Einstein coefficients. The VLIM parameter in the LEVEL input file tells the program the energy approached at the dissociation limit. The RKR potential energy curves do not always cover the full internuclear axis up to the dissociation limit. By default, LEVEL interpolates over the missing regions and calculates the remaining levels up to energy set by the VLIM parameter. One can define a couple of data points close to the dissociation limit for the LEVEL program to extrapolate. But whether the LEVEL program extrapolates to the dissociation level as a linear curve or as a polynomial of third order causes differences in the calculation of final energy levels and molecular parameters. Defining the dissociation limit and the behavior of the potential energy function accurately is crucial to obtain the correct results. One can use a custom polynomial to

define the type of extrapolation. For inverse potential extrapolation, for instance, one can use Eqn. 2.20 by defining the CNN and NCN values.

$$V(R) \propto VLIM - CNN/R^{NCN} \tag{2.20}$$

For inverse-power extrapolation (for $NCN > 0$), NCN coefficient specifies the limiting inverse-power behavior. CNN coefficient (when $CNN \neq 0$) causes the leading inverse-power coefficient to be fixed at the read-in value rather than be determined from a fit to the outmost turning points.

2.6 Autler-Townes Effect and Related Simulations

Autler-Townes effect is also known as the dynamic (AC) Stark effect. It can be observed when one of the two levels involved in the transition is coupled to a third one by a strong field [12]. For a three-level cascade system as shown in Figure 2.5, the probe laser (L_1), is scanned while the strong coupling laser (L_2) stays on resonance. As a result, a splitting is observed (Figure 2.6) in absorption/emission the spectra. The peak-to-peak separation in the spectra is the Rabi frequency (Ω).

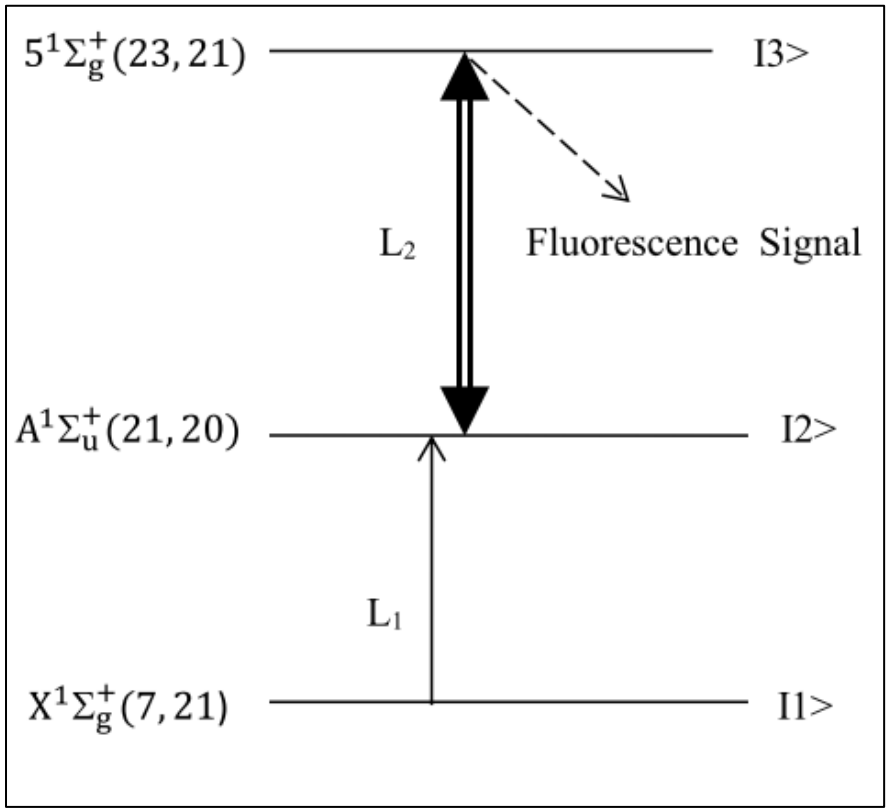

Figure 2.5 Autler-Townes cascade scheme for the $5^1\Sigma_g^+(23,21) \leftarrow A^1\Sigma_u^+(21,20) \leftarrow X^1\Sigma_g^+(21,20)$ transition.

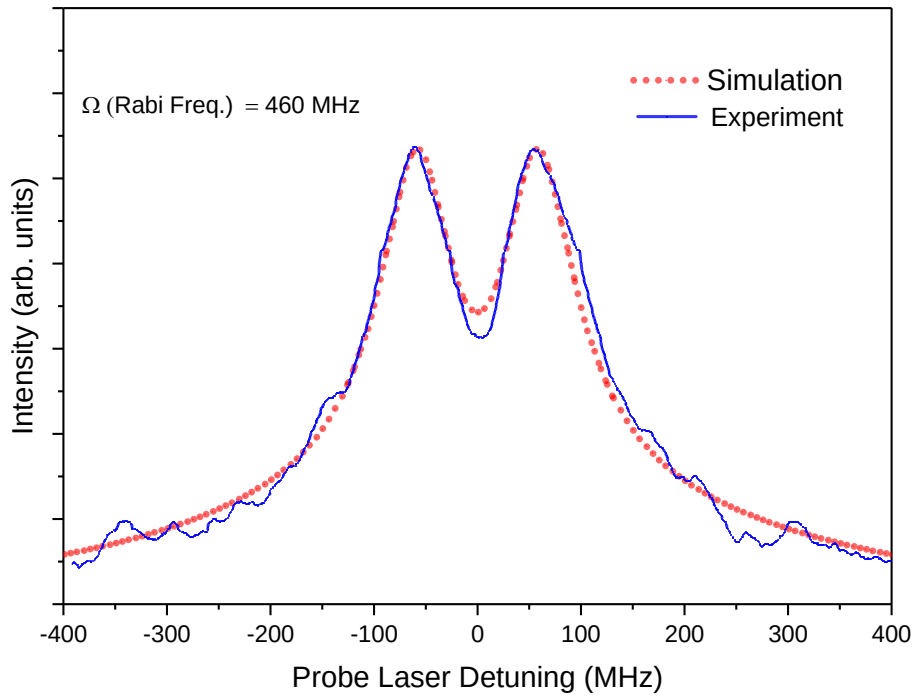

Figure 2.6 Autler-Townes splitting spectra for the $5^1\Sigma_g^+(23,21) \rightarrow A^1\Sigma_u^+(21,20)$ transition of Na_2.

The goal of an Autler-Townes experiment is to determine the Rabi frequency (Ω), a measure of the peak to peak splitting, from the Autler-Townes spectra. This information is then used to obtain the absolute dipole moment matrix element of the transition. Once the experimental splitting spectrum is obtained, a simulation is run and parameters are adjusted to match the experimental splitting. The Rabi frequency is defined as follows:

$$\Omega = \frac{\boldsymbol{\mu E}}{\hbar} \tag{2.21}$$

Here $\boldsymbol{\mu}$ stands for the transition dipole moment matrix element. The Rabi frequency (Ω) of the coupling transition is found through the experiment by matching the peak-to-peak separation of the simulation with that of the experiment. The AT splitting program [13] solves the density matrix equations (Eqn. 2.22) of motion.

$$\frac{\partial \rho}{\partial t} = -\frac{i}{\hbar}[H, \rho] + \Gamma(\rho) + \textit{relaxation terms} \tag{2.22}$$

The Hamiltonian in the interaction picture for this simple three level system (containing a pump and a coupling transition) is as follows:

$$H_I = \hbar\Delta_1|2\rangle\langle 2| + \hbar(\Delta_1 + \Delta_2)|3\rangle\langle 3| + \hbar\frac{\Omega_1}{2}(|2\rangle\langle 1| + |1\rangle\langle 2|) + \hbar\frac{\Omega_2}{2}(|3\rangle\langle 2| + |2\rangle\langle 3|) \tag{2.23}$$

where Ω_i stands for the Rabi frequency $\Omega_i \equiv \frac{\mu_{i,i+1}E_i}{\hbar}$ for the ith laser with

$$\mu_{i,i+1} = < \psi_{v_{i+1}J_{i+1}}|\mu_e(R)|\psi_{v_iJ_i} >. \tag{2.24}$$

Ω_2 is the Rabi frequency of the transition between second and the third level, $|2 > \rightarrow |3 >$.

The total Hamiltonian for the system in Eqn. (2.23) represents the combination of the Hamiltonian for the isolated molecule and the Hamiltonian for the interaction between the molecule and the external electromagnetic field. The dipole interaction here is between the molecule and the electric field component of the laser radiation $\mathbf{E}(\mathbf{r}, t) = E\hat{e}\cos(\mathbf{kr} + \omega t)$.

To simulate our results we used a computer program, written by Dr. Teodora Kirova, for open molecular systems [13]. The program parameters are the Rabi frequencies of the lasers, the spot sizes of the laser beams, the rotational and vibrational quantum numbers of the energy levels involved, the decay rates to lower states, and the wavenumbers corresponding to the wavelengths of the lasers. Among these parameters in Dr. Kirova's AT splitting simulation program, the dominant factors are the spot sizes for the laser beams (measured by using the razor blade technique [14, 15], and the laser powers. These two parameters change the Rabi frequencies significantly for the probe and coupling lasers. The Rabi frequency of the coupling laser is critical since it affects the line shape of the simulation drastically. The decay rates and collisional parameters do affect the wings and shoulders of the AT line shape but do not have a significant effect on the peak to peak separation. Some other parameters used in the AT simulation program are transition energies ($\nu_{31,}, \nu_{53,}\ \nu_{34,}$) in wavenumbers ($cm^{-1}$), rotational ($J$) and vibrational numbers (v) of the transitions, beam diameter of the pump laser (2w) and the projection of the total angular momentum on the internuclear axis (Λ), which defines the types of the various electronic states. In AT splitting spectra, the dominant factors which affect the splitting most are the Rabi frequency of the coupling laser (L_2 in a two laser system) and the focusing of the pump laser [16].

The Rabi frequency of the coupling laser transition depends on the electric field amplitude of the coupling laser and the transition dipole moment matrix element, $\mu_{i,i+1} = < \psi_{v_{i+1}J_{i+1}} | \mu_e(R) | \psi_{v_iJ_i} >$ where $\mu_e(R)$ stands for the electronic component of the transition dipole moment as a function of the internuclear distance R. The AT splitting simulation program solves the total Hamiltonian in Equation (2.23) and

simulates the AT line shape. Then the Rabi frequency setting for the coupling laser is adjusted until the simulation meets the experimental line shape. Having obtained the experimental Rabi frequency one can extract the absolute transition dipole moment matrix element for the coupling laser transition from the relation $\Omega_{23} \equiv \frac{\mu_{23} E_{L_2}}{\hbar}$ [17]. The electric field amplitude is a function of the laser power and for a given laser power value the electric field amplitude of the laser is given by the relation $\mathrm{E} = \sqrt{\frac{4\mathrm{P_{L2}}}{\pi c \varepsilon_0 \mathrm{w}^2}}$, where w is the beam waist of the laser beam defined at the $1/e^2$ points of the Gaussian beam profile and $\mathrm{P_{L_2}}$ denotes the coupling laser power.

2.7 Calculation of Lifetimes with BCONT 2.2

The program LEVEL 8.0 can be used to calculate the Einstein coefficients for the bound-bound part of the electronic transitions. The LEVEL program cannot calculate the Einstein coefficients for bound-free transitions.

For $\mathrm{Li_2}$ molecule electronic states, the transitions corresponding to the higher v values are mostly bound-free. In our calculations, we have combined the LEVEL 8.0 and BCONT programs [11, 18] to calculate the lifetimes for $\mathrm{Li_2}$ electronic states for energy levels within the internuclear distance up to the dissociation level. This is simply done by summing up the Einstein coefficients for bound-bound regions calculated by LEVEL 8.0 with the Einstein coefficients for the bound-free regions calculated by BCONT values and applying the formula 2.25.

$$\tau_i = 1/(\textstyle\sum_k A_{ik}) \tag{2.25}$$

Here A_{ik} terms stand for the Einstein coefficients and *i* stands for the initial level *i*, which undergoes radiative decay to lower energy lying energy levels *k* in multiple other electronic states and their continua.

2.8 Accumulation Curves of Rovibrational Wavefunction Overlap Integral

The sodium dimer experiment which is explained in detail in Chapter 3 has been repeated multiple times. However, we have found throughout the experiment that the normalized line intensities obtained via resolved fluorescence did not exactly match the theoretical line intensities. To understand the ultimate reason behind these inconsistencies between the normalized experimental and theoretical line intensities, we have created "accumulation curves" which are rovibrational wavefunction overlap integrals building up as a function of nuclear distance. Depending on where the overlap integrals accumulate, we can determine the R-centroid position corresponding to a specific transition. These curves provide us information as to where the transition probabilities are strongest and at what internuclear distance ranges the transitions occur.

Figure 2.7 shows that the line intensities for transitions from $6^1\Sigma_g^+(16,19)$ to the levels $A^1\Sigma_u^+(13,20)$ and $A^1\Sigma_u^+(16,20)$ states do not match the theoretical line intensities. Figure 2.8, Figure 2.9, Figure 2.10 and Figure 2.11 show the overlap integral accumulation curves for the $6^1\Sigma_g^+(16,19) \leftarrow A^1\Sigma_u^+(v',20)$ transitions. For the $6^1\Sigma_g^+(16,19) \leftarrow A^1\Sigma_u^+(16,20)$ transition, the accumulation occurs over the range 3-5Å and *R*-centroid approximation is not sufficient enough to determine the internuclear range accurately and a higher order approximation is required. For the $6^1\Sigma_g^+(16,19) \leftarrow$

$A^1\Sigma_u^+(11,20)$ transition, the overlap integral accumulates mostly at 3.5 Å and *R*-centroid approximation gives information about the internuclear distance range at which the transition occurs.

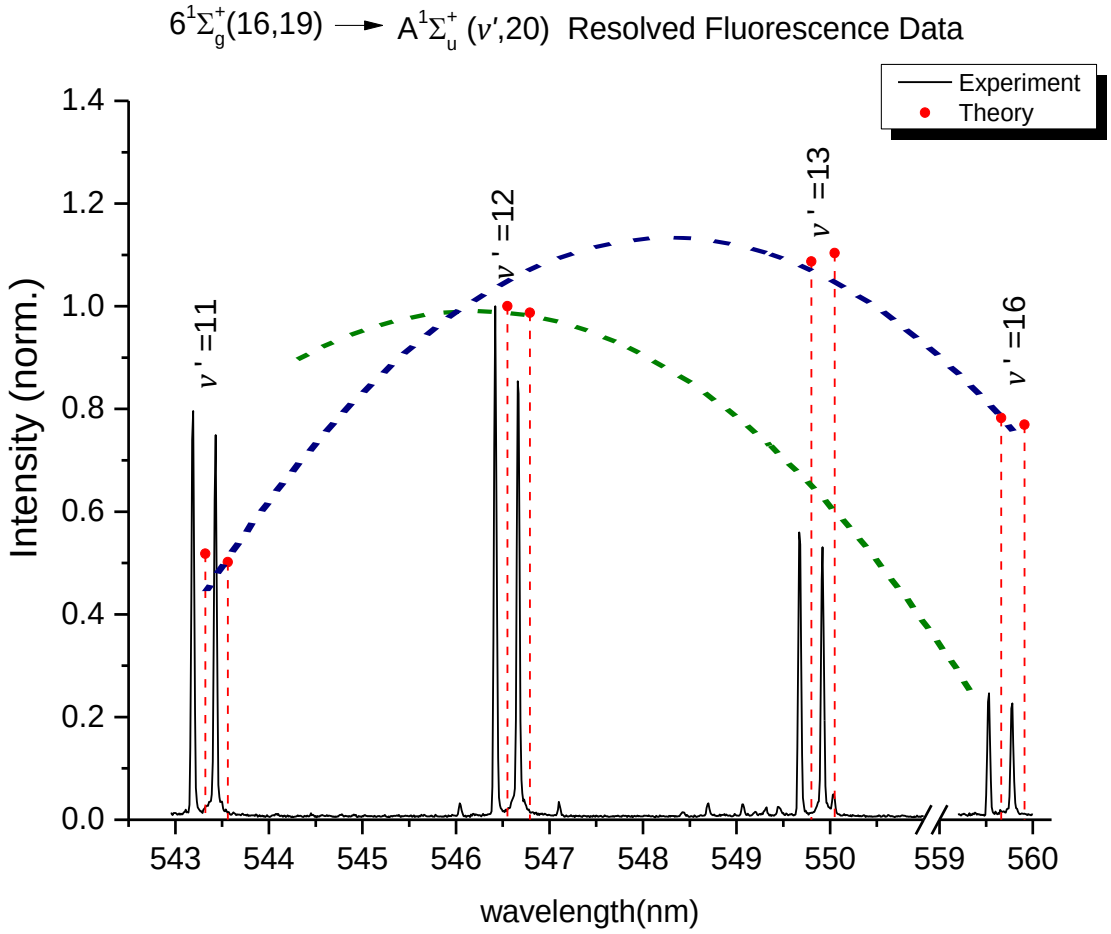

Figure 2.7 The comparison of experimental and theoretical line intensities for the Na_2 $6^1\Sigma_g^+(16,19) \rightarrow A^1\Sigma_u^+(v',20)$ transitions where v' is the vibrational number of the lower state. Blue and green dashed lines show the regions where the experiment differs from the theory most.

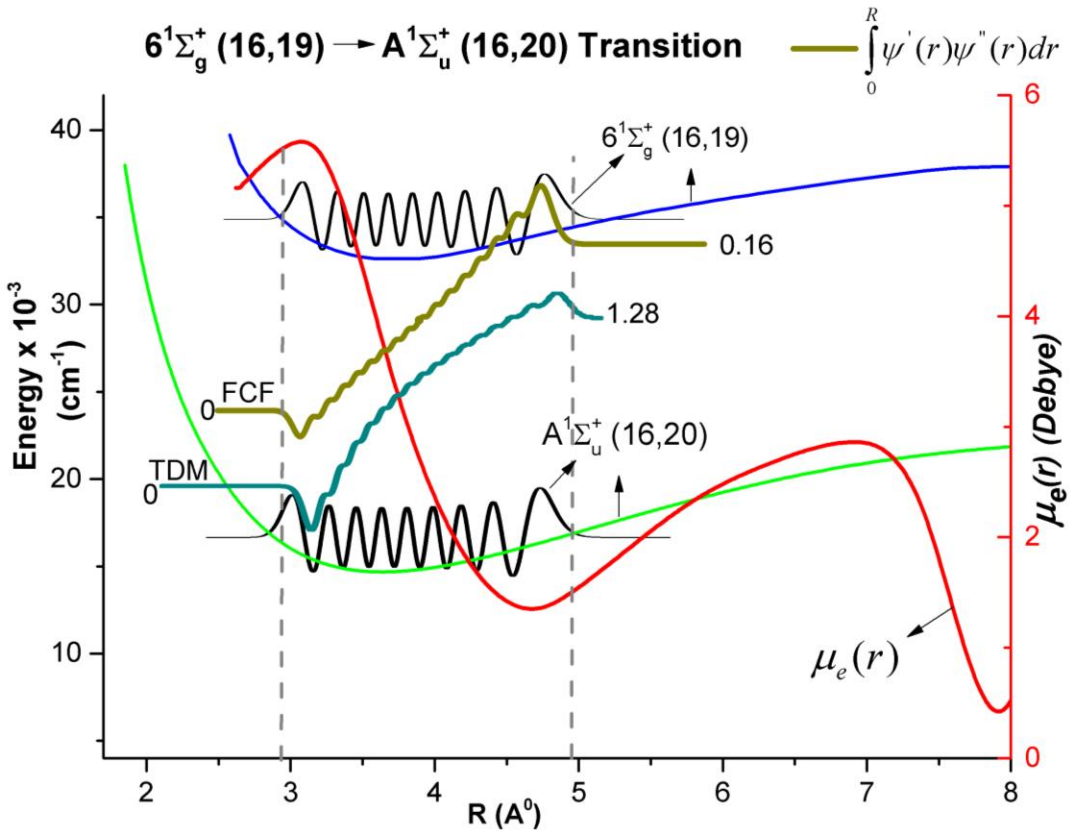

Figure 2.8 The accumulation curve for the Na_2 $6^1\Sigma_g^+(16,19) \rightarrow A^1\Sigma_u^+(16,20)$ transition. The integral accumulates linearly between 3 - 5Å. The dark green trace is for the Franck-Condon overlap integral and the dark cyan trace indicates the accumulation of the transition dipole moment matrix element.

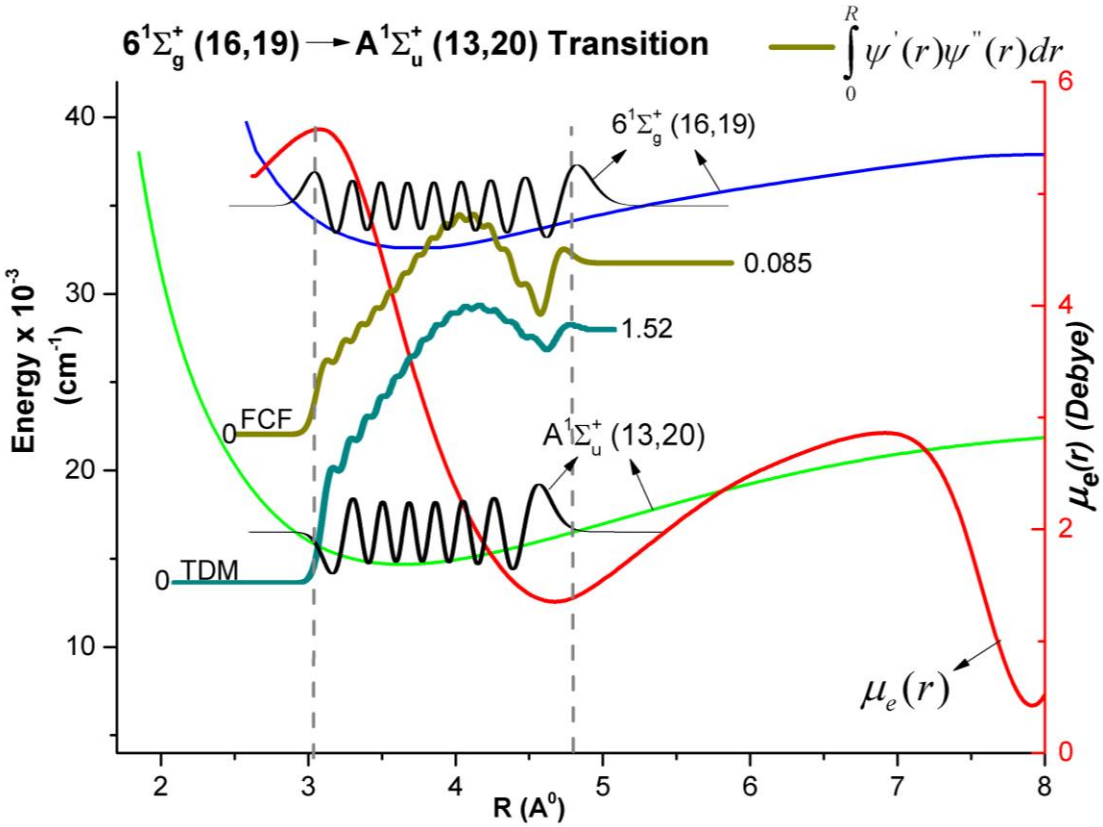

Figure 2.9 The accumulation curve for the Na_2 $6^1\Sigma_g^+(16,19) \rightarrow A^1\Sigma_u^+(13,20)$ transition. The accumulation is linear between 3-4Å. The accumulation predominantly occurs at 4Å. The dark green trace is for the Franck-Condon overlap integral and the dark cyan trace indicates the accumulation of the transition dipole moment matrix element.

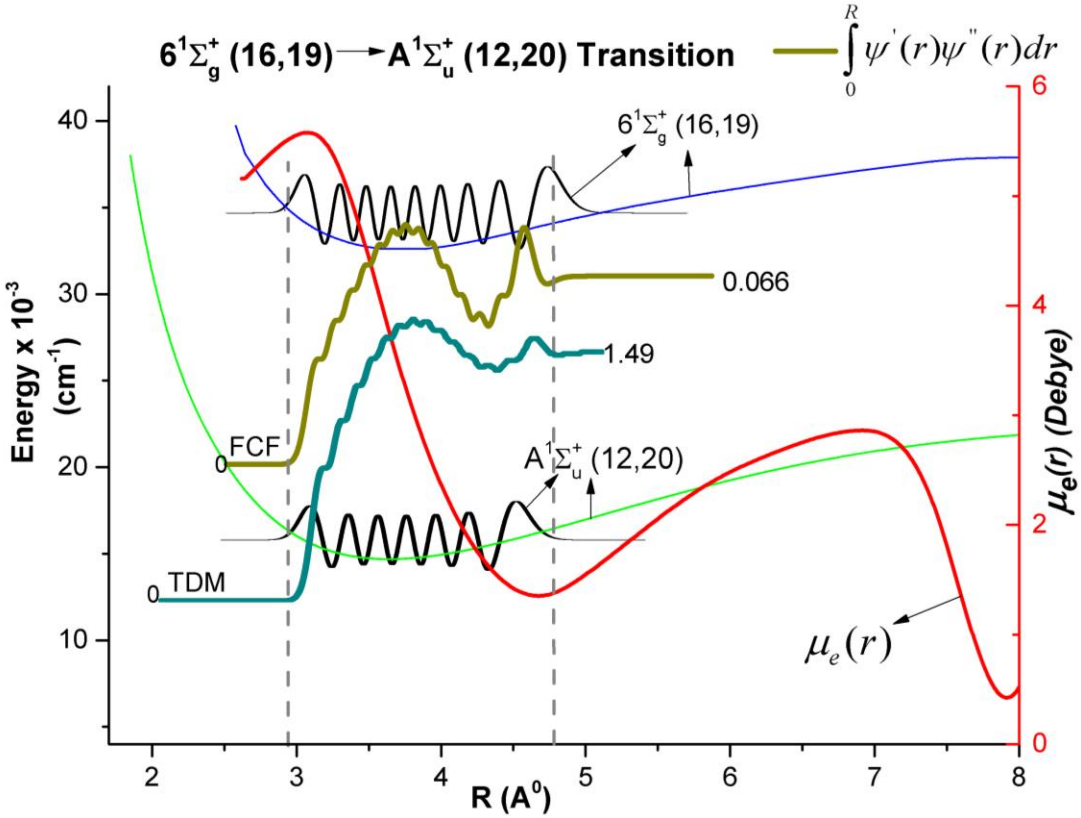

Figure 2.10 The accumulation curve for the Na_2 $6^1\Sigma_g^+(16,19) \rightarrow A^1\Sigma_u^+(12,20)$ transition. The integrals accumulate at 3.8Å. The dark green trace is for the Franck-Condon overlap integral and the dark cyan trace indicates the accumulation of the transition dipole moment matrix element.

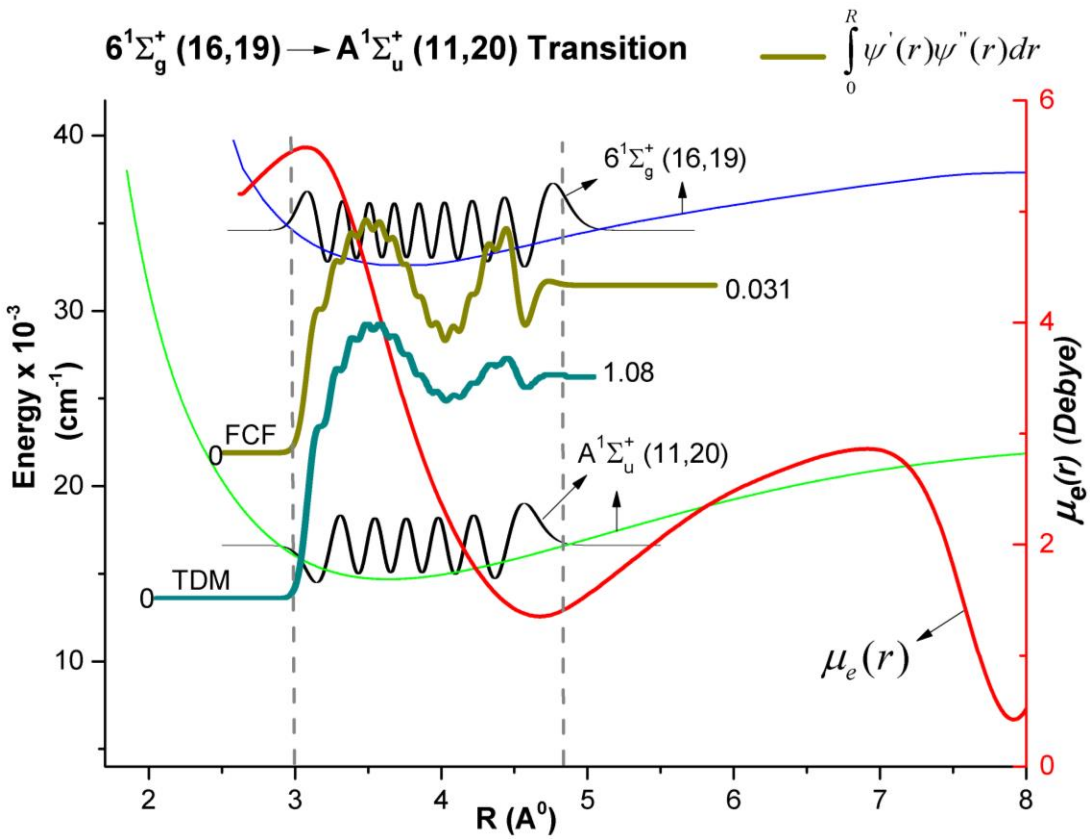

Figure 2.11 The accumulation curve for the Na_2 $6^1\Sigma_g^+(16,19) \rightarrow A^1\Sigma_u^+(11,20)$ transition. The overlap integral mostly accumulates around 3.5Å. The *R*-Centroid approximation accurately defines the internuclear range for the transition. The dark green trace is for the Franck-Condon overlap integral and the dark cyan trace indicates the accumulation of the transition dipole moment matrix element.

2.9 The *R*-Centroid Approximation

The R-Centroid approximation is a widely used method in order to define the *R*-dependence of electronic transition dipole moments of diatomic molecules. In the Autler-Townes method, by determining the peak-to-peak separation (Ω) in Eqn. 2.21, and the electric field of the coupling laser, one can extract the term μ, which is the electronic transition dipole moment matrix element. More explicitly:

$$\mu = < v' | \mu_e(R) | v'' > . \tag{2.26}$$

Here $|v' >$ and $|v'' >$ denote the higher and lower lying vibrational wavefuntions, respectively.

In other words, the *R*-Centroid approximation aims to extract the transition dipole moment function, $\mu_e(R)$ from Eqn. (2.26). The relative line intensities of the electronic transitions of a diatomic molecule depend on the product of the rotational line strength and the vibrational band strength. The rotational line strength can be calculated by diagonalizing the Hamiltonian to obtain the required rotational wavefunctions. The vibrational band strength is given by the equation [19] :

$$\begin{aligned} P_{(v',\, v'')} &= | \int_0^\infty \psi_{v'}(R) \mu_e(R) \psi_{v''}(R)\, dR |^2 \\ &= | < v' | \mu_e(R) | v'' > |^2 \end{aligned} \tag{2.27}$$

By assuming that $\mu_e(R)$ is constant and does not change with *R* over the region where the vibrational wavefunction overlap is significant, one can rewrite Eqn. 2.27 as

$$P_{(v',\,v'')} = [\mu_e(\bar{R})]^2 < v'|v'' > |^2,$$

with $$\bar{R} \equiv \frac{|<v'|R|\,v''>|}{|<v'|v''>|} \quad . \tag{2.28}$$

In the *R*-Centroid approximation, it is assumed that $\mu_e(R)$ is constant in the range where the overlap integral accumulates most of its value. The *R*-Centroid approximation is a first order approximation. The dipole moment function can be expanded in power series for higher order approximations as follows:

$$\mu_e(R) = \sum_{i=0}^{\infty} \mu_i \overline{R^i} \quad ; \; \mu_e(R) = \mu_0 + \mu_1 \overline{R} + \mu_2 \overline{R^2} \ldots \tag{2.29}$$

In this case, more terms are calculated in order to predict the dipole moment function as a function of internuclear distance *R*. The transition dipole moment matrix elements can be written as a power series as follows:

$$|< v'|\mu_e(R)|v'' >| = |< v'|v'' > | \sum_{i=0}^{\infty} \mu_i \overline{R^i}\,, \quad \overline{R^i} \equiv \frac{|<v'|R^i|\,v''>|}{|<v'|v''>|} \tag{2.30}$$

References

[1] V.K. Jain, Alpha Science International Limited, 2007.

[2] G. Herzberg, Spectra of Diatomic Molecules, Van Nostrand Reinhold Company 1966.

[3] L. L. Magnus, Ph.D. Thesis, Perturbation-Facilitated Optical-Optical Double Resonance Studies of NaK, Physics, Lehigh University, 2005.

[4] P.F. Bernath, Spectra of Atoms and Molecules, Oxford University Press, 2005.

[5] J.L. Dunham, The Energy Levels of a Rotating Vibrator, Physical Review 41 (1932) 721-731.

[6] I. Kovacs, Foundation of the theory of diatomic molecules, International Atomic Energy Agency (IAEA): IAEA.1974.

[7] E.E. Nikitin, R.N. Zare, Molecular Physics 82 (1994) 85-100.

[8] H.J. Wörner, F. Merkt, Fundamentals of Electronic Spectroscopy,Handbook of High-resolution Spectroscopy , John Wiley & Sons, 2011.

[9] R.J. Le Roy, RKR1: A computer program implementing the first-order RKR method for determining diatomic molecule potential energy functions, Journal of Quantitative Spectroscopy and Radiative Transfer 186 (2017) 158-166.

[10] O. Babaky, K. Hussein, Canadian Journal of Physics 67 (1989) 912-918.

[11] R.J. Leroy, University of Waterloo Chemical Physics Research CP-663, 2007.

[12] J.L. Picque, J. Pinard, Direct observation of the Autler-Townes effect in the optical range, Journal of Physics B: Atomic and Molecular Physics 9 (1976) L77.

[13] T. Kirova, Ph.D. thesis, Temple University, (2005).

[14] D.R. Skinner, R.E. Whitcher, Measurement of the radius of a high-power laser beam near the focus of a lens, Journal of Physics E: Scientific Instruments 5 (1972) 237.

[15] R.N. Zare, Angular Momentum : understanding spatial aspects in chemistry and physics Wiley, New York1988.

[16] S.J. Sweeney, E.H. Ahmed, P. Qi, T. Kirova, A.M. Lyyra, J. Huennekens, Journal of Chemical Physics 129 (2008).

[17] E.H. Ahmed, P. Qi, A.M. Lyyra, Physical Review A 79 (2009).

[18] Robert J. Le Roy, G.T. Kraemer, BCONT 2.2 A computer Program for Calculating Bound to Continuum Transition Intensities for Diatomic Molecules, University of Waterloo, 2002.

[19] C. Noda, R.N. Zare, Relation between classical and quantum formulations of the Franck-Condon principle: The generalized R-centroid approximation, Journal of Molecular Spectroscopy 95 (1982) 254-270.

CHAPTER 3

MEASUREMENT OF THE ELECTRONIC TRANSITION DIPOLE MOMENT MATRIX ELEMENTS OF THE $5^1\Sigma_g^+ \rightarrow A^1\Sigma_u^+$ AND $6^1\Sigma_g^+ \rightarrow A^1\Sigma_u^+$ TRANSITIONS OF THE SODIUM DIMER VIA OPTICAL-OPTICAL DOUBLE RESONANCE AND AUTLER-TOWNES SPECTROSCOPY

3.1 Introduction

We present here an experimental study of the electronic transition dipole moment matrix elements (TDMM) for the $5^1\Sigma_g^+ \rightarrow A^1\Sigma_u^+$ and $6^1\Sigma_g^+ \rightarrow A^1\Sigma_u^+$ electronic transitions of Na_2. Lifetime calculations based on these Na_2 TDMM's for the $3^1\Sigma_g^+$, $4^1\Sigma_g^+$, $5^1\Sigma_g^+$, and $6^1\Sigma_g^+$ electronic states were published earlier [1]. An accurate knowledge of the transition dipole moment matrix elements is crucial because critical parameters for diatomic molecules such as emission and absorption line intensities, lifetimes and Einstein coefficients depend on these matrix elements. The Na_2 $5^1\Sigma_g^+$ and $6^1\Sigma_g^+$ electronic states of the sodium dimer, which interact significantly with the ion-pair

(Na^+ + Na^-) Coulomb interaction potential, exhibit double wells and shoulders due to avoided crossings of the adiabatic potential energy functions [2-4]. The amplitude of the rovibrational wavefunctions for the electronic states increase around the shoulders and the outer wells of the potential energy functions. This causes the coupling of the lower and upper state wavefunctions to change abruptly, which in turn causes the electronic transition dipole moments of the $5^1\Sigma_g^+ \rightarrow A^1\Sigma_u^+$ and $6^1\Sigma_g^+ \rightarrow A^1\Sigma_u^+$ electronic transitions to exhibit rapidly changing behavior as a function of *R* [1].

Traditionally, electronic transition dipole moments have been determined by *ab initio* calculations or experimentally by using spectral line intensities. However, only relative transition dipole moments can be determined based on line intensities. Lifetime measurements involve decay to several lower lying electronic states and thus include the effect of multiple transition dipole moments. Intensity measurements are not absolute, because it is very difficult to calibrate the wavelength and the polarization dependence of the detection system and to determine the molecular densities with high accuracy [5]. On the other hand, by using the absolute transition dipole moment matrix elements from the Autler-Townes splitting measurements, these relative transition dipole moments can be converted to an absolute scale. The Autler-Townes method for a three-level system involves a weak probe laser pumping the population from the ground state to an intermediate state and a strong coupling laser transferring the population from the intermediate state to the higher state. The weak probe laser is scanned while the strong coupling laser is kept on resonance and the Autler-Townes splitting is obtained. The Autler-Townes method is superior to other experimental methods in obtaining the electronic transition dipole moment as a function of internuclear distance *R*, because it

only requires an accurate measurement of the coupling laser electric field amplitude and the determination of the Rabi frequency from the Autller-Townes splitting spectra [5]. Optical-optical double resonance (OODR) experiments [6-12] provide a quantum state selective method to probe transition dipole moments of thermal samples of diatomic molecules both in terms of relative fluorescence intensity measurements as well as by using coherence effects such as the Autler-Townes (AT) effect for the measurement of the absolute magnitude of the transition dipole matrix element [5, 13-17]. For the cascade excitation scheme in Doppler-broadened systems, the lasers must be counter-propagating for the AT splitting to be resolved [18, 19]. Here the pump transition is $X^1\Sigma_g^+ \,|1> \rightarrow A^1\Sigma_u^+ \,|2>$ and the coupling laser transitions are $A^1\Sigma_u^+ \,|2> \rightarrow 5^1\Sigma_g^+ \,|3>$ and $A^1\Sigma_u^+ \,|2> \rightarrow 6^1\Sigma_g^+ \,|3>$ of the Na_2 molecule. In order to test the *ab initio* transition dipole moment functions, we have carried out OODR and Autler -Townes experiments. The absolute values of the transition dipole moment matrix elements (TDMM) for specific transitions need to be obtained from the AT splitting experiments [20]. The relative spectral line intensities, for many transitions, obtained through resolved fluorescence are given by $I_{fluor} \propto \nu_{ik}^4 |\mu_{ik}|^2$ where ν_{ik} is the transition frequency and μ_{ik} is the transition dipole matrix element with indexes *i* and *k* denoting the upper and lower levels of the transition. This relationship can be used to obtain more absolute transition dipole moment matrix elements by combining the AT splitting data with the data obtained through resolved fluorescence. The ratio of line intensities in the expression $\frac{I_{ij}}{I_{ik}} = \frac{\nu_{ij}^4 |\mu_{ij}|^2}{\nu_{ik}^4 |\mu_{ik}|^2}$ is equal to the ratio of dipole moment matrix elements squared. Using one of the absolute transition dipole moment matrix element measurements obtained through

AT splitting method (for which we also obtained the line intensity from resolved fluorescence spectra following OODR excitation) more absolute dipole moment matrix elements can be obtained for transitions recorded by resolved fluorescence.

Combining the Autler-Townes splitting method with resolved fluorescence experiment is beneficial in certain aspects. Both methods have their own limitations and advantages. The Autler-Townes method works only for strong coupling laser transitions |2>→|3> for the three-level cascade system here, for which the transition dipole moment matrix elements are strong in accordance with the Franck-Condon principle [21]. The resolved fluorescence, on the other hand, is useful also for recording relatively weak transitions (with $\mathrm{TDMM} \leq 1.0$ Debye) making it possible to obtain data corresponding to a greater range of v and J (and hence, through R-centroid approximation, a greater internuclear distance). Since the line intensities obtained from resolved fluorescence are only relative, by combining these two methods, absolute values of transition dipole matrix elements are made available for a larger range of internuclear distances compared to that provided by the Autler-Townes measurements. In addition, the Autler-Townes effect based measurements can be used to test theoretically calculated *ab initio* electronic transition dipole moments, which are also absolute. The experimental setup for the AT splitting measurements is the same as for an OODR experiment with a couple of differences. The pump laser (L_1), and the probe laser (L_2) in the OODR experiment are now called the probe and coupling lasers, respectively. In addition, to observe the AT splitting effect, the coupling laser transition must have a strong transition dipole moment matrix element since the AT splitting will be smaller if the |2>→ |3> transition is weak. A strong coupling laser transition leads to the observation of a more easily resolved AT

splitting in the spectrum. In addition, the probe and coupling laser beams should be perfectly collinearly aligned and counterpropagating [20].

3.2 Experimental Details

3.2.1 Experimental Overview

The experimental setup for Autler-Townes and OODR experiments is as shown in Figure 3.1. The Sodium vapor was generated in a five-arm heat pipe oven. Argon gas was used as the buffer gas with a pressure of about 300-400mTorr. The temperature of the heat pipe oven was in the range of 600K to 800K. In both experiments, single, longitudinal mode, frequency stabilized, tunable, continuous-wave (CW) Coherent, Inc. Autoscan 699-29 ring dye lasers pumped by Verdi V10 (Coherent, Inc.) were used. The probe laser (L_1) was operated with a DCM dye, while the coupling laser (L_2) with a R6G 590 dye. For the Autler-Townes experiments the first laser is called the probe laser and the second the coupling laser. For OODR experiments, on the other hand, the first laser is called the pump laser and the second is called the probe laser. A lock-in amplifier (Stanford Research SR850) was used for phase sensitive detection of the photomultiplier signal with a mechanical chopper (SR540) to modulate the pump laser beam. A photomultiplier (PMT) (Hamamatsu R928), mounted on the top window of the heat pipe, was used to monitor the signal during the OODR scans. The photomultiplier tube voltage at the SPEX double monochromator was set to 984V. Fluorescence emitted along the horizontal arm of the heatpipe perpendicular to the laser propagation was collected and sent to a SPEX 1404 double monochromator. The resolved fluorescence spectrum was obtained by scanning the SPEX 1404 spectrometer while the probe and the coupling

lasers were kept on resonance. The line intensities in the recorded spectra where calibrated for wavelength variation of the spectrometer response using a white light incandescent source [22]. In the AT effect based measurements, the coupling laser (L_2) was kept on resonance while the probe laser (L_1) was scanned. To ensure that the lasers remained on resonance while the resolved fluorescence was recorded the total fluorescence from the excited $5^1\Sigma_g^+(v, J)$ and $6^1\Sigma_g^+(v, J)$ states was monitored with a bandpass filtered PMT attached to one of the side arms of the heatpipe oven. In order to minimize the residual Doppler linewidth the two lasers were counter-propagated. To ensure that the coupling laser E field amplitude was homogenous in the volume probed in the AT splitting measurements the spot size of the coupling laser was chosen to be approximately twice as large as the spot size for the probe laser. The spot sizes for L_1 and L_2 for the $5^1\Sigma_g^+$ state were 150μm and 263μm, while for the $6^1\Sigma_g^+(v, J)$ state they were 158μm and 278μm, respectively. The electric field amplitudes were calculated from the measured spotsize (w) defined at the $1/e^2$ points of the Gaussian beam profile and laser power P using the expression $E = \sqrt{\frac{4\mathrm{P}}{\pi c \varepsilon_0 w^2}}$. The spot sizes were determined experimentally using the razor blade technique (see sec. 3.2.3). The loss at the entrance window of the heatpipe for each laser was estimated to be approximately 10%, obtained from the measured total laser transmission of the cold heatpipe.

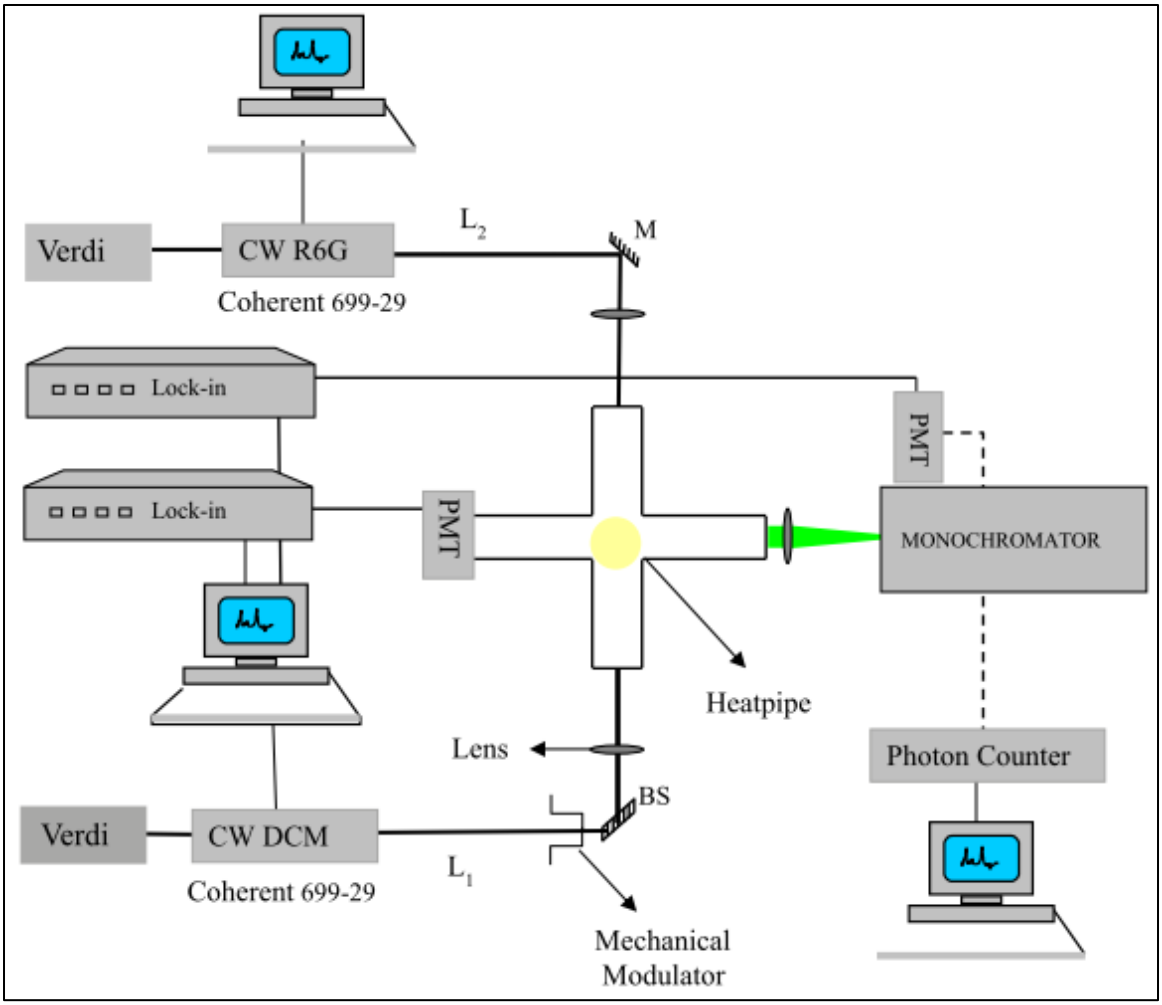

Figure 3.1 Experimental schematic of Autler-Townes spectroscopy and resolved fluorescence experiments. L_1 and L_2 are the tunable pump/probe and the coupling lasers, respectively. The tunable ring dye lasers are pumped by Verdi V10 lasers. The total fluorescence collection PMT was mounted on the top arm of the heatpipe. A BOMEM FT-IR spectrometer was used to calibrate the probe and coupling lasers. For the AT splitting experiment, a PMT was used, and for the resolved fluorescence experiment a photon counter was used.

3.2.2 Doppler Profile

The AT splitting program requires various parameters as input. The temperature inside the heat pipe at the moment of the experiment is one of these parameters. It is determined from the Doppler broadening of a particular pump laser transition. When the coupling laser is off, the pump laser is scanned to obtain the Doppler broadening as in the Figure 3.2.

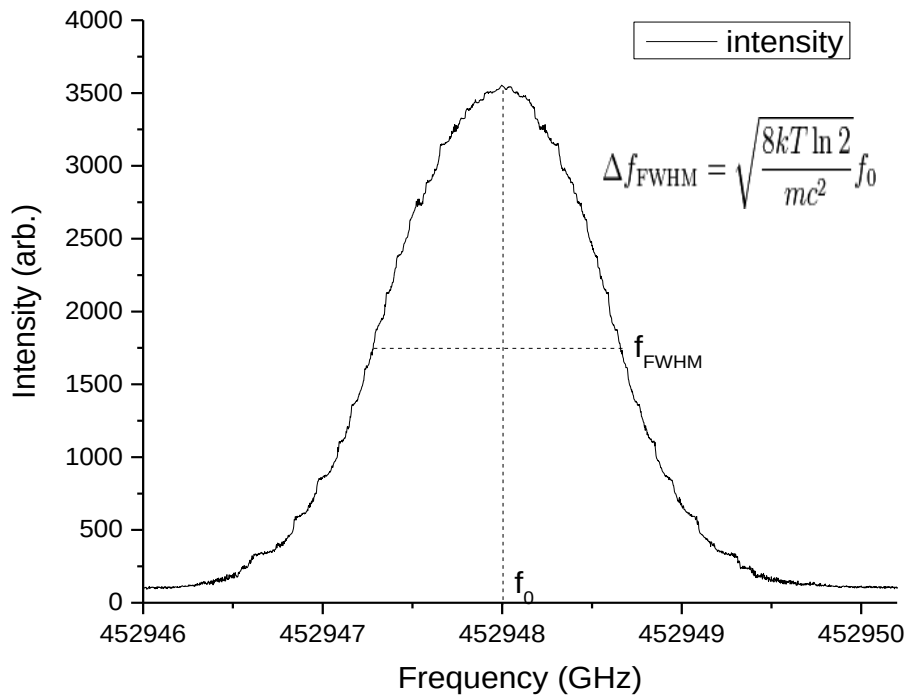

Figure 3.2 Doppler profile for the $A^1\Sigma_u^+(4.20) \leftarrow X^1\Sigma_g^+(0,19)$ transition of Na_2 molecule, detected by scanning the pump laser while observing the $A^1\Sigma_u^+(4.20) \leftarrow X^1\Sigma_g^+(0,19)$ fluorescence.

The temperature is found by using the Doppler broadening formula (Eqn. 3.1). The temperature depends on the center frequency at maximum intensity of the Doppler profile, the full width at half maximum frequencies, the Boltzmann constant, and the speed of light.

$$\Delta f_{FWHM} = f_0 \sqrt{\frac{8kTln2}{mc^2}} \,. \tag{3.1}$$

3.2.3 Laser Beam Profiling Using the Razor Blade Technique

The spot size (w) of a laser beam is a major factor in AT spectroscopy experiments. In order to obtain quantitative information from the Autler-Townes splitting measurement, the spot size of the pump laser must be significantly smaller than that of the coupling laser. In addition, the spot size values are used in the Autler-Townes simulation program to obtain the simulated curve for the Autler-Townes spectra. Parameters in this simulation are adjusted to fit the experimental curve in order to extract the experimental Rabi frequencies (Ω).

The electric field amplitude of a laser often exhibits a radial Gaussian distribution. The electric field amplitude and the power of a laser beam are related as follows:

$$E(r) = E_0 \exp\left(-\frac{r^2}{w^2}\right)$$

$$P_{Tot} = \int_0^{+\infty} \int_0^{2\pi} I(r) r dr d\varphi \tag{3.2}$$

Here the intensity is $I(r) = \epsilon c E^2(r)/2$. The result of the integration of the total power yields:

$$E_0 = \sqrt{\frac{4P_{Tot}}{c\epsilon_0 \pi w^2}}\,. \tag{3.3}$$

In the razor blade technique, the laser beam is assumed to have a Gaussian waveform and the laser beam is gradually cut by a sharp blade while the position of the blade and the laser power after the blade are recorded. The spot size of the Gaussian beam is defined as the radius measured at $1/e^2$ of the intensity of the beam profile [23]. There are two common ways of calculating the beam waist w after recording the data. The first method is simply recording the intensity versus distance data and fitting the data to a Gaussian curve. In this case the horizontal width between $1/e^2$ locations of two sides of the Gaussian profile is $2w$. The beam waist is half of this value. The second method of obtaining the beam waist is simply to record the positions of the blade at 75% (d_{75})and 25% (d_{25}) transmission of the total laser beam power and using the formula

$$w = \frac{1}{2\sqrt{C}}\,(d_{75} - d_{25}). \tag{3.4}$$

Here C is defined as the solution of the error function $\mathrm{erf}(c) = 1/2$, and has the value C= 0.47 [24]. In our experiments we used this method to obtain the spot size of the laser beams. Eqn. (3.4) has been derived from the Gaussian profile in Ref.[24].

3.3 Results and Discussion

Using the AT splitting and resolved fluorescence methods the transition dipole moment matrix elements for a number of rovibratinal transitions between the $A^1\Sigma_u^+$ and the $5^1\Sigma_g^+$ and $6^1\Sigma_g^+$ ion-pair states were measured. Line intensities are proportional to the matrix elements through the relation $I_{fluor} \propto \nu^4|\mu|^2$. From the ratio of line intensities, using one measured transition dipole moment matrix element (TDM) from the AT method as the reference, one can find the absolute TDM for the remaining transition. This method allowed us to obtain more absolute transition dipole moment matrix elements in addition to those obtained directly from the AT method. Experimental and calculated transition dipole moments, using the first order *R*-Centroid approximation and the second-order approximation [25] for both experiments are listed in Table 3.1 and Table 3.2. It was possible to obtain more data for the $5^1\Sigma_g^+(v, J) \rightarrow A^1\Sigma_u^+(v', J')$ transition compared to the $6^1\Sigma_g^+(v, J) \rightarrow A^1\Sigma_u^+(v', J')$ electronic transition corresponding to an internuclear distance range of 2.73-5.27Å. By combining the Autler-Townes splitting data with the resolved fluorescence data, we were able to expand this range to 2.33-5.42Å. Figure 3.3 (a) shows the Autler-Townes excitation scheme for the $5^1\Sigma_g^+(23,21) \rightarrow A^1\Sigma_u^+(21,20)$ electronic transition. Figure 3.4 shows the Autler-Townes splitting spectrum for the $5^1\Sigma_g^+(23,21) \rightarrow A^1\Sigma_g^+(21,20)$ transition. We have obtained the resolved fluorescence data for the $5^1\Sigma_g^+(23,21) \rightarrow A^1\Sigma_u^+(21,22)$ Autler-Townes splitting transition, corresponding to the P line of this transition. This transition was then used to calibrate the dipole moments obtained from resolved fluorescence to an absolute scale. In the end, we have used the R-

Centroid and second order multivariable fit to plot transition dipole moments as a function of R as shown in Figure 3.7.

For the $6^1\Sigma_g^+(v, J) \rightarrow A^1\Sigma_u^+(v', J')$ transitions the simulated and the experimental electronic transition dipole moments differ from 1 to 13%. All of the transitions from the AT splitting experiments correspond to an internuclear distance range of 3.16Å to 4.22Å (Table 3.2). Since among the $6^1\Sigma_g^+(v, J) \rightarrow A^1\Sigma_u^+(v', J')$ rovibronic transitions there were only a few strong transitions involving mainly low lying rovibrational levels in the $6^1\Sigma_g^+$ state, the data obtained through the Autler-Townes method was limited. The resolved fluorescence experiment for the $6^1\Sigma_g^+(v, J) \rightarrow A^1\Sigma_u^+(v', J')$ excitation used the same experimental setup except that both lasers (L_1 and L_2 in Figure 3.3 (b)) were kept on resonance while the SPEX 1404 monochromator was scanned. As a result, the experimental data spanned the internuclear distance range of 2.87-4.54Å. Figure 3.5 shows the Autler-Townes simulation for the $6^1\Sigma_g^+(15,19) \rightarrow A^1\Sigma_u^+(15,20)$ electronic transition. The spectra from resolved fluorescence are shown in Figure 3.6. Having obtained the absolute transition dipole moments, we have applied the R-centroid approximation [25] as well as a second order multivariable fit and obtained the transition dipole moment as a function of internuclear distance as shown in Figure 3.8. Both the first order R-centroid approximation and the second order multivariable fit show good agreement with the theoretically calculated *ab initio* data (Figure 3.8).

The R-Centroid values of the transition dipole moments for the $5^1\Sigma_g^+(v, J) \rightarrow A^1\Sigma_u^+(v', J')$ transition are scattered around 3.5Å and 5Å in Figure 3.7. The transition dipole moment matrix elements obtained around 5Å are as small as 1.0 Debye. The AT splitting is quite small for transitions with transition dipole moment matrix elements

smaller than 2.0 Debye. This could be a limitation to the precision of the observations in this region due to the fact that it is difficult to observe and optimize the splittings that are too small. The larger splittings with TDM values greater than 2.0 Debye, on the other hand, are easier to obtain and optimize. Once the splitting is obtained, laser powers, alignment of the counterpropagating beams and spot sizes were optimized to maximize the AT splitting. The TDM values for $5^1\Sigma_g^+(v, J) \rightarrow A^1\Sigma_u^+(v', J')$ around 3.5Å and 5Å are also the regions where the transition dipole moment function D(R) has physical sharp turning points (Figure 3.3 (a)). This indicates that the value of the overlap integrals of the wave functions changes drastically around these regions due to the change of the shape of the potential energy curves. Around 5Å the potential energy curve of $5^1\Sigma_g^+$ state starts broadening to the right becoming less steep. This causes the wavefunction of the $5^1\Sigma_g^+$ state to expands over this region. This has an effect on the overlap integral values and the transition dipole moment matrix elements. The calibrated wavenumbers for the AT splitting experiments and the laser power values for the probe and the coupling lasers for all transitions are given in the supplementary data.

With double resonance excitation schemes, the inner well behavior of the electronic transition dipole moment functions for the $5^1\Sigma_g^+ \rightarrow A^1\Sigma_u^+$ and $6^1\Sigma_g^+ \rightarrow A^1\Sigma_u^+$ transitions could be observed. However, their behavior at a larger internuclear distance is not available. This is the case because the Franck-Condon Factors (FCFs) and transition dipole moment matrix elements are only strong for the double resonance excitation for a few of the $5^1\Sigma_g^+ \rightarrow A^1\Sigma_u^+$ and $6^1\Sigma_g^+ \rightarrow A^1\Sigma_u^+$ transitions. Therefore, these double resonance experiments are limited to the inner well behavior of the transition dipole moment functions. Nevertheless, the theoretically calculated *ab initio* transition dipole moments

cover the full internuclear distance range. Triple resonance and quadruple resonance experiments could be used for additional experimental mapping of the transition dipole moment internuclear distance dependence if Franck-Condon factors are favorable for these excitation schemes.

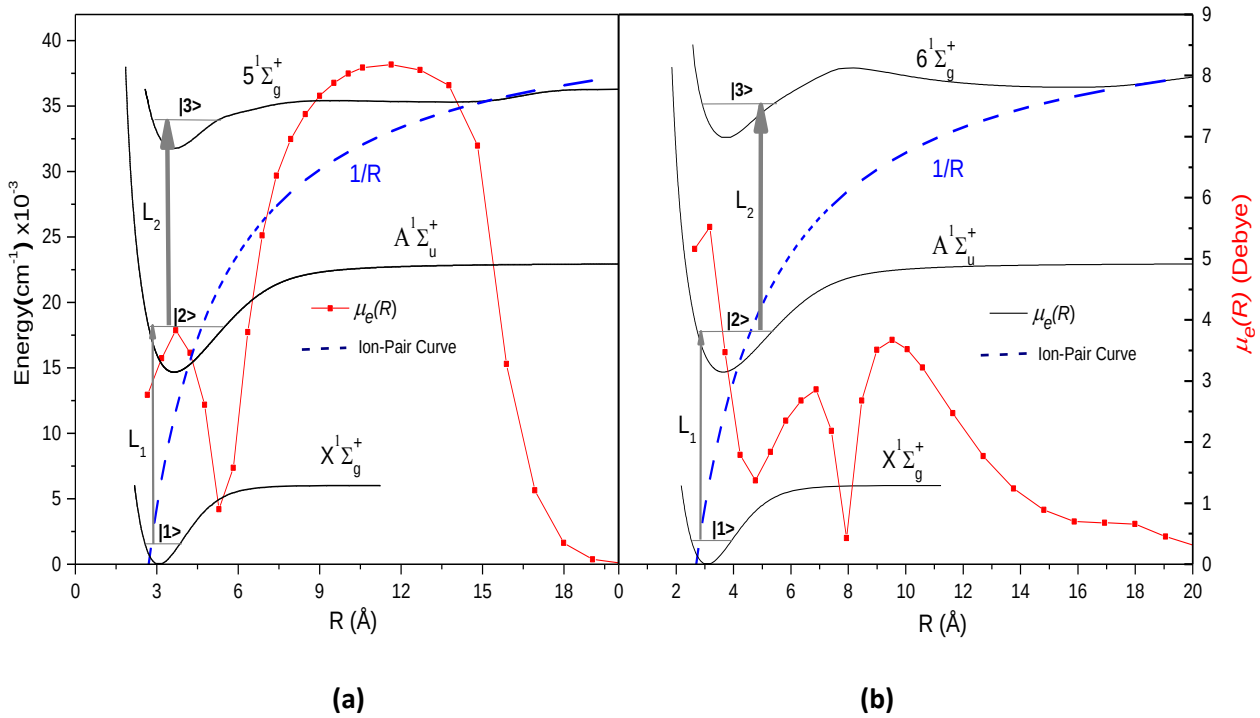

Figure 3.3 The Na_2 excitation scheme for the $5^1\Sigma_g^+ \leftarrow A^1\Sigma_u^+ \leftarrow X^1\Sigma_g^+$ (a), and the $6^1\Sigma_g^+ \leftarrow A^1\Sigma_u^+ \leftarrow X^1\Sigma_g^+$ (b) transitions. L_1 and L_2 are counter-propagating probe and coupling lasers respectively. The *ab initio* transition dipole moment function[1] is highlighted in red. The blue dashed line is the Na^++Na^- ion-pair curve.

Table 3.1 Transition dipole moment matrix elements obtained from the Autler-Townes splitting method and from the resolved fluorescence line intensities for the Na_2 $\mathbf{5}^1\Sigma_g^+(\boldsymbol{v}, J) \rightarrow A^1\Sigma_u^+(\boldsymbol{v}', J')$ transitions.

$5\Sigma_g^+(\boldsymbol{v}, J)$	$A^1\Sigma_u^+(\boldsymbol{v}', J')$	TDMM (Debye) Experiment	TDMM (Debye) Theory	$<\boldsymbol{v}, J \mid \boldsymbol{v}', J'>$	$\overline{R}$, Å	$\overline{R^2}$, Å^2	
(4,21)	(4,20)	3.124	3.605	0.992	3.74	14.08	Autler-Townes
(8,21)	(8,20)	3.238	3.327	0.952	3.81	14.78	
(10,21)	(10,20)	2.902	3.089	0.903	3.84	15.08	
(10,20)	(9,21)	0.767	1.005	0.264	2.73	6.41	
(11,20)	(10,21)	0.988	1.195	0.316	2.93	7.90	
(12,21)	(11,22)	1.238	1.395	0.372	3.09	9.18	
(13,21)	(13,20)	2.278	2.529	0.768	3.86	15.3	
(13,21)	(12,20)	1.389	1.646	0.444	3.26	10.45	
(13,19)	(14,18)	0.839	1.062	0.347	5.27	26.09	
(15,21)	(14,20)	1.931	2.034	0.616	3.81	15.07	
(15,21)	(16,22)	0.987	1.110	0.380	5.22	25.79	
(17,21)	(16,20)	2.208	2.327	0.661	3.65	13.56	
(17,21)	(18,20)	0.894	1.051	0.374	5.15	25.34	
(20,21)	(19,20)	2.068	2.178	0.662	3.8	14.87	
(23,21)	(21,20)	1.913	2.034	0.593	3.7	14.00	
(27,21)	(24,20)	1.504	1.710	0.525	3.76	14.64	
(23,21)	(20,20)	0.561	0.667	0.180	2.46	4.55	
(23,21)	(20,22)	0.512	0.608	0.164	2.33	3.51	Resolved Fluorescence
(23,21)	(21,22)	1.913	2.029	0.590	3.69	13.96	
(23,21)	(22,20)	1.086	0.844	0.294	3.42	12.36	
(23,21)	(22,22)	1.160	0.909	0.314	3.47	12.68	
(23,21)	(23,20)	0.792	0.729	0.266	5.37	26.92	
(23,21)	(23,22)	0.695	0.710	0.261	5.42	27.34	
(17,21)	(17,20)	1.152	1.204	0.401	3.65	13.65	
(17,21)	(17,22)	1.124	1.272	0.422	3.63	13.83	
(17,21)	(18,20)	0.894	1.051	0.374	5.15	25.34	
(17,21)	(18,22)	0.842	1.035	0.371	5.19	25.61	
(17,21)	(19,20)	0.746	0.874	0.403	4.70	22.55	

Table 3.2 Transition dipole moment matrix elements obtained from the Autler-Townes splitting method and from the resolved fluorescence line intensities for the Na_2 $\mathbf{6}^1\Sigma_g^+(\boldsymbol{v}, J) \rightarrow A^1\Sigma_u^+(\boldsymbol{v}', J')$ transitions.

$6^1\Sigma_g^+(\boldsymbol{v}, J)$	$A^1\Sigma_u^+(\boldsymbol{v}', J')$	TDMM (Debye) Experiment	TDMM (Debye) Theory	$< \boldsymbol{v}, J \| \boldsymbol{v}', J' >$	$\overline{R}$, Å	$\overline{R^2}$, Å^2	
(4,19)	(3,20)	2.284	2.205	0.482	3.42	11.66	Autler-Townes
(5,19)	(4,20)	2.158	2.128	0.469	3.43	11.69	
(7,19)	(4,20)	1.000	1.156	0.201	3.16	9.92	
(10,19)	(11,20)	1.596	1.545	0.661	4.14	17.29	
(13,19)	(14,20)	1.328	1.311	0.531	4.22	18.05	
(15,19)	(15,20)	1.136	1.201	0.359	3.69	13.43	
(19,19)	(19,20)	1.159	1.250	0.444	3.98	15.98	
(22,19)	(21,20)	1.095	1.158	0.323	3.62	12.99	
(15,19)	(9,18)	0.518	0.516	0.086	2.88	8.20	Resolved Fluorescence
(15,19)	(9,20)	0.474	0.502	0.084	2.87	8.17	
(15,19)	(10,18)	0.917	0.946	0.161	2.99	8.87	
(15,19)	(10,20)	0.869	0.929	0.158	2.98	8.84	
(15,19)	(11,18)	1.375	1.406	0.249	3.10	9.57	
(15,19)	(11,20)	1.314	1.393	0.246	3.10	9.55	
(15,19)	(12,18)	1.642	1.592	0.301	3.19	10.16	
(15,19)	(12,20)	1.608	1.598	0.301	3.19	10.13	
(15,19)	(13,18)	1.359	1.126	0.258	3.36	11.28	
(15,19)	(13,20)	1.357	1.159	0.263	3.35	11.22	
(15,19)	(15,18)	1.122	1.220	0.366	3.70	13.53	
(15,19)	(16,18)	1.215	0.962	0.369	4.29	18.80	
(15,19)	(16,20)	1.192	1.000	0.386	4.28	18.75	
(15,19)	(17,18)	0.821	0.955	0.617	4.53	20.52	
(15,19)	(17,20)	0.762	0.936	0.614	4.54	20.60	

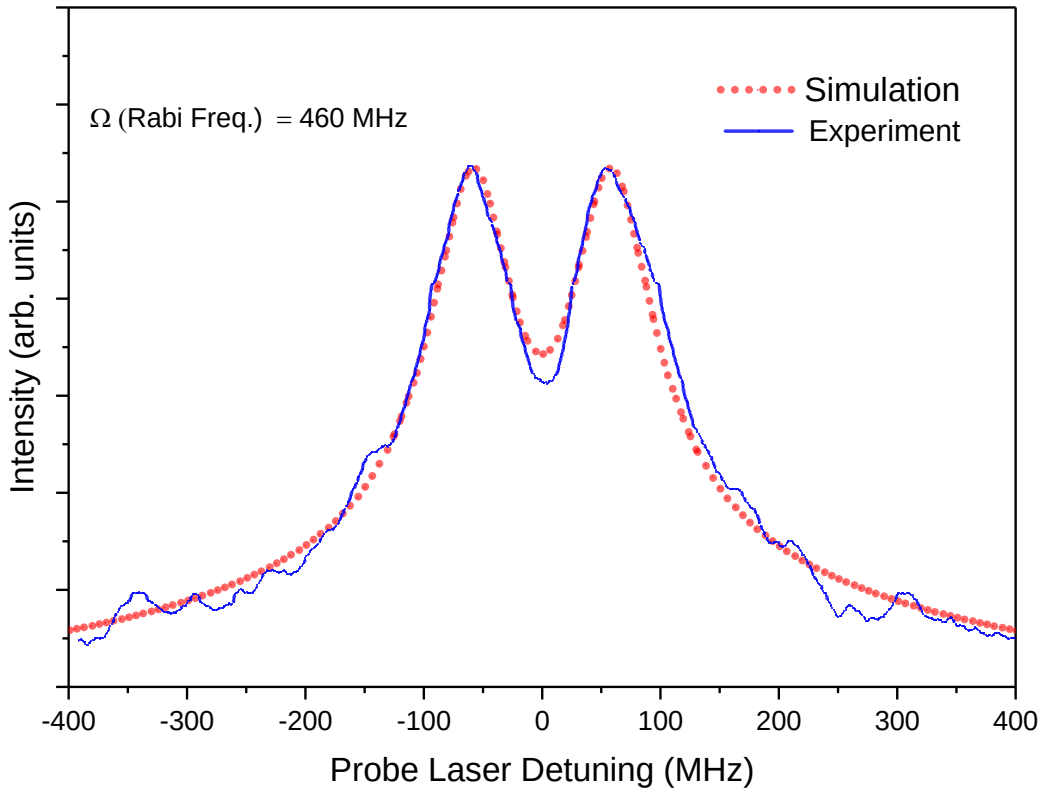

Figure 3.4 Autler-Townes splitting spectra for Na_2 $5^1\Sigma_g^+(23,21) \rightarrow A^1\Sigma_u^+(21,20)$ transition.

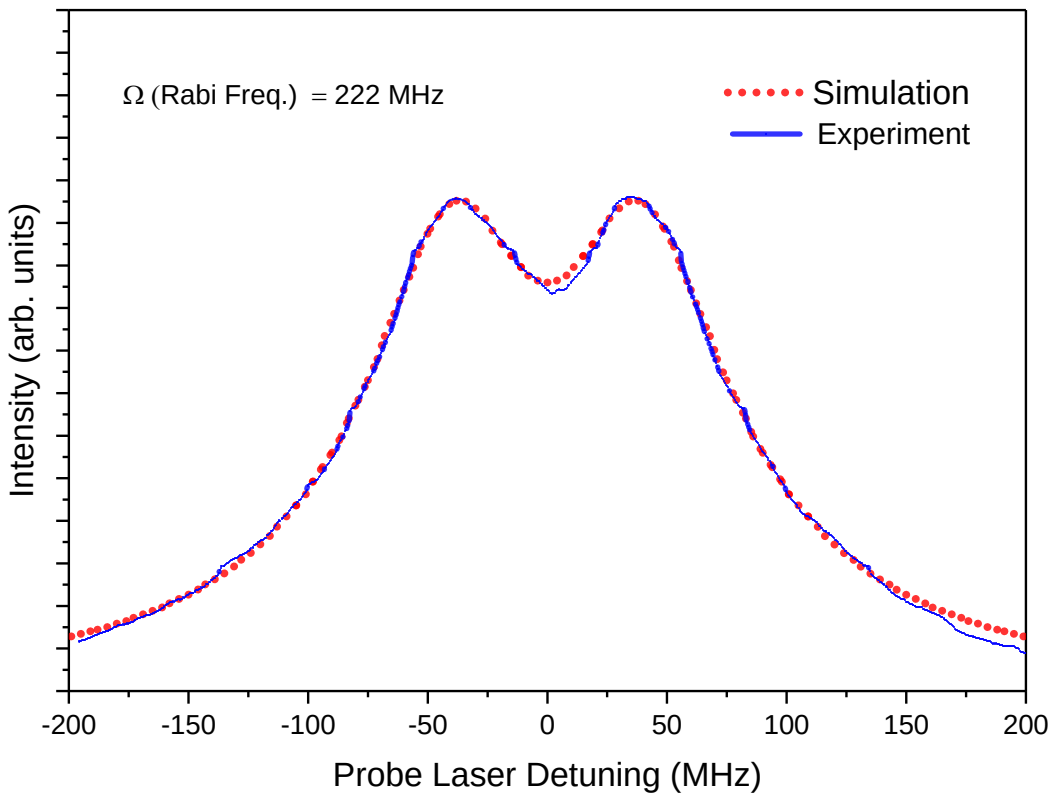

Figure 3.5 Autler-Townes Splitting spectra for Na_2 $6^1\Sigma_g^+(15,19) \rightarrow A^1\Sigma_g^+(15,20)$ transition.

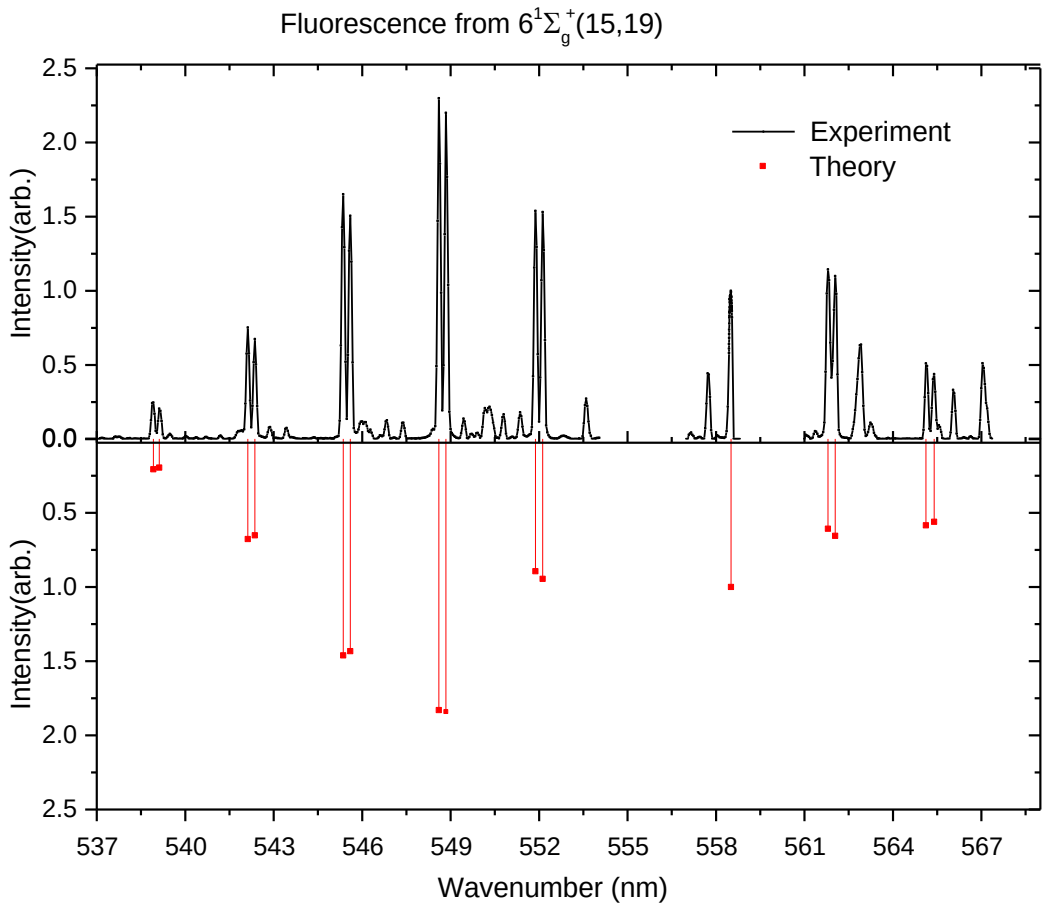

Figure 3.6 Resolved fluorescence from the Na_2 $6^1\Sigma_g^+(15,19)$ state to vibrational levels of the $A^1\Sigma_u^+$ state.

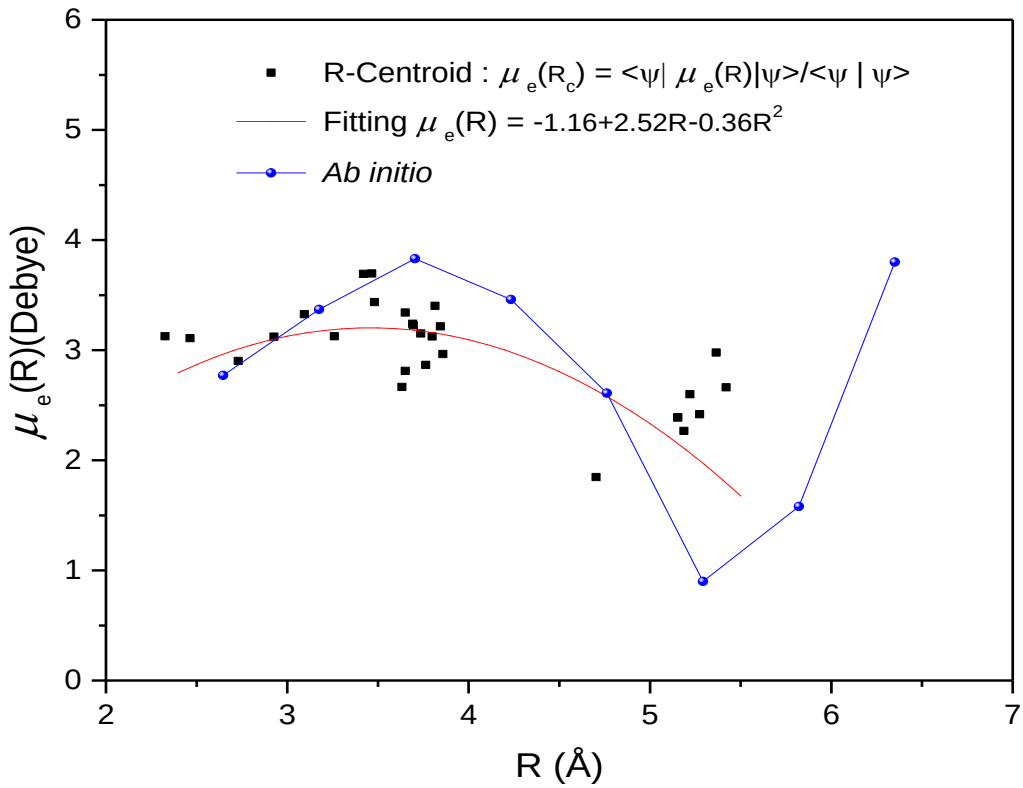

Figure 3.7 Electronic transition dipole moment function, $\mu_e(R)$, for the Na_2 $5^1\Sigma_g^+ \leftarrow A^1\Sigma_u^+$ electronic transition.

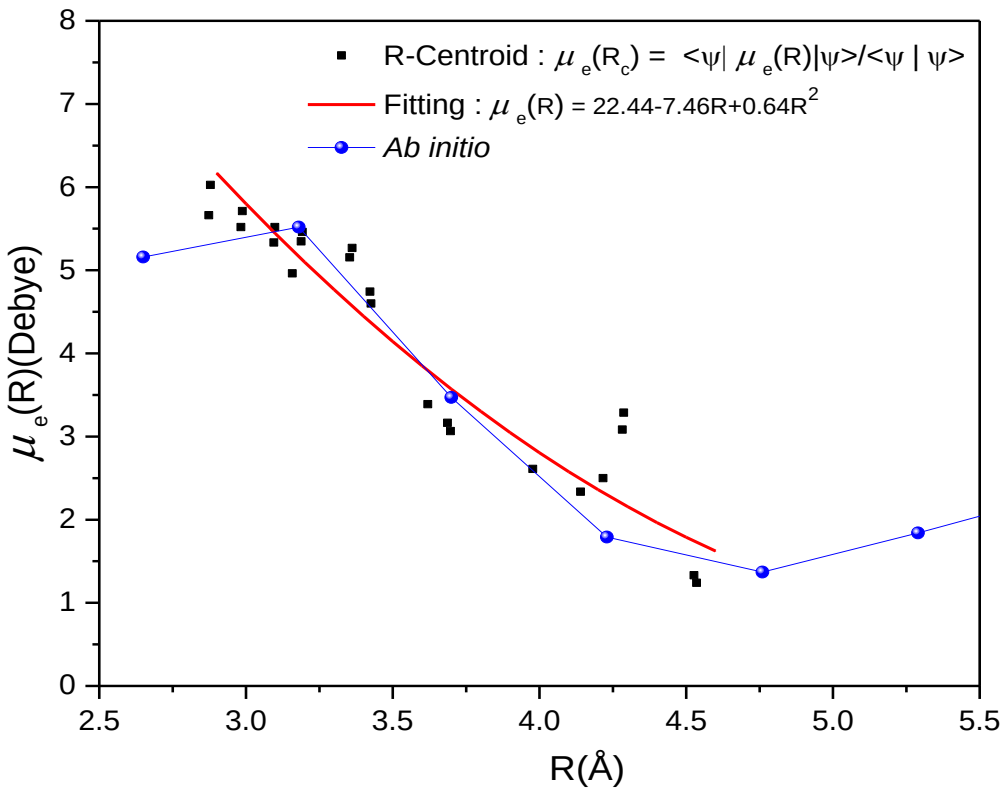

Figure 3.8 Electronic transition dipole moment function, $\mu_e(R)$, for the Na_2 $6^1\Sigma_g^+ \leftarrow A^1\Sigma_u^+$ electronic transition.

3.4 Conclusions

We have combined Autler-Townes splitting data for transition dipole matrix elements with resolved fluorescence spectral line intensity data from OODR resolved fluorescence to generate experimental transition dipole moment functions $\mu_e(R)$ for the $5^1\Sigma_g^+ \rightarrow A^1\Sigma_u^+$ and $6^1\Sigma_g^+ \rightarrow A^1\Sigma_u^+$ transitions of Na_2. For strong transitions, we have made use of the Autler-Townes splitting technique [14, 15, 20, 26, 27] to obtain absolute transition dipole moment matrix elements. For weaker transitions, we have used spectral line intensity data from resolved fluorescence spectra. By combining the Autler-Townes splitting based absolute measurements of the transition dipole matrix elements with the relative resolved fluorescence-based intensity measurements it was possible to expand the internuclear distance range of the experimental transition dipole moment mapping on an absolute scale for these transitions. The experimental results confirm a strong variation of these transition dipole moments as a function of internuclear distance. This is caused by the strong coupling of the Na_2 $5^1\Sigma_g^+$ and $6^1\Sigma_g^+$ electronic states with the $Na^+ + Na^-$ ion-pair potential. In the range of internuclear distances accessible by OODR excitation, we have also compared the experimental transition dipole moments with theoretical *ab initio* calculations, which also provide absolute transition dipole moments.

References

[1] A. Sanli, B. Beser, J.R. Edwardson, S. Magnier, E.H. Ahmed, A. Marjatta Lyyra, Electronic transition dipole moment and radiative lifetime calculations of sodium dimer ion-pair states, The Journal of Chemical Physics 143 (2015) 104304.

[2] C.C. Tsai, J.T. Bahns, W.C. Stwalley, Journal of Chemical Physics 100 (1994) 768-774.

[3] C.C. Tsai, J.T. Bahns, W.C. Stwalley, Journal of Molecular Spectroscopy 167 (1994) 429-436.

[4] T. Laue, P. Pellegrini, O. Dulieu, C. Samuelis, H. Knockel, F. Masnou-Seeuws, E. Tiemann, European Physical Journal D 26 (2003) 173-185.

[5] E. Ahmed, A. Hansson, P. Qi, T. Kirova, A. Lazoudis, S. Kotochigova, A.M. Lyyra, L. Li, J. Qi, S. Magnier, Journal of Chemical Physics 124 (2006) 084308

[6] N.W. Carlson, F.V. Kowalski, R.E. Teets, A.L. Schawlow, Identification of excited states in Na2 by two-step polarization labeling, Optics Communications 29 (1979) 302-306.

[7] G.Y. Yan, B.W. Sterling, A.L. Schawlow, Potential of the (5)Σ1g+ state of Na2 by two-step excitation spectroscopy, Journal of the Optical Society of America B 5 (1988) 2305-2310.

[8] L. Li, R.W. Field, Direct observation of high-lying 3.PI.g states of the sodium molecule by optical-optical double resonance, The Journal of Physical Chemistry 87 (1983) 3020-3022.

[9] H. Wang, L. Li, A.M. Lyyra, W.C. Stwalley, CW optical-optical double-resonance excitations of 39K2 Rydberg states, Journal of Molecular Spectroscopy 137 (1989) 304-311.

[10] T.-J. Whang, H. Wang, A.M. Lyyra, L. Li, W.C. Stwalley, Optical-optical double resonance spectroscopy of the Na2 21Πg state, Journal of Molecular Spectroscopy 145 (1991) 112-122.

[11] E. Kagi, N. Yamamoto, H. Fujiwara, M. Fukushima, T. Ishiwata, Optical–Optical Double Resonance Spectroscopy of the 1g(3P1)-A3Π (1u)-X1Σg+ Transition of I2, Journal of Molecular Spectroscopy 216 (2002) 48-51.

[12] J.T. Kim, H. Wang, J.T. Bahns, W.C. Stwalley, The 3 1Πg and 3 1Δg states of 39K2 studied by optical–optical double resonance spectroscopy, The Journal of Chemical Physics 102 (1995) 6966-6974.

[13] A.M.F. Lau, W.M. Huo, Molecular transition moment determination by Autler-Townes spectroscopy: D 1Πu-E,F 1Σg+ bands of H2, Chemical Physics Letters 157 (1989) 108-114.

[14] E.H. Ahmed, P. Qi, B. Beser, J. Bai, R.W. Field, J.P. Huennekens, A.M. Lyyra, Physical Review A 77 (2008).

[15] J.B. Qi, G. Lazarov, X.J. Wang, L. Li, L.M. Narducci, A.M. Lyyra, F.C. Spano, Physical Review Letters 83 (1999) 288-291.

[16] J. Qi, G. Lazarov, X. Wang, L. Li, L.M. Narducci, A.M. Lyyra, F.C. Spano, Erratum: Autler-Townes Splitting in Molecular Lithium: Prospects for All-Optical Alignment of Nonpolar Molecules [Phys. Rev. Lett. 83, 288 (1999)], Physical Review Letters 88 (2002) 229901.

[17] J. Qi, F.C. Spano, T. Kirova, A. Lazoudis, J. Magnes, L. Li, L.M. Narducci, R.W. Field, A.M. Lyyra, Physical Review Letters 88 (2002).

[18] E. Ahmed, A.M. Lyyra, Effect of Doppler broadening on Autler-Townes splitting in the molecular cascade excitation scheme, Physical Review. A (2007) Medium: X; Size: page(s) 053407-053407.053410.

[19] A. Lazoudis, E.H. Ahmed, L. Li, T. Kirova, P. Qi, A. Hansson, J. Magnes, A.M. Lyyra, Experimental observation of the dependence of Autler-Townes splitting on the probe and coupling laser wave-number ratio in Doppler-broadened open molecular cascade systems, Physical Review A 78 (2008) 043405.

[20] S.J. Sweeney, E.H. Ahmed, P. Qi, T. Kirova, A.M. Lyyra, J. Huennekens, Journal of Chemical Physics 129 (2008).

[21] E.H. Ahmed, P. Qi, A.M. Lyyra, Physical Review A 79 (2009).

[22] R. Stair, W.E. Schneider, J.K. Jackson, A New Standard of Spectral Irradiance, Applied Optics 2 (1963) 1151-1154.

[23] D.R. Skinner, R.E. Whitcher, J. Phys. E 5 (1972) 237.

[24] E. Ahmed, Autler-Townes Spectroscopy of Molecular Electronic Transition Dipole Moments in Doppler Broadened Systems, Ph.D. Thesis, Temple University, 2007.

[25] C. Noda, R.N. Zare, Relation between classical and quantum formulations of the Franck-Condon principle: The generalized R-Centroid approximation, Journal of Molecular Spectroscopy 95 (1982) 254-270.

[26] J. Qi, F.C. Spano, T. Kirova, A. Lazoudis, J. Magnes, L. Li, L.M. Narducci, R.W. Field, A.M. Lyyra, Physical Review Letters 88 (2002) 173003.

[27] A.M. Lyyra, H. Wang, T.J. Whang, W.C. Stwalley, L. Li, Physical Review Letters 66 (1991) 2724-2727.

CHAPTER 4

ELECTRONIC TRANSITION DIPOLE MOMENT AND RADIATIVE LIFETIME CALCULATIONS OF SODIUM DIMER ION-PAIR STATES

4.1 Introduction

We present here a description of a computational study of lifetimes and transition dipole moment matrix elements for the sodium dimer ion-pair states of $^1\Sigma_g^+$ symmetry. These electronic states have multiple wells and shoulders that broaden the potential energy wells. Previously, Dr. Magnier calculated the *ab initio* electronic transition dipole moment functions [1] that vary strongly with internuclear distance. These were used in the present calculations of lifetimes and transition dipole moment matrix elements. We calculated the lifetimes and they agree well with experimental values from the literature when available. We published this work in the Journal of Chemical Physics [2].

Alkali dimer M_2 and alkali hydride MH molecular electronic states with ion-pair character are known to exhibit multiple minima and shoulders in their potential energy curves [3-7]. This exotic behavior of the $^1\Sigma_g^+$ symmetry states is caused by avoided crossings of the zero-order covalent and ionic ($M^+ + M^-$) potential energy curves. In addition to exhibiting discontinuous slopes of vibrational G(v) and rotational B(v)

functions with increasing vibrational quantum number v, a pronounced variation of the electronic transition moment is predicted for regions of internuclear distance that involve avoided crossings of zero-order covalent or ionic configurations [8-10]. Some evidence for such behavior has been found in a few electronic states of alkali hydrides [4, 5, 11, 12]. In addition, in the lighter molecules such as H_2 and LiH, breakdown effects of the Born-Oppenheimer approximation have also been observed [4, 5, 13]. As a result of this, potential energy curves differ significantly from one isotopomer to the other. For the slightly heavier Li_2 molecule, the resulting anomalous isotope shifts are quite small [14]. The E-F, G-K and H-H states of H_2 have been studied extensively both theoretically and experimentally since the '70s [6]. For example, the E-F double minimum state of H_2 has served as a gateway state to higher lying excited states in double resonance spectroscopy [15] as well as for the study of photodissociation to their continua [16].

The Li_2 ion-pair states $3(E)^1\Sigma_g^+$ and $4(F)^1\Sigma_g^+$ have been well characterized both theoretically and experimentally [9, 17, 18] and the $4(F)^1\Sigma_g^+$ rovibrational levels exhibit interesting rovibrational isotopomer dependent predissociation behavior [19, 20] to the continuum of the $3(E)^1\Sigma_g^+$ state. The analogous Na_2 state $4(F)^1\Sigma_g^+$ does not predissociate [21].

Due to the poor Franck-Condon factors for excitation from the thermal population of the ground state via the $1(A)^1\Sigma_u^+$ state, these ion-pair states have been observed using either atomic fluorescence following predissociation [19, 20], ion detection with a thermal molecular sample [21-25], or in a molecular beam [26]. In a series of experiments S. R. Leone *et al.* have used the Li_2 $3(E)^1\Sigma_g^+$ state in femtosecond coherent

control wavepacket experiments for control of wave packet dynamics [27, 28], alignment effects in multiphoton coherent excitation [29], and the manipulation of rovibronic wavepacket compositions [30].

The Na_2 ion-pair $3^1\Sigma_g^+$, $4^1\Sigma_g^+$, $5^1\Sigma_g^+$ and $6^1\Sigma_g^+$ states, plotted in Figure 4.1, have been calculated by Sylvie Magnier *et al.* [10] using two effective potential methods. In these two *ab initio* approaches, potential energy curves (PECs) of $^1\Sigma_g^+$, $^1\Sigma_u^+$ highly excited states display strange patterns located at intermediate and large internuclear distances (5.3Å< R <21Å). Shoulders are found in the PECs of the $3^1\Sigma_g^+$ and $4^1\Sigma_g^+$ electronic states for 5.3Å< R <21Å, as well as a large avoided crossing between these curves.

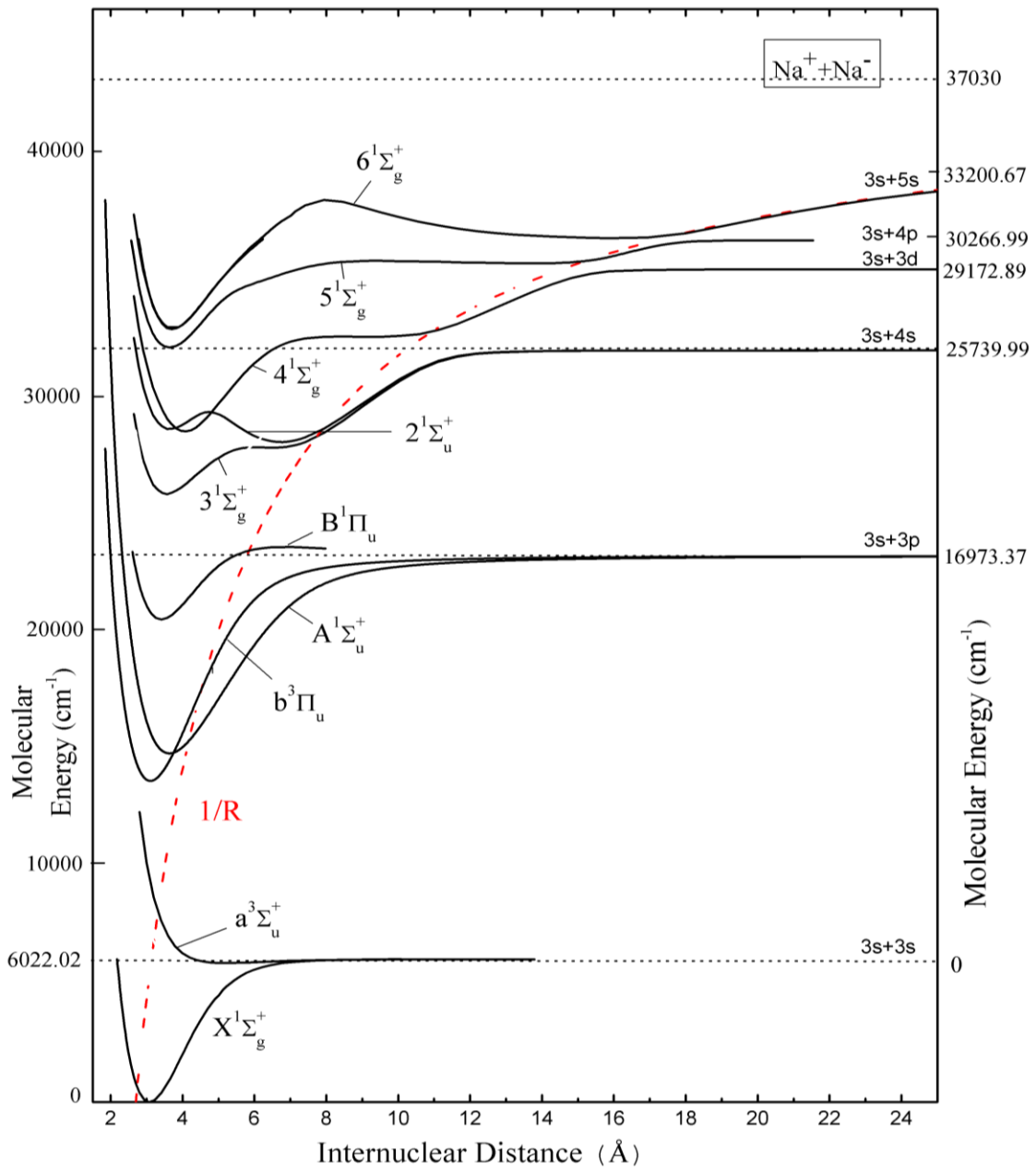

Figure 4.1 Selected potential energy curves of the Na_2 molecule excited states. The dotted line is the ion pair $Na^+ + Na^-$ Coulomb interaction function $e^2/(4\pi\varepsilon R)$, which crosses the region of the electronic states and causes the secondary wells and shoulders for these potential energy functions. The potential energy curves are from Refs.[10, 22-26, 31-35].

For *R* varying between 10.6Å and 18.5Å, two very close avoided crossings between the PECs of the $4\,^1\Sigma_g^+$, $5\,^1\Sigma_g^+$ and $6\,^1\Sigma_g^+$ electronic states are observed, which are due to the ionic-covalent interaction. A diabatic approach has been developed to extract from adiabatic calculations, the diabatic states dissociating into the ionic state ($Na^+ + Na^-$) and those correlated to a covalent state (Na(nl) + Na(n'l')) [36]. In these calculations, only the ionic ground state Na^- (^1S) has been considered and some of the observed structures correspond to crossings between relevant covalent and ionic energy curves as plotted in Figure 4.2. In order to model the ionic-covalent interaction and extend it to other molecular symmetries more accurately, in the *ab initio* calculations, Dr. Magnier has determined the lowest $^{1,3}S$, $^{1,3}P$ and, $^{1,3}D$ excited states of Na^- [37] through large atomic interaction configuration calculations including 3s-7s, 3p-7p, 3d-7d and 4f-6f orbitals. Dr. Magnier obtained for the ionic ground state, an energy of -0.209008au, which is in good agreement with the previously determined experimental -0.209884au [38] and *ab initio* -0.208813au [36] values.

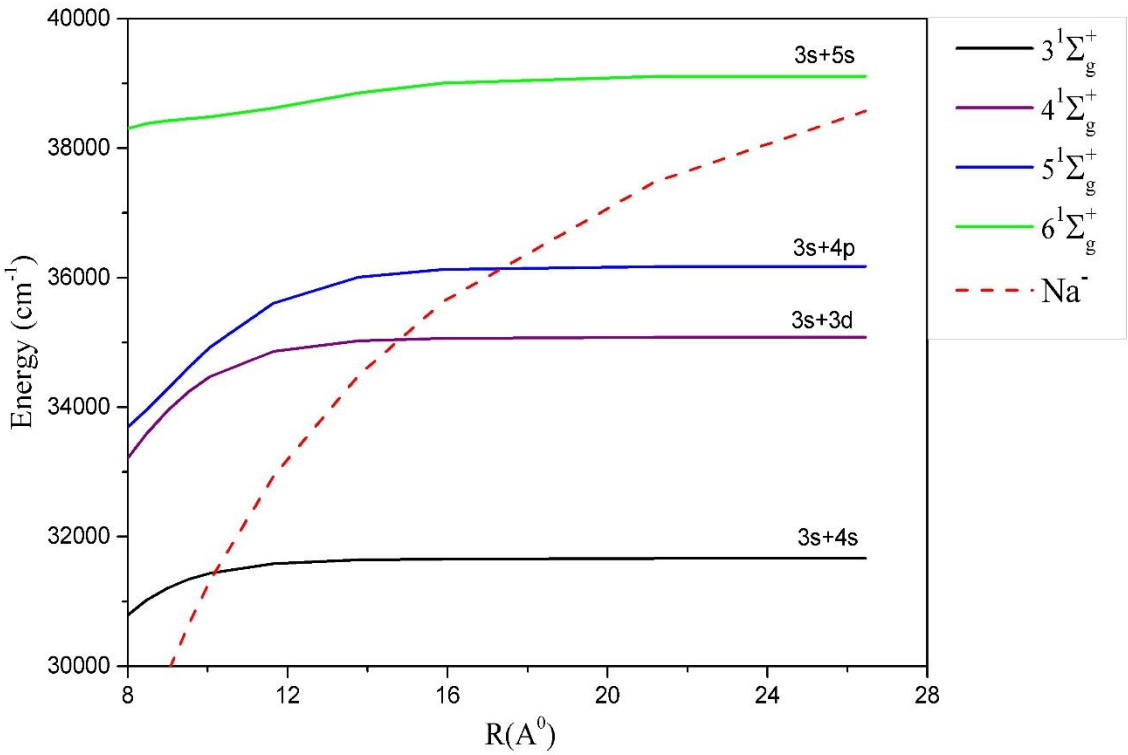

Figure 4.2 Diabatic potential energy curves for the $^1\Sigma_g^+$ states correlated to Na(3s) + Na (4s, 3d, 4p, 5s) and for the ionic ground state $Na^-(^1S)$.

The first $Na^{-}(^{1}S)$ ionic excited states are located below the atomic threshold Na(3p) at an energy of -41217.55 cm^{-1} and -40262.62 cm^{-1}, respectively. As displayed in Figure 4.3 (b), pseudo-crossings between ionic curves of these states and the PECs of $3^{1}\Sigma_{g}^{+}$ and $4^{1}\Sigma_{g}^{+}$ states are observed in the region of the shoulders. Similar remarks may be made for the potential energy curves of the $^{1}\Sigma_{u}^{+}$ states dissociating into the same asymptotes as shown in Figure 4.3 (a). The potential energy calculations have been supplemented by determination of the transition dipole moments (TDM) [1]. Variations of TDM for (3-6)$^{1}\Sigma_{g}^{+} \leftarrow {}^{1}\Sigma_{u}^{+}$ and (3-6)$^{1}\Sigma_{g}^{+} \leftarrow 2\,^{1}\Sigma_{u}^{+}$ transitions are presented in Figure 4.4. The TDM functions for (3-6)$^{1}\Sigma_{g}^{+} \leftarrow B^{1}\Pi_{u}$ transitions are shown in Figure 4.5. A crossing is observed between the TDM of the $3\,^{1}\Sigma_{g}^{+} \leftarrow B^{1}\Pi_{u}$ and $4\,^{1}\Sigma_{g}^{+} \leftarrow B^{1}\Pi_{u}$ transitions at 3.86Å, which corresponds to the position of a large avoided crossing between the two PECs. In the region of the shoulder, the $4\,^{1}\Sigma_{g}^{+} \leftarrow B^{1}\Pi_{u}$ TDM decreases with increasing R and approaches 0 at the end of the shoulder before increasing again and crossing the $5\,^{1}\Sigma_{g}^{+} \leftarrow B^{1}\Pi_{u}$ TDM at 14.8Å. This is very close to the position of the avoided crossing of the molecular potential energy curves. In the range of 6.35Å-15.87Å, the $5\,^{1}\Sigma_{g}^{+} \leftarrow B^{1}\Pi_{u}$ TDM is seen to be constant. When the pseudo-crossing occurs in the PECs with the ionic curve of the ground state, the $5\,^{1}\Sigma_{g}^{+} \leftarrow B^{1}\Pi_{u}$ TDM decreases to 0 with increasing *R* while for the $4\,^{1}\Sigma_{g}^{+} \leftarrow B^{1}\Pi_{u}$ TDM increases up to the value of the $5\,^{1}\Sigma_{g}^{+} \leftarrow B^{1}\Pi_{u}$ TDM. Because of the

potential well due to pseudo-crossings with ionic curves, a little peak is observed in $6^1\Sigma_g^+ \leftarrow B^1\Pi_u$ TDM, while the variation of TDM is more important for the $6^1\Sigma_g^+ \rightarrow 2^1\Sigma_u^+$ transition (Figure 4.4 (b)). Similar observations may be made for the transitions between the $2^1\Sigma_u^+$ and $(3\text{-}6)^1\Sigma_g^+$ states. The influence of ionic-covalent interaction is not negligible for these transition dipole moments and may induce strong variations as well as inversion of TDM values. The transition dipole moments of the $(3\text{-}6)\,X^1\Sigma_g^+ \leftarrow A^1\Sigma_u^+$ transitions are illustrated in Figure 4.4 (a) and Table 4.1 Table of transition dipole moment functions for each transitions that we have used in our calculation. Dipole moment functions are in Debye and internuclear distances are in atomic units. Unlike the Li_2 $4(F)^1\Sigma_g^+$ state, these ion-pair states do not predissociate and rovibrational energy levels with large R-centroid values have been observed by ion detection based Optical-Optical Double Resonance (OODR) [21-25] and fluorescence enhanced triple resonance spectroscopy [26].

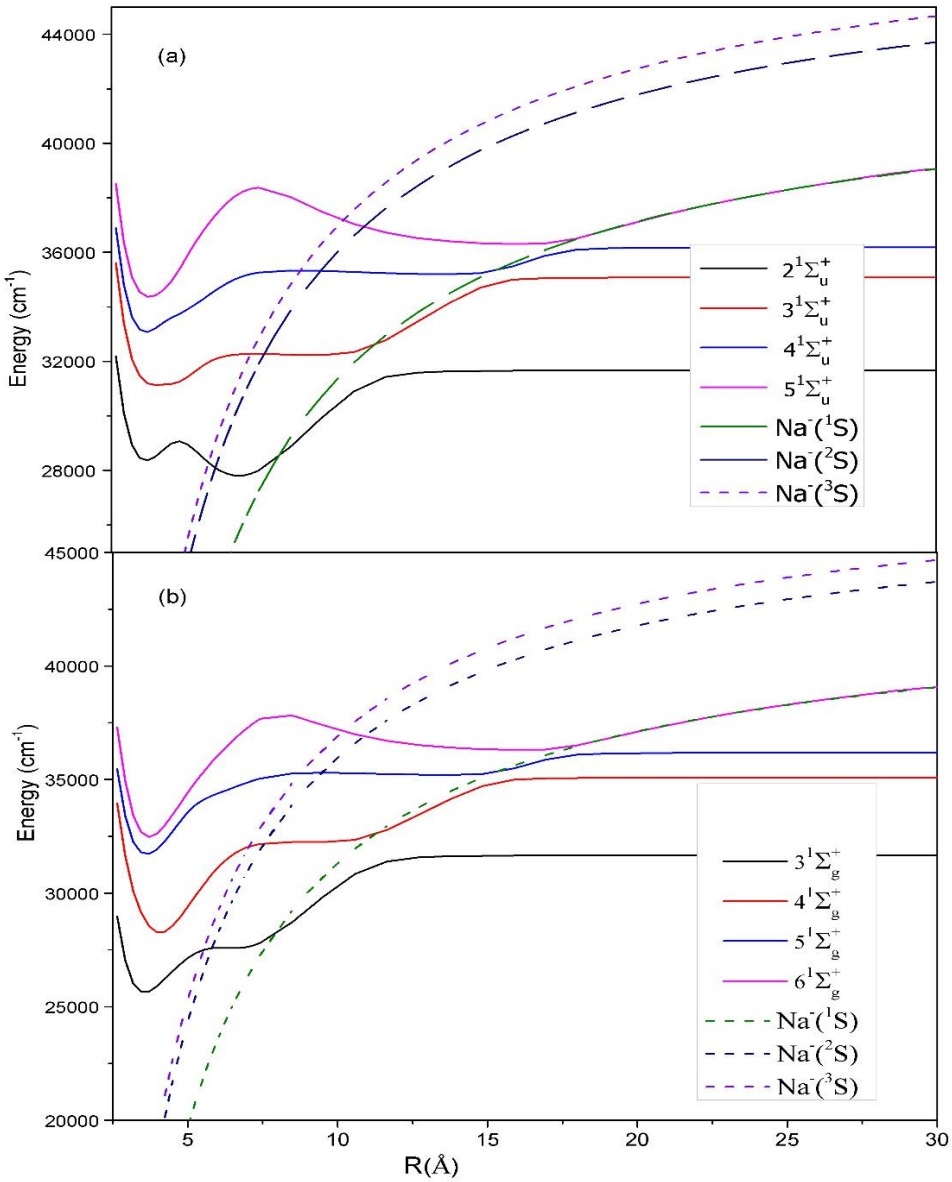

Figure 4.3 (a) Adiabatic potential energy curves of the (2-5) $^1\Sigma_u^+$ states crossed by the ionic $Na^-(^1S)$ state. (b) Adiabatic potential energy curves of the (3-6) $^1\Sigma_g^+$ states crossed by the ionic $Na^-(^{1\text{-}3}S)$ states.

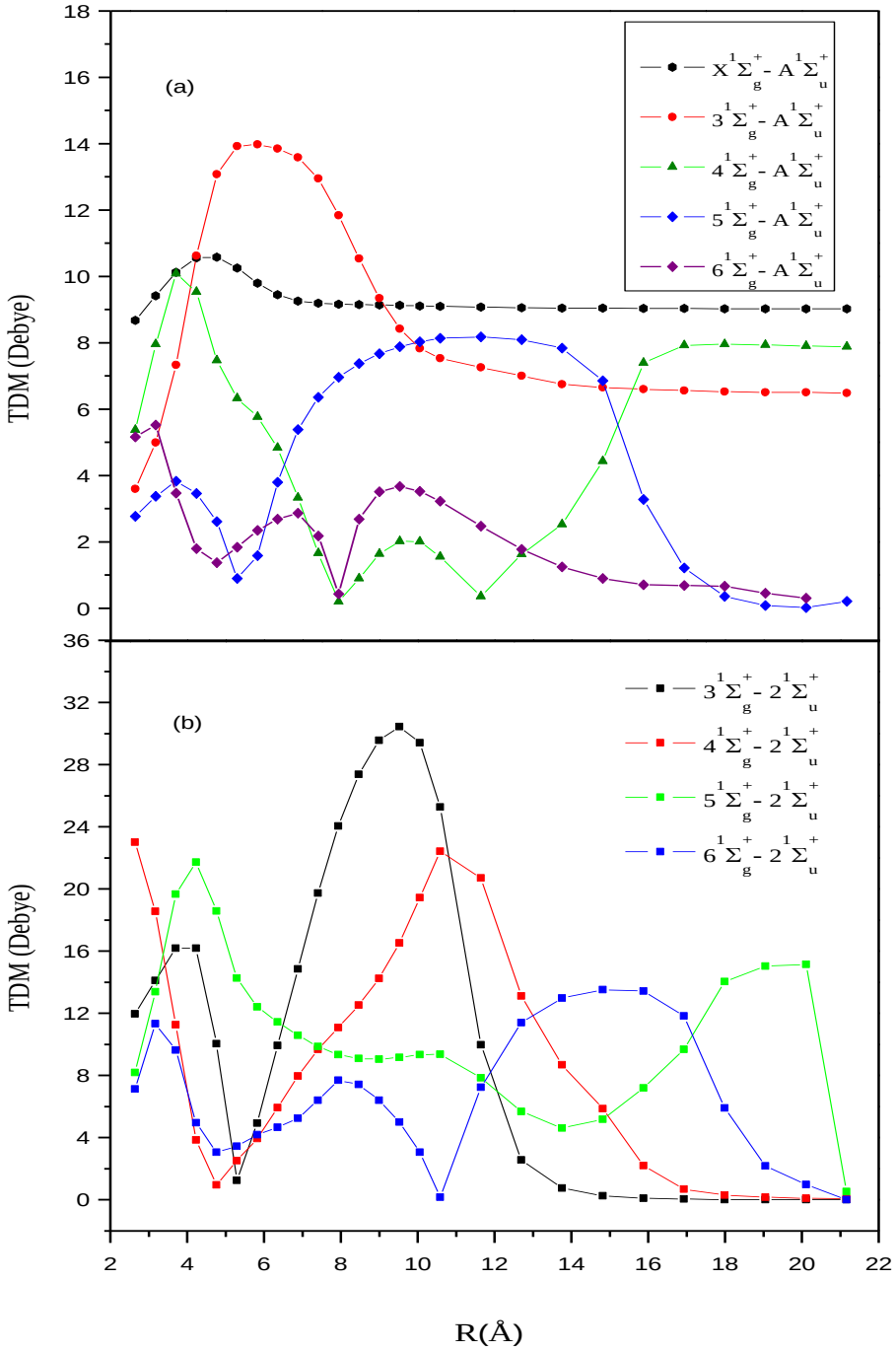

Figure 4.4 (a) Electronic transition dipole moment function, $\mu_e(R)$, plots for transitions between the low-lying excited and the first excited electronic state of the sodium dimer. (b) Electronic transition dipole moment function, $\mu_e(R)$, plots for transitions between the low-lying excited and the second excited electronic state of the sodium dimer.

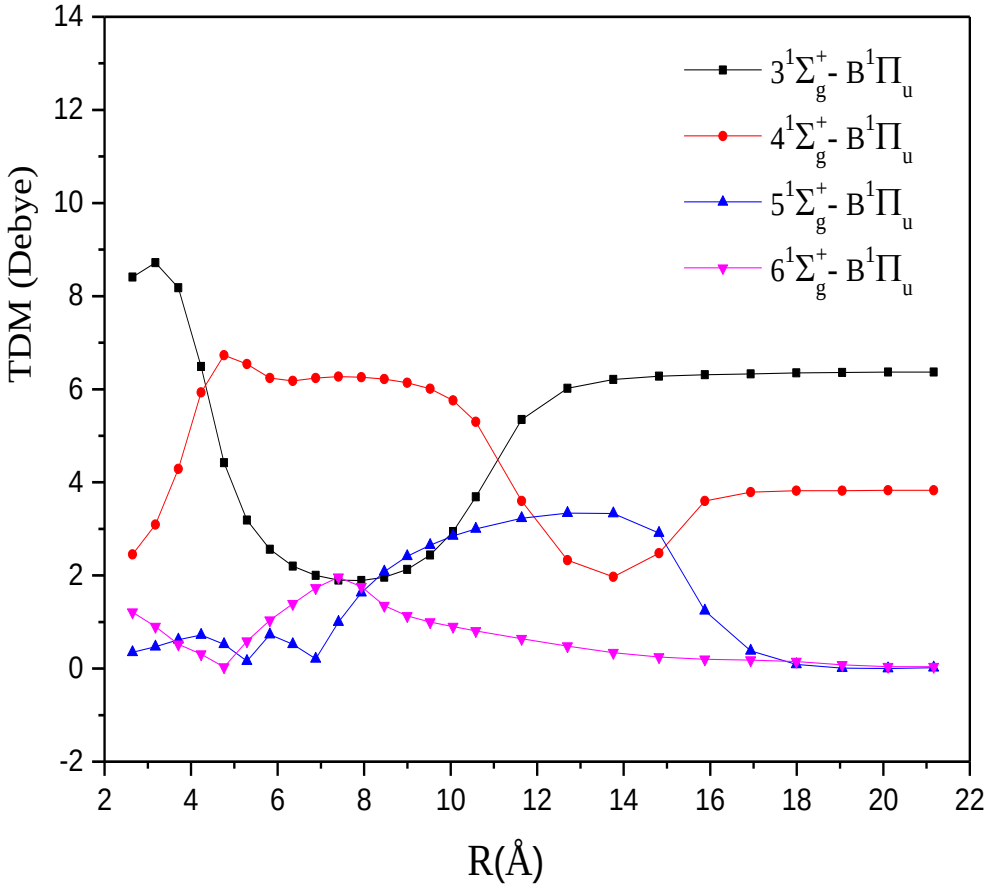

Figure 4.5 Electronic transition dipole moment functions, $\mu_e(R)$, for (3-6) $^1\Sigma_g^+ \leftarrow B^1\Pi_u$ transitions of Na_2.

The aim of this study is to present a road map for the critical parameters for an Autler-Townes spectroscopic probe of the predicted pronounced variation of the electronic transition dipole moments of the Na_2 dimer between the ion-pair states of $^1\Sigma_g^+$ symmetry and the $1(A)^1\Sigma_u^+$ state. The focus of this probe is on the avoided crossing regions between the zero-order covalent and ionic $Na^+ + Na^-$ configurations. Using quadruple resonance spectroscopy [39] and Autler-Townes splitting based measurements, the absolute magnitude of the electronic transition dipole moment matrix elements for the coupling laser rovibronic transitions $(3\text{-}6)^1\Sigma_g^+ \rightarrow 1(A)^1\Sigma_u^+$ can be obtained.

Using the Autler-Townes technique, the Rabi frequency $\Omega = \frac{\mu E}{\hbar}$ can be extracted from the observed Autler-Townes splitting spectrum for different R-centroid values as has been demonstrated for the $1(A)^1\Sigma_u^+ - 1(X)^1\Sigma_g^+$ systems of Na_2 and Li_2 [40, 41]. For regions of internuclear distance where the transition dipole moment matrix elements are smaller, calibrated fluorescence intensity data can be combined with absolute calibration of selected strong transitions for complete experimental mapping of the electronic transition dipole moment as demonstrated in Ref. [42]. Such accurate knowledge of the experimental transition dipole moment function is important to test the pronounced variation of the transition dipole moments as a function of internuclear distance predicted by *ab initio* calculations, and for understanding the structure of the excited states and their decay dynamics to gain more information for quantum control of molecular dynamics [27-30].

Traditional probes of the electronic transition dipole moment variation as a function of internuclear distance have also included lifetime measurements. However, since the upper state often decays to multiple lower lying electronic states, such measurements involve contributions from several transition dipole moments. In calibrated fluorescence measurements this no longer is a limiting factor since specific rovibronic transition intensities are observed [42]. However, the radiative lifetimes are of great interest in atomic/molecular physics or astrophysics since absolute transition probabilities can be determined from the measured lifetime of an excited level into the lower levels [43]. The radiative lifetime also plays a role in the simulations of the Autler-Townes splitting spectra, in particular in the spectral line wings. The line center of the Autler-Townes splitting spectrum is dominated by the Rabi frequency of the coupling laser [39, 40, 44-46].

4.2 Computational Background of Critical Parameters

An oscillating electric dipole moment can be induced with an external electromagnetic field and their interaction is resonant if the frequency of the field corresponds to the frequency of the transition between the upper and lower levels. Thus, the amplitude of this moment between the upper rovibrational level (v',J') and the lower rovibrational level (v'',J'') is referred as the transition dipole moment matrix element

$$\mu_{v'J'v''J''} \equiv \int \Psi_{v'J'}(R)\mu_e(R)\Psi_{v''J''}(R)dR = < v'J'|\mu_e(R)|v''J'' > \tag{4.1}$$

where R is the internuclear distance. The electronic transition moment μ_e can then be calculated from this matrix element using the R-centroid approximation

$$\mu_e(R_c) = \frac{<v'J'|\mu_e(R)|v"J'">}{<v'J'|v"J'">} \tag{4.2}$$

where $R_c = \frac{<v'J'|R|v"J">}{<v'J'|v"J">}$ is the R-centroid. The integral over the products of the upper and lower wavefunctions is the square root of the Franck-Condon factor $q_{v'J'v''J''} = |\int \Psi_{v'J'}(R)\ \Psi_{v"J"}(R)dR|^2$.

The absolute transition intensities either in absorption or emission spectra are related to the transition dipole moment matrix elements and the transition frequency. For emission, which we use to observe the resolved fluorescence spectra in our experiments, the transition probabilities are proportional to $|\mu^2\ |\nu^3$ for photon detectors.

The measurement of the absolute magnitude of the vibrationally averaged transition dipole matrix element is critical for comparison with theoretical values [40, 41]. Similarly calibrated intensity measurements are only relative but can be normalized to an absolute scale using the measured intensity for the same transition that was used for the Autler-Townes splitting measurement of the transition dipole moment matrix element [42]. The experimental Autler-Townes splitting spectra are theoretically simulated using standard density matrix formalism [39, 40, 44-46]. The transition dipole moment matrix elements are sensitively dependent on the wave functions of upper and lower states and provide crucial tests for the quality of computed wave functions.

In addition to the *ab initio* transition dipole moment values, we present here the background calculations needed for the mapping of the transition dipole moment functions for the (3,4,5) $^1\Sigma_g^+$ states to the 1(A) $^1\Sigma_u^+$ state of Na_2 molecule using the Autler-Townes effect. We have calculated radiative lifetimes of the ion-pair $^1\Sigma_g^+$ states and the first excited $A\,^1\Sigma_u^+$ state, electronic transition dipole moment matrix elements, and Franck-Condon factors for the sodium dimer. The main purpose of this paper is to identify optimal quadruple resonance [39] excitation pathways to probe Na_2 ion-pair $^1\Sigma_g^+ \leftarrow A\,^1\Sigma_u^+$ transition dipole moment functions.

As indicated above, the radiative lifetimes of the upper and lower states of the coupling laser are needed in the simulations of the Autler-Townes split coupling laser transition line wings. The radiative lifetimes, to be used in the AT simulations, are calculated from the Einstein coefficients A_{ik} for spontaneous emission using the computer program called LEVEL [47]. This program uses the previously obtained experimental (when available) or *ab initio* potential energy curves and transition dipole moments of the specific transitions which are presented here for the first time. It then solves the radial Schrödinger equation and produces the Einstein coefficients, Franck-Condon factors, and transition dipole moment matrix elements. We present the results of the calculations below.

4.3 Pseudopotential Calculation of Electronic Transition Dipole Moments

The transition dipole moments between various pairs of electronic states of Na_2 have been computed by Magnier *et al*. [1] over a large range of internuclear distances $5a_0 < R < 40a_0$. Molecular energies and two-electron wave functions have been determined through configuration-interaction (CI) calculations in the framework of the pseudopotential method. Details of the method and the basis sets used in this work may be found in Ref. [10]. The expectation value of the operator $\sum_{i=1}^{2} r_i$ has been estimated using the basis set of CI two-electron wave functions. The absolute values of the transition dipole moment functions for the transitions $^1\Sigma_g^+ \rightarrow A^1\Sigma_u^+$ are listed in Table 4.1 as a function of internuclear distance.

4.4 Lifetime Calculations

We have calculated the radiative lifetimes, τ, of the ion-pair $(3,4,5)^1\Sigma_g^+$ states of the Na_2 molecule rovibrational levels and compared them with the experimental results from the literature when available. The lifetime is simply the inverse of the total decay rate of the excited level to all possible lower energy levels. We denote with τ_i the lifetime of the excited level |i> , with A_{ik} the total decay rate of the excited level |i>, and with A_{ik} the decay rate of the excited level |i> to the lower level |k>. The A_{ik} are known as the Einstein coefficients, which runs over all possible rovibrational transitions. Therefore we can write

$$\tau_i = A_i^{-1} = (\Sigma A_{ik})^{-1}. \quad (4.3)$$

Using the calculated wavefunctions, the LEVEL program calculates the transition quantities, *i.e*. frequencies of the all possible rovibrational transitions, Franck-Condon factors, transition dipole moment matrix elements, and Einstein coefficients. In addition to radiative lifetimes, we also present the results for the transition dipole moment matrix elements and Franck-Condon factors. The Einstein coefficient for one single decay channel from the upper level (v',J') to the lower level (v'',J'') is represented by $A_{v'J'v''J''} = k\frac{S_{J'J''}}{g'(2J'+1)}\nu^3|\mu|^3$.

ν is the transition frequency, μ is the transition dipole moment between the two levels, $S_{J'J''}$ is the Hönl-London rotational intensity factor; g is the degeneracy factor which is 1 for $\Lambda = 0$, and 2 for $\Lambda \neq 0$ states. For S = 0 that the line strengths are normalized to (2J+1) for Σ–Σ transitions and to 2(2*J*+1) for all other *singlet–singlet* transitions. The total decay rate of the excited state rovibrational level is obtained by summing up all the individual Einstein A coefficients, $A_{v'J'} = \sum_{v''J''} A_{v'J'v''J''}$. We have calculated the individual rovibrational level decay rates, and added them up to obtain the total decay rate.

Table 4.1 Table of transition dipole moment functions for each transitions that we have used in our calculation. Dipole moment functions are in Debye and internuclear distances are in atomic units.

R a.u	$A^1\Sigma_u^+ \downarrow X^1\Sigma_g^+$	$3^1\Sigma_g^+ \downarrow A^1\Sigma_u^+$	$3^1\Sigma_g^+ \downarrow B^1\Pi_u$	$4^1\Sigma_g^+ \downarrow A^1\Sigma_u^+$	$4^1\Sigma_g^+ \downarrow B^1\Pi_u$	$5^1\Sigma_g^+ \downarrow A^1\Sigma_u^+$	$5^1\Sigma_g^+ \downarrow B^1\Pi_u$	$5^1\Sigma_g^+ \downarrow 2^1\Sigma_u^+$	$6^1\Sigma_g^+ \downarrow A^1\Sigma_u^+$	$6^1\Sigma_g^+ \downarrow B^1\Pi_u$	$6^1\Sigma_g^+ \downarrow 2^1\Sigma_u^+$
5.00	8.67	3.59	8.41	5.37	2.45	2.77	0.35	8.18	5.16	1.21	7.13
6.00	9.42	4.99	8.72	7.95	3.09	3.37	0.47	13.39	5.52	0.90	11.32
7.00	10.12	7.33	8.18	10.08	4.29	3.83	0.62	19.67	3.47	0.52	9.63
8.00	10.56	10.62	6.49	9.53	5.93	3.46	0.72	21.72	1.79	0.31	4.95
9.00	10.58	13.08	4.42	7.47	6.73	2.61	0.52	18.59	1.37	0.03	3.07
10.00	10.25	13.92	3.19	6.32	6.54	0.90	0.16	14.26	1.84	0.59	3.44
11.00	9.80	13.98	2.56	5.76	6.24	1.58	0.73	12.42	2.35	1.04	4.19
12.00	9.45	13.85	2.20	4.83	6.18	3.80	0.52	11.45	2.68	1.39	4.67
13.00	9.26	13.59	2.00	3.33	6.24	5.38	0.21	10.59	2.86	1.73	5.27
14.00	9.19	12.95	1.90	1.66	6.27	6.36	1.00	9.85	2.18	1.96	6.42
15.00	9.16	11.84	1.89	0.20	6.26	6.96	1.63	9.35	0.43	1.76	7.71
16.00	9.15	10.54	1.96	0.90	6.22	7.37	2.08	9.10	2.68	1.35	7.43
17.00	9.14	9.34	2.13	1.64	6.14	7.67	2.41	9.04	3.51	1.13	6.41
18.00	9.13	8.42	2.44	2.02	6.01	7.88	2.65	9.15	3.67	1.00	5.02
19.00	9.11	7.83	2.94	2.01	5.76	8.03	2.85	9.33	3.52	0.90	3.06
20.00	9.10	7.53	3.69	1.55	5.30	8.13	3.00	9.37	3.22	0.81	0.18
22.00	9.08	7.26	5.35	0.35	3.60	8.18	3.23	7.85	2.47	0.64	7.23
24.00	9.06	7.00	6.02	1.63	2.33	8.09	3.34	5.68	1.77	0.48	11.39
26.00	9.05	6.75	6.21	2.52	1.97	7.84	3.33	4.62	1.24	0.34	12.97
28.00	9.04	6.65	6.28	4.43	2.48	6.85	2.91	5.18	0.89	0.25	13.53
30.00	9.03	6.60	6.31	7.39	3.60	3.28	1.24	7.19	0.70	0.20	13.43
32.00	9.03	6.56	6.33	7.92	3.79	1.21	0.38	9.68	0.68	0.18	11.82
34.00	9.02	6.53	6.35	7.95	3.82	0.35	0.09	14.05	0.66	0.15	5.90
36.00	9.02	6.51	6.36	7.93	3.82	0.08	0.01	15.05	0.45	0.08	2.18
38.00	9.02	6.50	6.37	7.90	3.83	0.02	0.00	15.15	0.30	0.04	0.99
40.00	9.02	6.48	6.37	7.88	3.83	0.21	0.02	0.52	5.33	5.12	0.00

4.5 The Overview of Na_2 Electronic States

There were two different experimental data sets that have been used to map the potential energy curve of the $X^1\Sigma_g^+$ state available from the literature; *(i)* Kusch *et al.* [34] and *(ii)* Babaky *et al.* [31]. The latter, which was used in our calculations, provided the $X^1\Sigma_g^+$ state up to the maximum vibrational level $v = 62$ with the outer turning point of vibration at R=11.2310124 Å with energy of 6017.8555 cm^{-1} above the ground state minimum.

For the calculations of the $A^1\Sigma_u^+$ state lifetimes and transition dipole moment matrix elements; potential energy curves from Ref.[33] and from Ref.[31] for the $A^1\Sigma_u^+$ and $X^1\Sigma_g^+$ states are used, respectively. The potential energy curve is presented in Figure 4.1. The $A^1\Sigma_u^+$ state only undergoes one allowed electronic transition, which is to the singlet ground $X^1\Sigma_g^+$ state. According to the Hönl-London intensity factors, Σ-Σ transitions decay only to lower rotational levels of the P and R branches, where P and R represent $J''=J'+1$ and $J''=J'-1$ rotational transitions, respectively. As can be seen in Figure 4.4 (a), the transition dipole moment function is biggest between R~3.5 – 6.0 Å. This results in the strongest transitions around the same region, thus leading to larger Einstein A coefficients and shorter lifetimes. The lifetime results for $A^1\Sigma_u^+$ vibrational levels up to $v = 52$ are presented in Figure 4.6 for the rotational quantum number J=1. The plot shows that the lifetime is shorter with larger dipole moment.

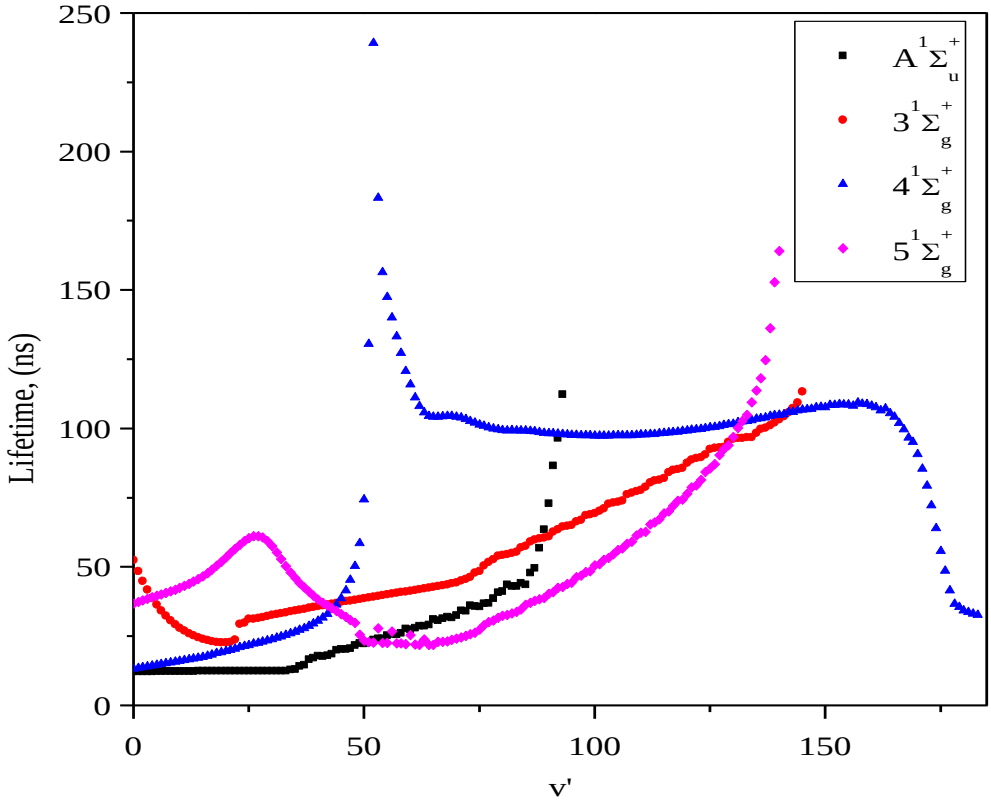

Figure 4.6 Plot of the radiative lifetime values versus the vibrational levels of the $A^1\Sigma_u^+$ $3^1\Sigma_g^+$, $4^1\Sigma_g^+$ and $5^1\Sigma_g^+$ states of Na_2.

For the higher vibrational levels, $v > 30$ the decay to the continuum of the ground state becomes more significant [4, 5]. We have compared our results with the experimental data of Baumgartner *et al.* [48] for various rovibrational levels of Na_2.

For the $3^1\Sigma_g^+$ state, there are two allowed decay transitions to the lower electronic states; *(i)* $3^1\Sigma_g^+ \rightarrow B^1\Pi_u$ and *(ii)* $3^1\Sigma_g^+ \rightarrow A^1\Sigma_u^+$. For the calculations of the $3^1\Sigma_g^+$ state lifetimes and transition dipole moment matrix elements; potential energy curves of the $3^1\Sigma_g^+$ [22], $A^1\Sigma_u^+$ [33] and $B^1\Pi_u$ [34, 35] states were used. The inner well of the $B^1\Pi_u$ state is from Ref.[34] and the potential barrier is from Ref.[35]. The lifetime results for this state are presented in Figure 4.6 up to $v = 145$ rovibrational levels for the rotational quantum number *J*=1. For the inner well, where the vibrational number is smaller than 20, lifetimes decrease with increasing v. Lifetimes and transition dipole moments show rapid changes around shoulders and second minima of the potentials. This can be observed in Figure 4.6. At $v = 23$, lifetimes show a increase with increasing v.

For the $4^1\Sigma_g^+$ state, there are two allowed fluorescence decay channels to lower states; *(i)* $4^1\Sigma_g^+ \rightarrow B^1\Pi_u$ and *(ii)* $4^1\Sigma_g^+ \rightarrow A^1\Sigma_u^+$ transitions. The potential energy curve for the $4^1\Sigma_g^+$ state is from Ref.[23] and for the $B^1\Pi_u$ state from Refs. [34, 35]. We have calculated the individual rovibrational level decay rates and added them up for the total decay rate. The lifetime results for this state are presented in Figure 4.6 up to $v = 185$ for the rotational quantum number *J* =1. Transition dipole moment matrix elements of the rovibrational transitions from the $4^1\Sigma_g^+$ state to the $A^1\Sigma_u^+$ state are presented in Figure 4.9. The lifetimes increase with increasing v for the inner well up to $v = 52$ and then

starts decreasing past the shoulder for $v > 52$, which is consistent with the *ab initio* transition dipole moment function in Figure 4.4 (a).

For the $5^1\Sigma_g^+$ state, there are three allowed electronic transitions to the lower electronic states; *(i)* $5^1\Sigma_g^+ \rightarrow B^1\Pi_u$, *(ii)* $5^1\Sigma_g^+ \rightarrow A^1\Sigma_u^+$, and *(iii)* $5^1\Sigma_g^+ \rightarrow 2^1\Sigma_u^+$. The potential energy curve of the $5^1\Sigma_g^+$ state is taken from Ref.[24] and the $B^1\Pi_u$ state is from Ref.[34, 35]. We have calculated the individual rovibrational level decay rates and added them up for the total decay rate. The results are presented in Figure 4.6 up to $v = 140$ for the rotational quantum number *J*=1. Transition dipole moment matrix elements of the rovibrational transitions from $5^1\Sigma_g^+$ to $A^1\Sigma_u^+$ are also presented in Figure 4.10 (d). Comparing the total lifetime plot in Figure 4.6 to the *ab initio* curve for $5^1\Sigma_g^+$ state in Figure 4.3(b), one can see the inverse correlation. Lifetimes are the smallest at $v' = 62$, while the *ab initio* dipole moment function reaches its maximum value. Lifetimes are larger for $v' > 62$ where the dipole moments are smaller as shown in Figure 4.4 (a). Transition dipole moment matrix elements of rovibrational transitions from $6^1\Sigma_g^+$ to $A^1\Sigma_u^+$ are also presented in Figure 4.11.

. For the $6^1\Sigma_g^+$ state There are three allowed transitions to the lower lying electronic states ; *(i)* $6^1\Sigma_g^+ \rightarrow B^1\Pi_u$, *(ii)* $6^1\Sigma_g^+ \rightarrow A^1\Sigma_u^+$, and *(iii)* $6^1\Sigma_g^+ \rightarrow 2^1\Sigma_u^+$. We have calculated the individual rovibrational level decay rates and added them up for the total decay rate, and results are presented in Figure 4.12 up to $v' = 304$. The $6^1\Sigma_g^+$ state has one inner well [25], one outer well [26] and a potential barrier in between [10]. That

makes it more difficult to handle this state computationally than the other electronic states. The inner well is labeled in red and the outer well in black in Figure 4.12. Figure 4.13 shows representative wavefunctions for vibrational levels belonging to the inner and outer wells of the $6^1\Sigma_g^+$ electronic state. The *ab initio* transition dipole moment function for the $6^1\Sigma_g^+ \rightarrow A^1\Sigma_u^+$ transition and the potential energy functions of the $6^1\Sigma_g^+$ and $A^1\Sigma_u^+$ states are presented in Figure 4.14. The lifetimes for the inner well and the outer well vibrational levels show quite different behaviors. Levels for $v < 40$ all belong to the inner well. At $v = 40$, some vibrational levels belong to the inner well and others belong to the outer well. Lifetimes of the vibrational levels belonging to the outer well are distinctly longer than those of levels belonging to the inner well. Lifetimes increase with increasing v for the inner well levels and a decrease with increasing v for the outer well levels.

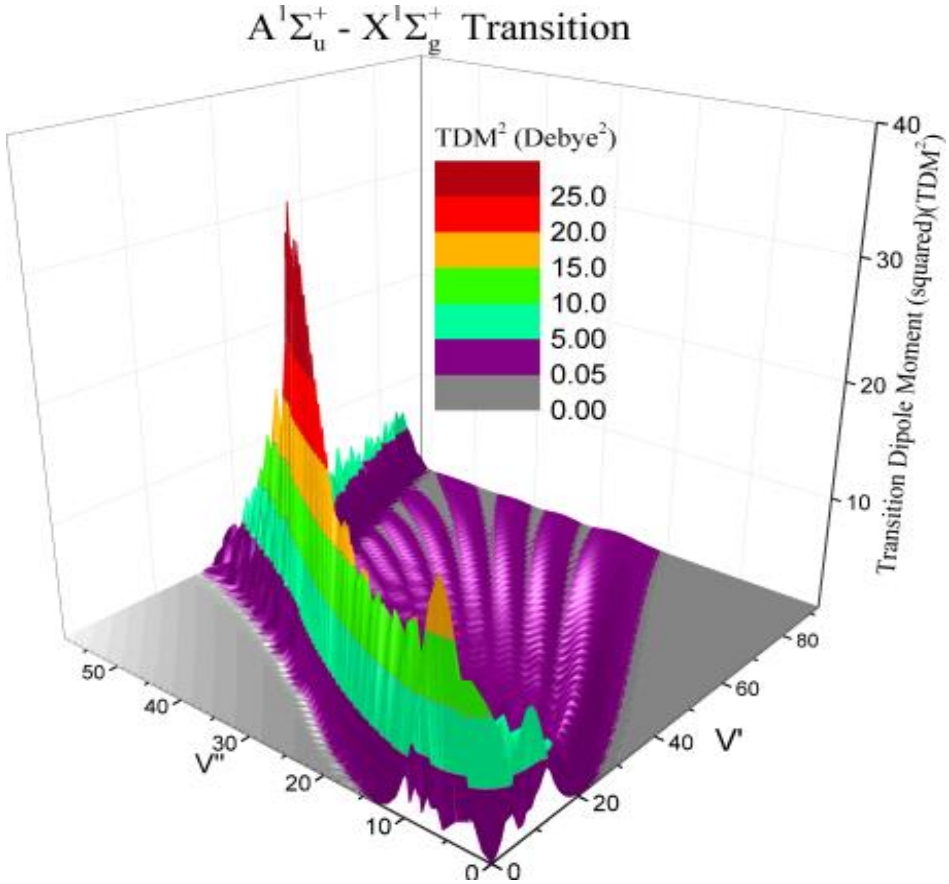

Figure 4.7 Mapping of the transition dipole moment matrix elements as a function of rovibrational levels for transitions between the electronic states (a) $A^1\Sigma_u^+$ and $X^1\Sigma_g^+$ of Na_2.

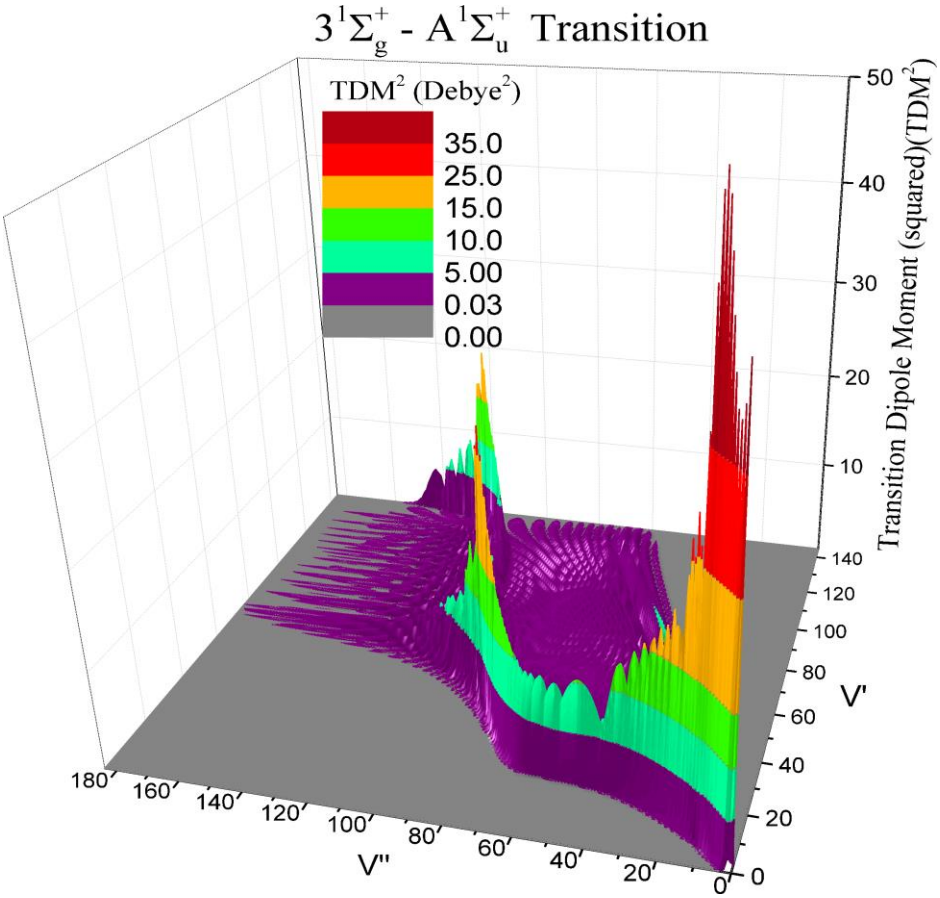

Figure 4.8 Mapping of the transition dipole moment matrix elements as a function of rovibrational levels for transitions between the electronic states $3^1\Sigma_g^+$ and $A^1\Sigma_u^+$ of Na_2.

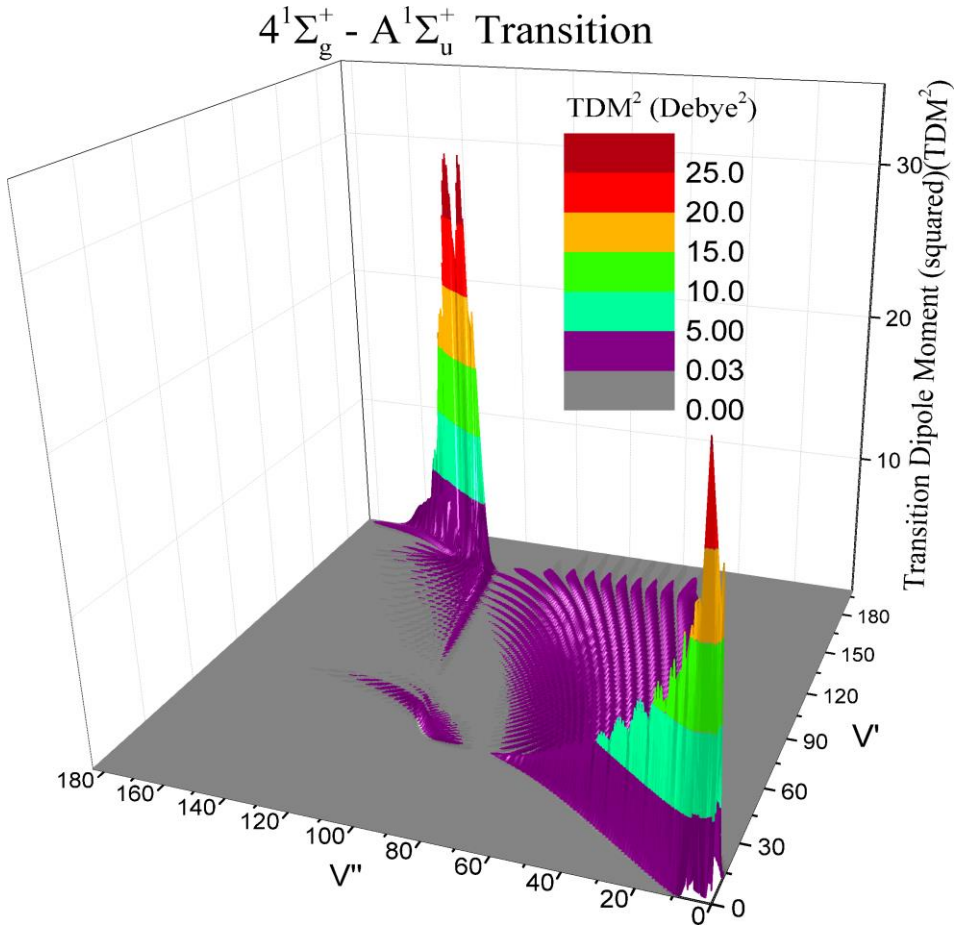

Figure 4.9 Mapping of the transition dipole moment matrix elements as a function of rovibrational levels for transitions between the electronic states $4^1\Sigma_g^+$ and $A^1\Sigma_u^+$ of Na_2.

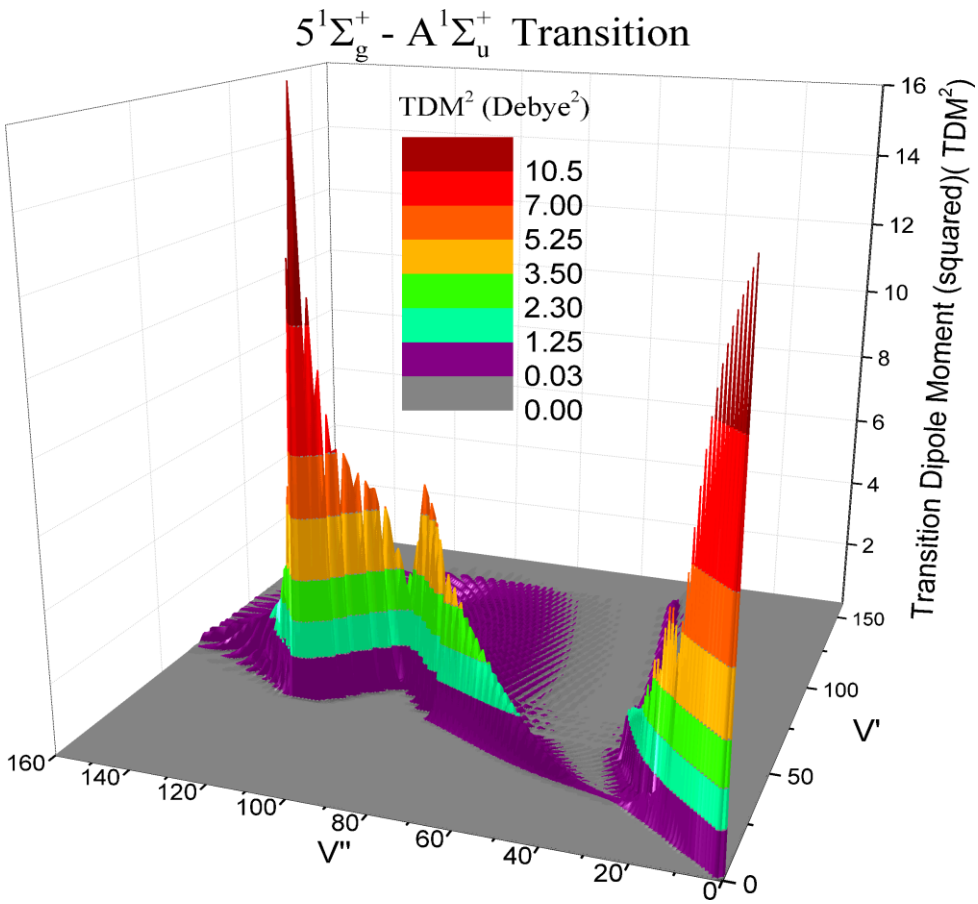

Figure 4.10 Mapping of the transition dipole moment matrix elements as a function of rovibrational levels for transitions between the electronic states $5^1\Sigma_g^+$ and $A^1\Sigma_u^+$ of Na_2.

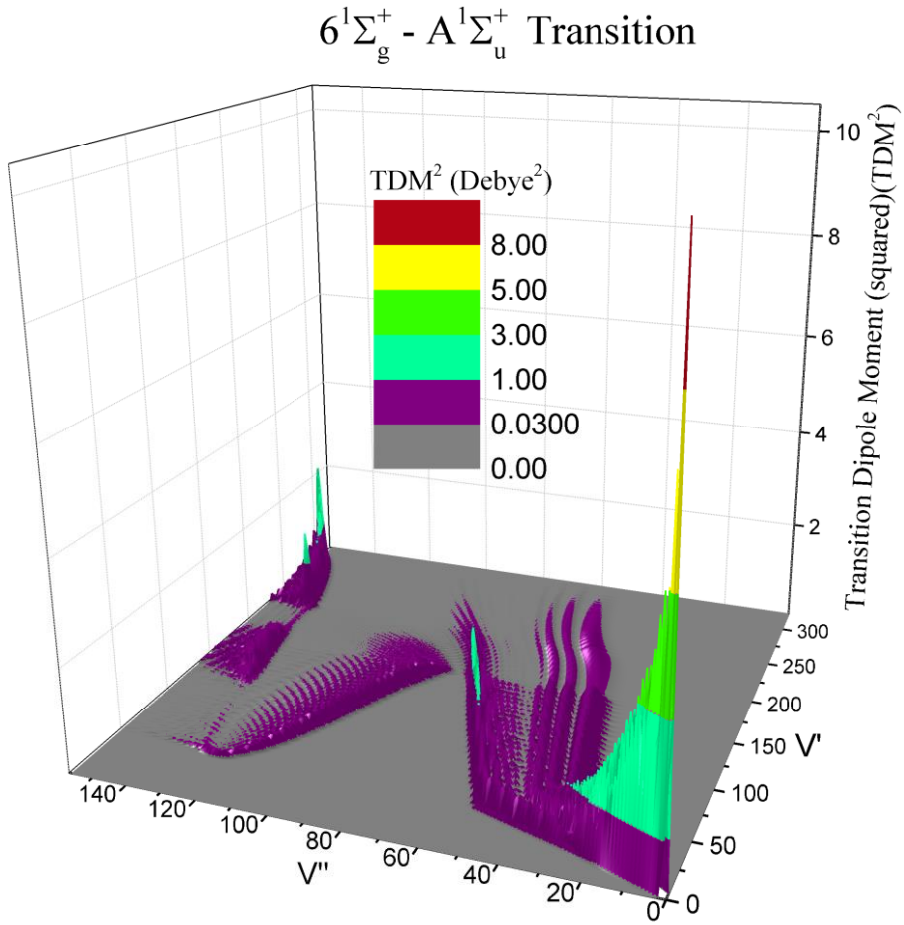

Figure 4.11 Mapping of the transition dipole moment matrix elements as a function of rovibrational levels for transitions between the electronic states $6^1\Sigma_g^+$ and $A^1\Sigma_u^+$ of Na_2.

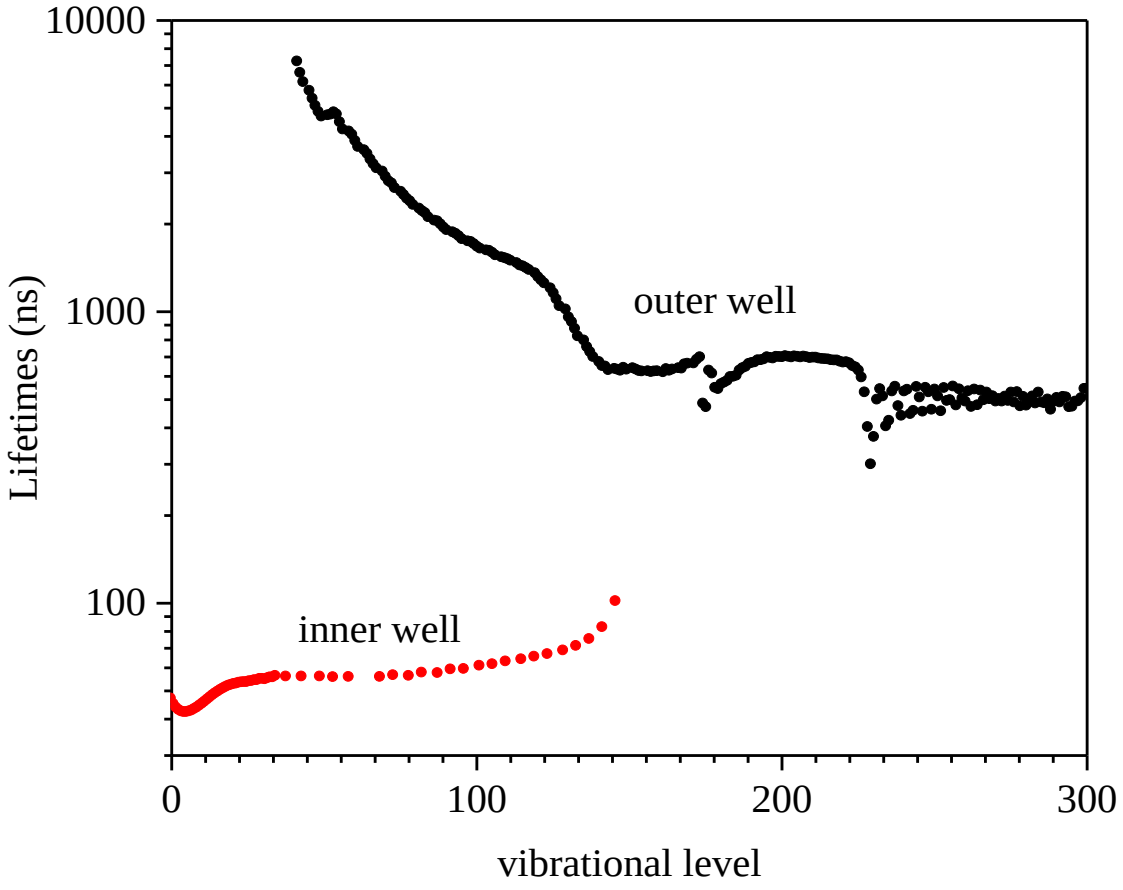

Figure 4.12 Radiative lifetimes of the vibrational levels of the $6^1\Sigma_g^+$ state of Na_2.

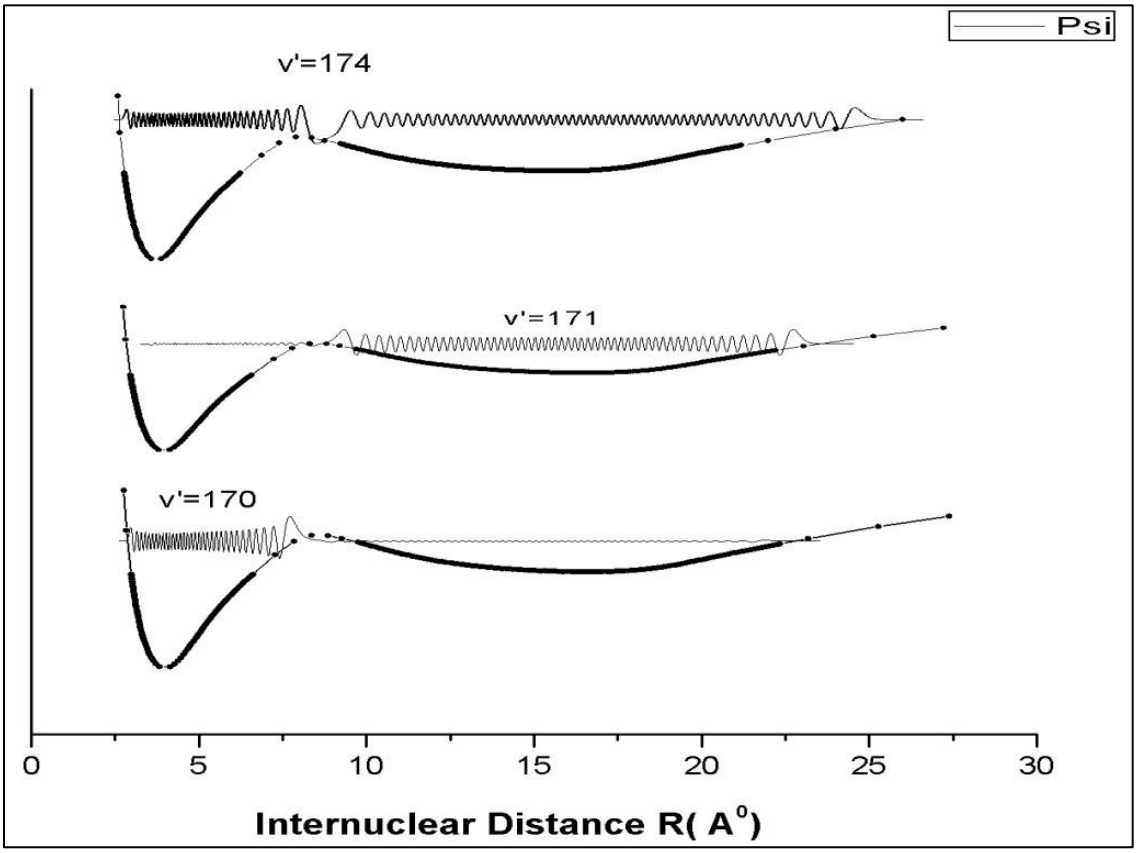

Figure 4.13 Vibrational wavefunctions for representative inner-well ($v' = 170$), outer-well ($v' = 171$) and above the barrier ($v' = 174$) vibrational levels of the $6^1\Sigma_g^+$ state of Na_2.

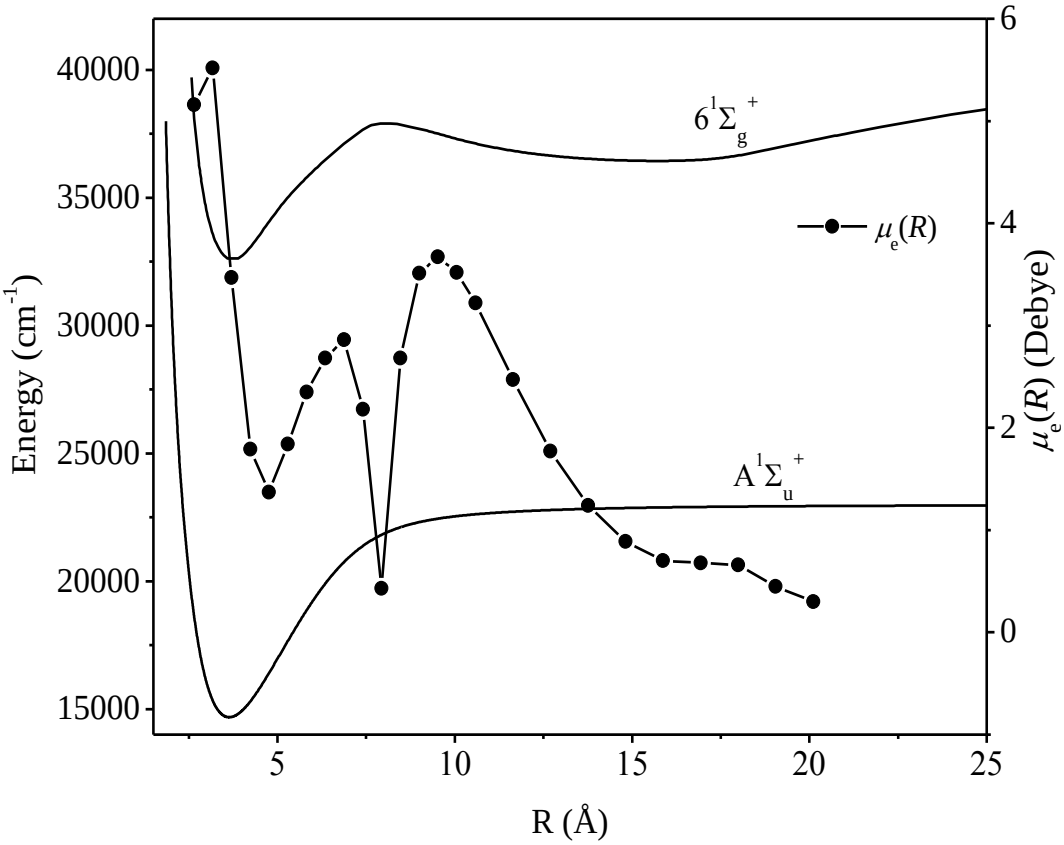

Figure 4.14 Potential curves for $6^1\Sigma_g^+$, $A^1\Sigma_u^+$ states of Na_2 and the *ab-initio* transition dipole moment curve between the states.

Table 4.2 Total lifetimes for the Na_2 molecular states (lifetimes in nanoseconds). v and J are vibrational and rotational quantum numbers. A, 3 ,4, 5, 6 are $A^1\Sigma_u^+$, $3^1\Sigma_g^+$, $4^1\Sigma_g^+$, $5^1\Sigma_g^+$ and $6^1\Sigma_g^+$ states respectively.

Total Lifetimes for the Na_2 Molecular States (lifetimes in nanoseconds)								
v	A(J=1)	A(J=20)	A(J=40)	A(J=60)	3(J=1)	4(J=1)	5(J=1)	6(J=1)
0	12.2023	12.2260	12.2949	12.4078	38.9804	12.7221	37.0186	141.9680
1	12.2274	12.2509	12.3190	12.4306	37.0126	12.9307	37.6302	137.5085
2	12.2505	12.2737	12.3410	12.4510	35.1479	13.1572	38.2283	134.5513
3	12.2723	12.2952	12.3616	12.4700	33.3690	13.3882	38.7832	132.5992
4	12.2927	12.3153	12.3808	12.4879	31.6653	13.6349	39.3209	131.4270
5	12.3121	12.3345	12.3992	12.5050	30.1563	13.8949	39.8850	130.9479
6	12.3307	12.3528	12.4170	12.5218	28.8431	14.1596	40.4451	130.9823
7	12.3488	12.3707	12.4343	12.5380	27.6557	14.4219	41.0045	131.4060
8	12.3660	12.3877	12.4506	12.5527	26.5681	14.6779	41.5669	132.1823
9	12.3819	12.4033	12.4653	12.5660	25.6053	14.9309	42.1700	133.2764
10	12.3966	12.4177	12.4788	12.5781	24.7796	15.1818	42.8189	134.5945
11	12.4104	12.4312	12.4913	12.5889	24.0333	15.4326	43.5071	136.0820
12	12.4232	12.4436	12.5027	12.5986	23.3701	15.6835	44.2431	137.6939
13	12.4349	12.4550	12.5130	12.6072	22.8165	15.9361	45.0349	139.3734
14	12.4455	12.4652	12.5223	12.6148	22.3519	16.1902	45.9163	141.1399
15	12.4550	12.4744	12.5306	12.6215	21.9870	16.4447	46.9386	142.9330
16	12.4637	12.4828	12.5380	12.6273	21.6848	16.7064	48.1168	144.6782
17	12.4715	12.4903	12.5445	12.6320	21.4447	17.0041	49.4067	146.3514
18	12.4785	12.4969	12.5499	12.6350	21.2898	17.3015	50.7630	147.9579
19	12.4842	12.5021	12.5535	12.6358	21.2295	17.7929	52.2207	149.4682
20	12.4877	12.5050	12.5548	12.6346	21.3179	18.1514	53.7673	150.8523
21	12.4891	12.5059	12.5546	12.6342	21.6192	18.8759	55.2861	152.0717
22	12.4899	12.5067	12.5557	12.6372	22.6605	19.2698	56.8502	153.1401
23	12.4930	12.5102	12.5604	12.6417	28.7041	19.6635	58.3674	154.0026
24	12.4992	12.5164	12.5653	12.6408	28.7751	19.9456	59.6806	154.6580
25	12.5034	12.5194	12.5641	12.6347	30.3007	20.3446	60.7370	155.1943
26	12.5010	12.5159	12.5590	12.6330	30.1681	20.8382	61.4559	156.0310
27	12.4973	12.5126	12.5581	12.6336	30.3246	21.2409	61.6364	156.3267

ν	A(J=1)	A(J=20)	A(J=40)	A(J=60)	3(J=1)	4(J=1)	5(J=1)	6(J=1)
28	12.4988	12.5143	12.5596	12.6449	30.5072	21.5913	61.1591	156.6336
29	12.4979	12.5125	12.5577	12.6520	30.8628	21.9668	59.9722	156.5051
30	12.4992	12.5138	12.5738	12.7820	31.2779	22.6606	58.1064	157.3199
31	12.4994	12.5196	12.6001	12.8694	31.5118	23.0657	55.7952	157.5757
32	12.5585	12.5753	12.7577	13.4948	31.8238	23.4875	53.2600	158.3060
33	12.5852	12.6443	12.8848	13.8639	32.0748	23.9653	50.7423	158.3899
34	12.9173	12.9297	13.6251	15.5725	32.3705	24.6175	48.4151	159.5128
35	13.0828	13.3063	13.9983	16.3736	32.6975	25.1171	46.3375	159.6054
36	14.2006	14.1558	15.8930	18.0911	32.9488	25.9061	44.4942	159.2477
37	14.7130	15.2488	16.4424	18.3668	33.2167	26.8213	42.7847	160.1761
38	16.6419	16.5057	18.0401	18.3317	33.5044	27.5540	41.2142	161.0946
39	17.2619	17.6379	18.0819	18.4616	33.8013	28.8284	39.7684	161.0299
40	17.8887	17.8788	18.0482	19.7109	34.0825	29.7598	38.4219	162.4380
41	17.8069	17.8106	18.1243	20.7825	34.3868	31.0437	37.2809	7260.7826
42	18.1078	18.0353	19.8880	21.1131	34.6629	32.4173	36.2845	6635.3561
43	18.6505	19.2118	20.2689	21.0024	34.9238	33.8914	35.3047	6162.7994
44	20.0181	19.8947	20.6069	21.6935	35.2220	35.9309	34.3057	161.8641
45	20.3973	20.3887	20.4666	23.1983	35.5318	38.0687	33.3102	5759.0497
46	20.3003	20.2645	21.7800	23.3614	35.8151	41.0067	32.2602	5411.2383
47	20.5955	21.0793	22.3115	23.3288	36.0633	44.6739	31.2776	5112.7693
48	21.7927	21.6421	22.6799	23.9779	36.3238	49.7003	30.3673	4878.3579
49	22.4416	22.3967	22.5170	25.5903	36.6072	57.7253	26.0374	4695.9503
50	22.2939	22.2146	23.9847	25.3379	36.9192	73.3256	26.6488	161.9446
51	22.7466	23.2645	24.5689	26.1452	37.2430	128.6917	26.0379	4747.4174
52	23.7526	23.6551	24.4977	26.7321	37.5478	236.1928	25.8492	4767.2097
53	24.1521	23.9954	24.6140	27.2465	37.8450	180.9730	28.4406	4859.4821
54	24.1259	23.8966	26.2404	27.0956	38.0982	154.4352	25.7555	4772.3928
55	25.2851	25.7179	26.3960	29.5914	38.3302	145.9349	25.6621	4490.7699
56	25.7484	25.7422	26.5855	29.4538	38.6209	139.2378	27.4228	4241.6564
57	25.5769	25.6222	27.5276	29.8101	38.9406	133.7432	25.5330	161.9578
58	26.1620	25.8334	28.0267	30.2441	39.2725	129.4439	25.3573	4171.8884
59	27.7152	27.5470	27.7849	31.1019	39.6082	124.7423	25.1081	4067.4188
60	27.4169	27.1914	29.2582	30.7967	39.9585	122.0096	26.3107	3877.0689
61					40.2685	118.9945	24.8135	3694.3537
62					40.5515	116.7988	24.5191	161.2291
63					40.8267	114.5727	25.0395	3599.1809
64					41.0757	112.5176	24.4053	3496.1963
65					41.3214	110.9407	24.1981	3344.7282
66					41.6280	109.3290	24.8860	3225.9623

v	A(J=1)	A(J=20)	A(J=40)	A(J=60)	3(J=1)	4(J=1)	5(J=1)	6(J=1)
67					41.9275	107.9013	25.3093	3121.2071
68					42.3113	106.5582	25.4509	161.5104
69					42.7607	105.4788	25.9315	3040.0209
70					43.1960	104.3608	26.4550	2922.1814
71					43.9787	103.5007	27.0151	2818.0071
72					44.6379	102.5429	27.6826	2767.9684
73					45.5074	101.7039	28.3194	2669.5704
74					47.1095	100.9643	29.0471	0.0000
75					47.8700	100.2059	30.3417	2592.7516
76					49.8506	99.6659	32.1699	2526.9592
77					51.2746	99.0588	33.5293	2454.1201
78					52.2982	98.6004	34.2814	2406.4322
79					53.6683	98.3437	35.4155	2334.7188
80					54.0830	98.0148	36.3385	161.3971
81					54.4540	97.8684	36.5941	2268.7331
82					54.9123	98.1194	37.3904	2225.0403
83					55.3750	97.9535	38.1032	2190.5556
84					56.8847	97.9892	38.9970	2121.4691
85					57.5804	98.0549	41.1742	163.0783
86					59.1594	97.8179	42.1196	2063.1686
87					59.7740	97.7127	42.8777	2051.3462
88					60.1900	97.4795	43.6314	2003.3197
89					60.5897	97.3104	44.2439	1952.4783
90					60.9719	97.1928	46.0870	1914.3877
91					62.6741	97.0928	46.7626	162.5436
92					63.5131	96.9369	48.7831	1883.4029
93					64.4841	96.8254	49.1558	1861.0980
94					64.8323	96.7187	50.6005	1824.4752
95					65.1131	96.5677	51.1422	1781.4633
96					66.4250	96.4756	53.7534	165.6643
97					67.0275	96.4130	54.3983	1752.2877
98					68.7154	96.3397	55.9776	1744.3612
99					69.0142	96.2571	56.3425	1714.0817
100					69.3402	96.2050	59.2267	1680.4624
101					70.2684	96.1946	59.7303	1653.4365
102					71.1547	96.1858	61.7595	165.2423
103					72.8354	96.1905	62.6249	1632.1230
104					73.1931	96.2312	64.2474	1624.8237
105					73.5737	96.2547	66.3884	1600.8139

v	A(J=1)	A(J=20)	A(J=40)	A(J=60)	3(J=1)	4(J=1)	5(J=1)	6(J=1)
106					74.0057	96.3230	67.0762	1569.3728
107					76.2345	96.4213	69.2621	168.9428
108					76.7400	96.4608	69.9889	1545.8752
109					77.3034	96.5675	72.8938	1535.4474
110					77.7430	96.7376	74.3400	1521.8264
111					78.9703	96.8582	74.6408	1504.2229
112					80.4211	96.9765	78.0739	169.2409
113					81.2424	97.1134	78.9594	1475.3552
114					81.4926	97.3043	80.3893	1448.4107
115					82.0841	97.4750	83.4157	1439.0054
116					84.1760	97.6182	84.1463	1419.1657
117					85.0127	97.8472	86.6125	1396.7509
118					85.3703	98.0395	89.1789	172.7025
119					85.6987	98.1934	89.6499	1361.1403
120					87.6568	98.3257	92.5462	1320.5015
121					88.7621	98.5862	95.5177	1288.1238
122					89.3178	98.7561	96.3736	1256.5119
123					89.6052	98.8658	98.9504	174.0626
124					90.5212	99.1889	102.6480	1208.2119
125					92.6360	99.3382	104.2778	1161.6079
126					93.0211	99.5538	106.0474	1108.3385
127					93.1938	99.7772	110.6180	1049.9152
128					93.3262	100.1313	113.3489	176.9896
129					95.1966	100.3647	114.7661	1022.7096
130					96.2103	100.5190	118.9443	960.8650
131					96.5270	101.0390	123.2902	925.4773
132					96.5034	101.2970	126.0827	877.5573
133					96.8426	101.5051	128.8396	826.6879
134					96.9037	101.7302	134.7724	179.2795
135					98.3580	102.3693	140.5733	800.9176
136					99.7622	102.6021	145.8405	759.8399
137					100.3121	102.8460	153.7619	730.5079
138					101.1338	103.5019	168.2069	702.3883
139					102.1386	103.7939	189.3523	182.0759
140					103.2150	103.9844	203.4716	675.6215
141					104.3537	104.1809	246.2637	653.5861
142					105.7413	104.9613	377.3992	651.4660
143					107.3225	105.0775	818.2497	633.2908
144					109.2583	105.6843	918.0842	185.1047

v	A(J=1)	A(J=20)	A(J=40)	A(J=60)	3(J=1)	4(J=1)	5(J=1)	6(J=1)
145						105.9816	993.0787	639.3041
146						106.1682	1018.5558	635.1595
147						106.4737	957.3343	629.7286
148						107.0788	841.6993	644.9417
149						107.1753	713.6792	634.9915
150						107.1476	595.7783	189.1442
151						107.9592	495.4425	642.6938
152						108.0427	418.0219	636.4711
153						108.3700	448.9550	628.4677
154						108.3151	1060.0080	626.3436
155						108.3302	1181.8450	194.1684
156						107.8977	1916.7279	627.6022
157						109.1413	2779.7196	622.9271
158						108.6370	3376.6144	626.4641
159						108.5389	3923.5171	627.6786
160						107.9765	4484.6672	202.4606
161						107.4578	4884.6860	622.1981
162						106.4307	8310.4190	638.4091
163						107.0307	6107.7220	630.2019
164						105.3656	4373.9803	636.6879
165						104.0846	3106.9120	217.1060
166						101.9167		643.0889
167						99.6840		641.0742
168						96.5995		662.3583
169						95.0901		666.0233
170						90.6320		253.6792
171						85.4822		666.7991
172						79.3168		686.6076
173						72.2726		700.7321
174						63.9597		486.0026
175						55.7693		472.7036
176						48.6481		630.4017
177						41.4608		615.4835
178						36.7100		550.3700
179						35.5109		544.5124
180						34.3229		567.1349
181						33.6724		573.2468
182						33.1814		581.4114
183						32.7769		599.7276

v	A(J=1)	A(J=20)	A(J=40)	A(J=60)	3(J=1)	4(J=1)	5(J=1)	6(J=1)
184						32.4316		600.3229
185						32.0975		605.1751
186						31.8107		630.8502
187						31.5992		643.1963
188						31.4526		649.2626
189						31.3386		665.4061
190						31.2366		669.9424
191						31.1400		673.3162
192						31.0526		684.3415
193						30.9858		685.0229
194						30.9564		689.5883
195						30.9997		701.5421
196						31.1576		697.2173
197						31.4688		693.9159
198						31.9297		703.0818
199						32.4401		702.4195
200						32.8199		700.6993
201						19512277.6147		707.3507
202						22071533.8417		703.8431
203						25045636.1969		699.7528
204						28515162.6589		705.5896
205						32583887.1288		703.9984
206						37383709.6257		700.2065
207						43081629.2878		704.1886
208						49890990.8918		701.6495
209						58117909.5590		696.0326
210						68025830.0954		698.2372
211						80183774.0743		698.6885
212						95171084.2190		694.0119
213						113820606.7591		691.0860
214						137593145.6282		690.6172
215						167759794.7555		689.1537
216						206744132.5052		684.4785
217						257550745.2188		682.8360
218						326734011.3514		683.1668
219						416858651.7035		676.4237
220								671.8490
221								674.1798
222								668.8067

v	A(J=1)	A(J=20)	A(J=40)	A(J=60)	3(J=1)	4(J=1)	5(J=1)	6(J=1)
223								654.1744
224								646.8118
225								630.7142
226								597.6914
227								531.5264
228								403.9381
229								300.6004
230								373.3167
231								501.2833
232								544.9681
233								513.9969
234								405.9128
235								424.2793
236								535.2372
237								555.6774
238								476.0284
239								441.3174
240								534.5140
241								541.9880
242								447.4208
243								458.8987
244								554.5716
245								510.0629
246								455.8248
247								550.6405
248								531.4995
249								462.9313
250								543.0459
251								514.6384
252								457.6617
253								549.5860
254								496.3859
255								499.2884
256								556.4033
257								479.0301
258								544.2793
259								505.8743
260								493.7176
261								536.0960

v	A(J=1)	A(J=20)	A(J=40)	A(J=60)	3(J=1)	4(J=1)	5(J=1)	6(J=1)
262								473.1899
263								543.0536
264								479.2211
265								538.4641
266								498.5447
267								530.6479
268								502.7340
269								515.5893
270								493.6890
271								503.7963
272								493.5821
273								513.6847
274								496.0942
275								529.8437
276								490.4047
277								531.7077
278								475.7307
279								512.2382
280								477.7299
281								492.0497
282								514.0090
283								485.7727
284								530.3177
285								489.9721
286								487.0482
287								502.4532
288								462.9736
289								492.8883
290								508.5154
291								490.6445
292								512.3371
293								510.6314
294								472.0371
295								474.0782
296								494.0025
297								494.3127
298								507.2134
299								546.1581
300								546.5790

v	A(J=1)	A(J=20)	A(J=40)	A(J=60)	3(J=1)	4(J=1)	5(J=1)	6(J=1)
301								514.1608
302								492.8729
303								504.8901
304								553.1082

4.6 Suggested Excitation Schemes

Double [45], triple [49] and quadruple [39] resonance excitation schemes can be used to measure the absolute magnitude of the transition dipole moments matrix elements by using the Autler-Townes effect. As demonstrated in reference [40] these measurements can be combined with calibrated intensity measurements for weaker transitions for broader internuclear range mapping of the transition dipole moment functions. In this section, we suggest an excitation scheme for Autler-Townes splitting based measurement of the absolute transition dipole moment function. Published in 2006 by E.H. Ahmed *et al*. [40] presented a new approach for measuring the transition dipole moment of molecular transitions by using the Autler-Townes splitting. To simulate these experiments one needs to know the lifetimes of the excited molecular states. The ion-pair states in Na_2 have very complicated μ vs. R behavior. Here we provide the preliminary calculations for mapping this behavior; trying to find the best candidates to use for the coupling laser transition, L_4, shown in Figure 4.15 for this purpose.

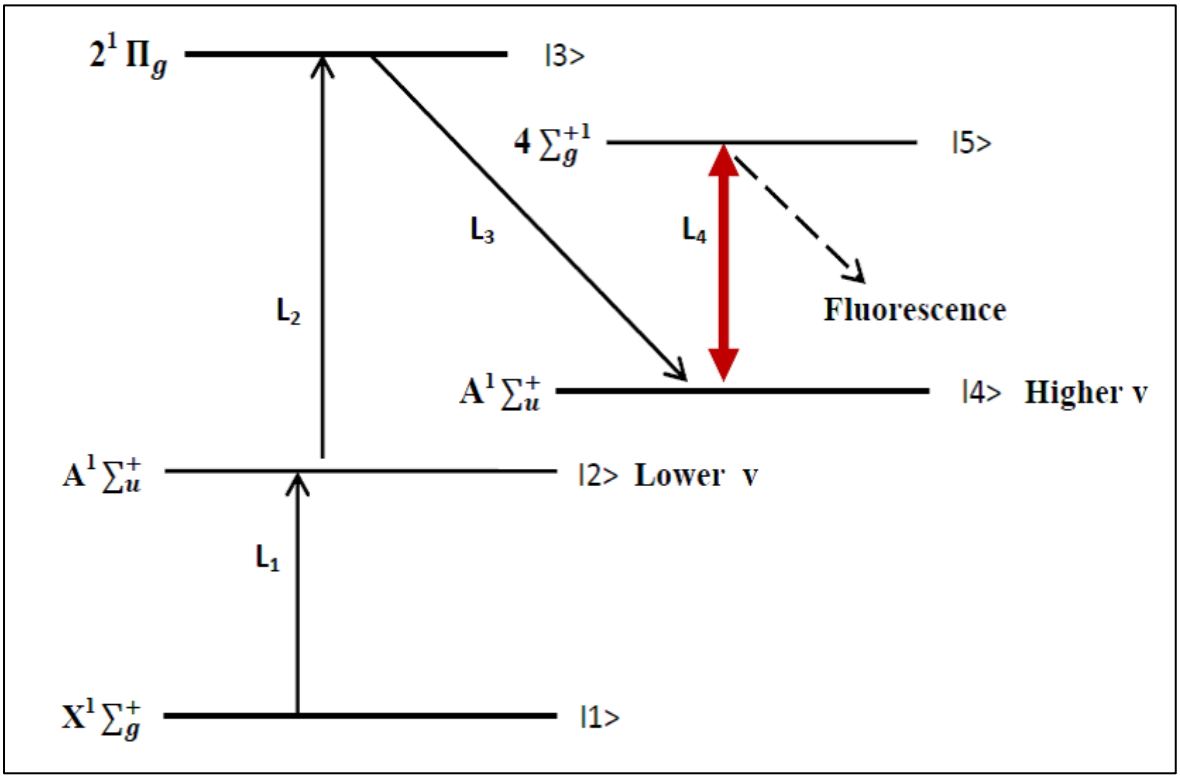

Figure 4.15 All-optical quadruple resonance technique sample excitation scheme. The goal is to find a set of transitions, which is in the range of available lasers, and also satisfies the conditions of higher FCF and a higher μ matrix element. Excitation schemes used for the all-optical quadruple resonance experiment [39]. L_4 is the coupling laser which couples levels |4> and |5> to the system. The Autler-Townes splitting caused by L_4 is observed in the fluorescence spectra by scanning the frequency of the probe laser L_3, while all other lasers are kept on resonance.

4.7 Conclusions

This work presents calculations of the transition their matrix elements between the $A^1\Sigma_u^+$ state and the ion-pair states $X^1\Sigma_g^+$, $3^1\Sigma_g^+$, $4^1\Sigma_g^+$, $5^1\Sigma_g^+$, $6^1\Sigma_g^+$ of the Na_2 molecule. In addition, lifetimes of these states have been calculated (Table 4.2). Transition dipole moment matrix elements maps for $A^1\Sigma_u^+ \leftarrow X^1\Sigma_g^+$ and $(3\text{-}6)^1\Sigma_g^+ \leftarrow A^1\Sigma_u^+$ transitions are as shown in Figure 4.7, Figure 4.8, Figure 4.9, Figure 4.10 and Figure 4.11, respectively. The lifetime plots for $A^1\Sigma_u^+$ and $(3\text{-}6)^1\Sigma_g^+$ states are as depicted in Figure 4.6 Both inner and outer wells of $6^1\Sigma_g^+$ electronic state are studied computationally and the wavefunctions are plotted. We have determined the inner-well behavior of the transition dipole moment matrix elements by carrying out OODR and Autler-Townes experiments for $(4\text{-}5)^1\Sigma_g^+ \leftarrow A^1\Sigma_u^+$ transitions and the results are listed in Chapter 3. An Optical-Optical Double Resonance excitation scheme is not enough to reach transitions of the outer well. Hence, one needs to carry out a quadruple resonance scheme to reach those levels. The calculated lifetimes and transition dipole moment matrix element plots in this work will be helpful in the design of double or quadruple resonance based Autler-Townes experiment. A possible quadruple resonance scheme to study the outer well behavior of TDMs is shown in Figure 4.15. The calculated lifetimes are listed in Table 4.2. Even if the transition dipole moment matrix elements do not facilitate Autler-Townes probing of the transition dipole moments for transitions from the outer well, the energy levels could be observed using quadruple resonance excitations.

References

[1] S. Magnier, Private communication.

[2] A. Sanli, B. Beser, J.R. Edwardson, S. Magnier, E.H. Ahmed, A. Marjatta Lyyra, Electronic transition dipole moment and radiative lifetime calculations of sodium dimer ion-pair states, The Journal of Chemical Physics 143 (2015) 104304.

[3] R.S. Mulliken, Physical Review 50 (1936) 1028.

[4] W.C. Stwalley, W.T. Zemke, S.C. Yang, Journal of Physical and Chemical Reference Data 20 (1991) 153-187.

[5] W.C. Stwalley, W.T. Zemke, Journal of Physical and Chemical Reference Data 22 (1993) 87-112.

[6] S. Yu, K. Dressler, Journal of Chemical Physics 101 (1994) 7692-7706.

[7] L. Wolniewicz, K. Dressler, Journal of Chemical Physics 82 (1985) 3292-3299.

[8] A. Spielfiedel, Journal of Molecular Spectroscopy 217 (2003) 162-172.

[9] I. Schmidtmink, W. Muller, W. Meyer, Chemical Physics 92 (1985) 263-285.

[10] S. Magnier, P. Millie, O. Dulieu, F. Masnou-Seeuws, Journal of Chemical Physics 98 (1993) 7113-7125.

[11] K.K. Docken, J. Hinze, Journal of Chemical Physics 57 (1972) 4928-&.

[12] C.R. Vidal, W.C. Stwalley, Journal of Chemical Physics 77 (1982) 883-898.

[13] W.C. Stwalley, Journal of Chemical Physics 63 (1975) 3062-3080.

[14] X.J. Wang, J. Magnes, A.M. Lyyra, A.J. Ross, F. Martin, P.M. Dove, R.J. Le Roy, Journal of Chemical Physics 117 (2002) 9339-9346.

[15] R.C. Ekey, E.F. McCormack, Journal of Physics B-Atomic Molecular and Optical Physics 38 (2005) 1029-1035.

[16] C.W. Zucker, E.E. Eyler, Journal of Chemical Physics 85 (1986) 7180-7183.

[17] W. Jastrzebski, A. Pashov, P. Kowalczyk, Journal of Chemical Physics 114 (2001) 10725-10727.

[18] A. Pashov, W. Jastrzebski, P. Kowalczyk, Journal of Chemical Physics 113 (2000) 6624-6628.

[19] S. Antonova, Ph.D. thesis, Temple University, 2000.

[20] S. Antonova, G. Lazarov, K. Urbanski, A.M. Lyyra, L. Li, G.H. Jeung, W.C. Stwalley, Journal of Chemical Physics 112 (2000) 7080-7088.

[21] C.C. Tsai, J.T. Bahns, T.J. Whang, H. Wang, W.C. Stwalley, A.M. Lyyra, Physical Review Letters 71 (1993) 1152-1155.

[22] C.C. Tsai, T.J. Whang, J.T. Bahns, W.C. Stwalley, Journal of Chemical Physics 99 (1993) 8480-8488.

[23] C.C. Tsai, J.T. Bahns, H. Wang, T.J. Whang, W.C. Stwalley, Journal of Chemical Physics 101 (1994) 25-30.

[24] C.C. Tsai, J.T. Bahns, W.C. Stwalley, Journal of Chemical Physics 100 (1994) 768-774.

[25] C.C. Tsai, J.T. Bahns, W.C. Stwalley, Journal of Molecular Spectroscopy 167 (1994) 429-436.

[26] T. Laue, P. Pellegrini, O. Dulieu, C. Samuelis, H. Knockel, F. Masnou-Seeuws, E. Tiemann, European Physical Journal D 26 (2003) 173-185.

[27] E.B.W. Lerch, X.C. Dai, S. Gilb, E.A. Torres, S.R. Leone, Journal of Chemical Physics 124 (2006).

[28] E.A. Torres, E.-B.W. Lerch, X. Dai, S. Gilb, S.R. Leone, Journal of Chemical Physics 126 (2007).

[29] X. Dai, S.R. Leone, Journal of Chemical Physics 127 (2007).

[30] E.-B.W. Lerch, X. Dai, E.A. Torres, J.B. Ballard, H.U. Stauffer, S.R. Leone, Journal of Physics B-Atomic Molecular and Optical Physics 41 (2008).

[31] O. Babaky, K. Hussein, Canadian Journal of Physics 67 (1989) 912-918.

[32] V.S. Ivanov, V.B. Sovkov, L. Li, The Journal of Chemical Physics 118 (2003) 8242-8247.

[33] P. Qi, J. Bai, E. Ahmed, A.M. Lyyra, S. Kotochigova, A.J. Ross, C. Effantin, P. Zalicki, J. Vigue, G. Chawla, R.W. Field, T.J. Whang, W.C. Stwalley, H. Knoeckel, E. Tiemann, J. Shang, L. Li, T. Bergeman, Journal of Chemical Physics 127 (2007).

[34] P. Kusch, M.M. Hessel, Journal of Chemical Physics 68 (1978) 2591-2606.

[35] E. Tiemann, Zeitschrift Fur Physik D-Atoms Molecules and Clusters 5 (1987) 77-82.

[36] S. Magnier, M. Aubertfrecon, O. Bouty, F. Masnou-Seeuws, P. Millie, V.N. Ostrovsky, Journal of Physics B-Atomic Molecular and Optical Physics 27 (1994) 1723-1741.

[37] S. Magnier, M. Aubert-Frecon, C. Le Sech, Journal of Physical Chemistry A 105 (2001) 11069-11072.

[38] H. Hotop, W.C. Lineberger, Journal of Physical and Chemical Reference Data 14 (1985) 731-750.

[39] E.H. Ahmed, P. Qi, A.M. Lyyra, Physical Review A 79 (2009).

[40] E. Ahmed, A. Hansson, P. Qi, T. Kirova, A. Lazoudis, S. Kotochigova, A.M. Lyyra, L. Li, J. Qi, S. Magnier, Journal of Chemical Physics 124 (2006) 084308

[41] O. Salihoglu, P. Qi, E.H. Ahmed, S. Kotochigova, S. Magnier, A.M. Lyyra, Journal of Chemical Physics 129 (2008).

[42] S.J. Sweeney, E.H. Ahmed, P. Qi, T. Kirova, A.M. Lyyra, J. Huennekens, Journal of Chemical Physics 129 (2008).

[43] J.Y. Seto, R.J. Le Roy, J. Verges, C. Amiot, Journal of Chemical Physics 113 (2000) 3067-3076.

[44] J.B. Qi, G. Lazarov, X.J. Wang, L. Li, L.M. Narducci, A.M. Lyyra, F.C. Spano, Physical Review Letters 83 (1999) 288-291.

[45] J. Qi, F.C. Spano, T. Kirova, A. Lazoudis, J. Magnes, L. Li, L.M. Narducci, R.W. Field, A.M. Lyyra, Physical Review Letters 88 (2002) 173003.

[46] E.H. Ahmed, P. Qi, B. Beser, J. Bai, R.W. Field, J.P. Huennekens, A.M. Lyyra, Physical Review A 77 (2008).

[47] R.J. Leroy, University of Waterloo Chemical Physics Research CP-663, 2007.

[48] G. Baumgartner, H. Kornmeier, W. Preuss, Chemical Physics Letters 107 (1984) 13-21.

[49] A.M. Lyyra, H. Wang, T.J. Whang, W.C. Stwalley, L. Li, Physical Review Letters 66 (1991) 2724-2727.

CHAPTER 5

LIFETIME AND TRANSITION DIPOLE MOMENT CALCULATIONS OF LITHIUM DIMER ION-PAIR ELECTRONIC STATES

5.1 Introduction

Being the smallest homonuclear diatomic molecule after H_2, there are many experimental and theoretical studies of the lithium dimer since it is a relatively simpler system compared to other alkali dimer molecules. In this work we focused on the $^7Li_2$ molecule. Figure 5.1 shows the potential energy curves of the lithium dimer molecular electronic states. As can be seen from the figure, these states exhibit double wells and shoulders due to the interaction with the Li^+ Li^- ion-pair configuration. The double well behavior is predominantly observed for higher lying electronic states states of $^1\Sigma_g^+$ symmetry at larger internuclear distance. The ion-pair character of these potential energy curves makes their lifetimes also interesting because of the unusual behavior of their transition dipole moments which exhibit rapid changes in regions of internuclear distance corresponding to potential energy curve shoulders and double wells. The changing wavefunction amplitudes and wavelength around the shelf regions as seen Figure 5.2 in turn cause the overlap integrals to differ significantly compared to those involving lower lying excited state vibrational levels.

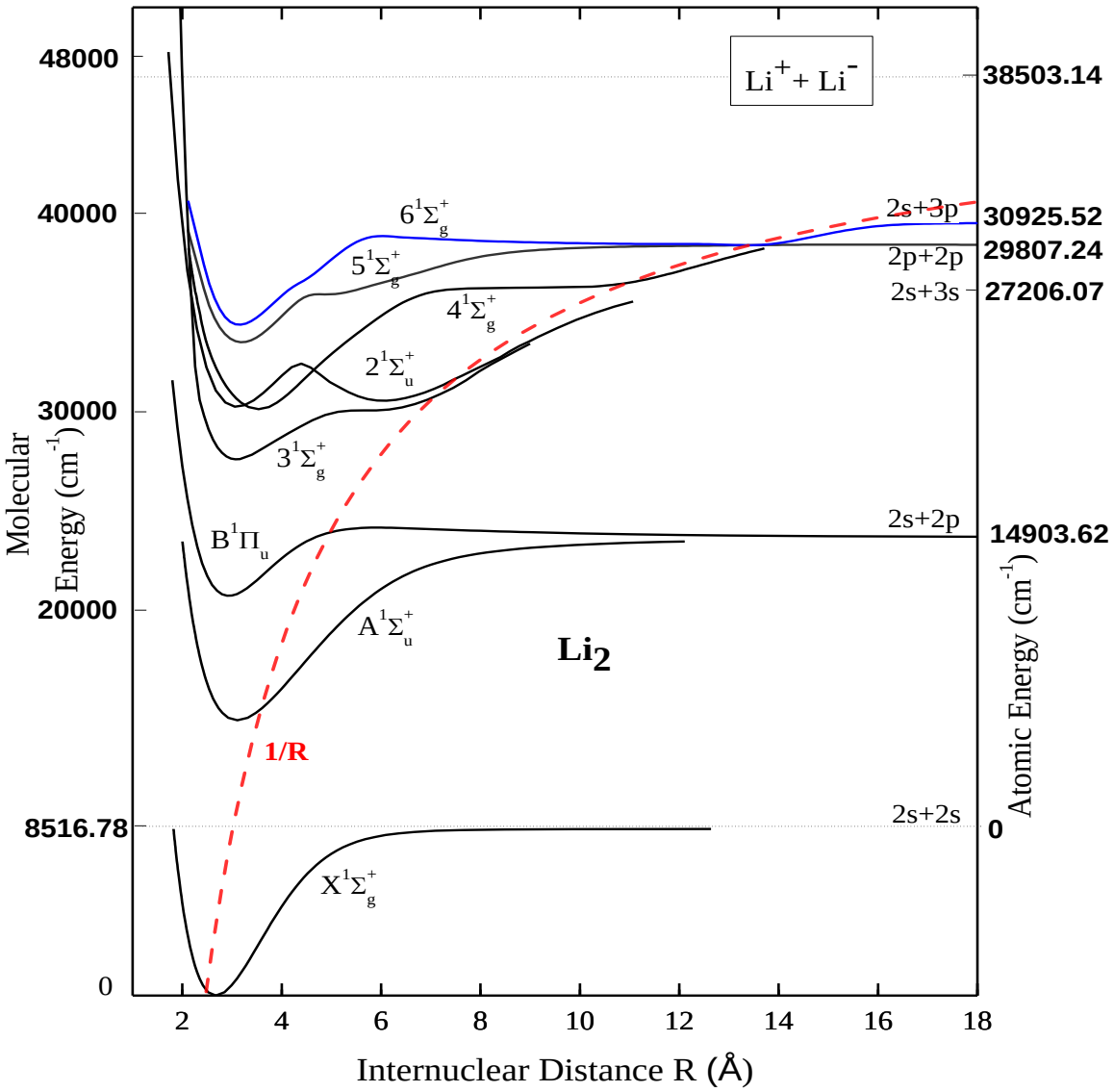

Figure 5.1 Potential energy curves of the lithium dimer $^{7}Li_2$, including some ion-pair electronic states. The red dashed curve is the ion-pair curve.

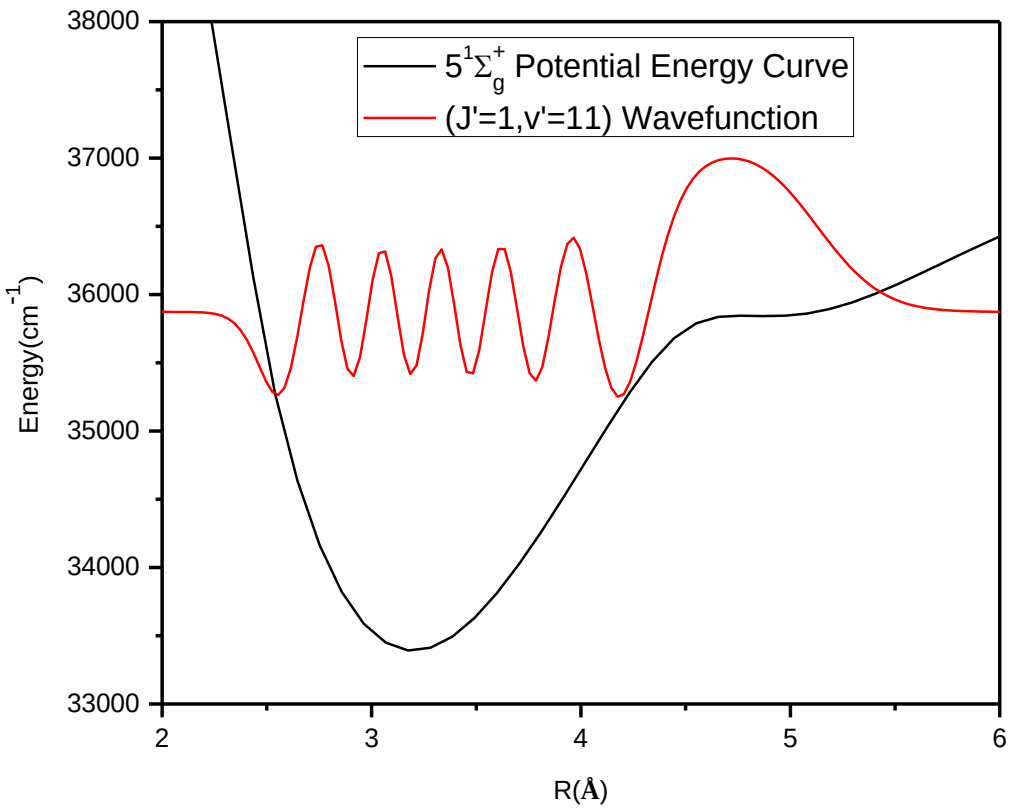

Figure 5.2 $^{7}Li_2$ $5\,^{1}\Sigma_g^{+}$ (v = 25, J=1) vibrational wavefunction for a level near the shelf region.

Besides the multiple wells and shoulders, the lithium dimer is particularly exciting for analysis because in contrast to the sodium dimer, there are bound to continuum transitions for higher lying states. In this work, we present a computational study of total lifetimes (including bound-bound and bound-continuum transitions) and transition dipole moment matrix elements for the lithium dimer ion-pair states. We have calculated the

total lifetimes (Table 5.1), τ, of these ion-pair states and we compare them with experimental results from literature when available [1-6].

5.2 Potential Energy Curves (PECs) and Transition Dipole Moment Functions (TDM) for Li_2 Ion-Pair States

For the Li_2 ground state, we used the $X^1\Sigma_g^+$, potential energy curve from Ref.[7] and the $A^1\Sigma_u^+$ potential from Ref.[4]. The Li_2 $E(3)^1\Sigma_g^+$ ion-pair state was first studied by Bernheim [8-10]. Trying to construct the potential energy curve using the RKR method failed around the shoulder of the $E(3)^1\Sigma_g^+$ state. Since the RKR method cannot be applied to the potentials with double minima or shoulders. Because of this, the inverted perturbation technique (IPA) was used by Bernheim to construct the potential energy curve. In the IPA method, the effect of the nonadiabatic contributions to the potential was not precisely known and suggested as a future work in Bernheim's paper [10]. Later, W. Jastrzebski *et al.* [3] reanalyzed the $E(3)^1\Sigma_g^+$ shoulder region with an improved IPA method which removed the unphysical oscillations in the shoulder region. W. Jastrzebski *et al.* used fewer parameters around the shelf region and used a cubic spline method which they argue is more flexible than the Legendre polynomial method used in Ref.[10]. Jastrzebski's study of the $E(3)^1\Sigma_g^+$ PEC [3] concludes that the nonadiabatic contributions to the $E(3)^1\Sigma_g^+$ state are as small as $0.1cm^{-1}$. We used W. Jastrzebski's $E(3)^1\Sigma_g^+$ PEC in our calculations since it was smoother than the PEC given in Ref. [10] and extended to longer internuclear distance.

The $^7Li_2$ $F(4)^1\Sigma_g^+$ state has a shelf region due to the interaction with the ion-pair curve. We used the RKR curve from Ref. [11] for our calculations. The $F(4)^1\Sigma_g^+$ state was first studied by Bernheim [8] by OODR technique and vibrational levels up to $v = 30$ were detected. Antonova *et al.* [11] used the same OODR spectroscopy method and observed levels up to $(v = 33)$. Then these authors used the more sensitive ionization technique in an attempt to observe higher levels. However none were observed. This was due to the fact that the $F(4)^1\Sigma_g^+$ state predissociated via the $E(3)^1\Sigma_g^+$ continuum to the 2s+3s atomic limit which is about 2600cm^{-1} below the 2p+2p atomic limit [8, 11].

The Li_2 $5^1\Sigma_g^+$ and $6^1\Sigma_g^+$ states were both first studied by Bernheim *et al*. experimentally through OODR spectroscopy as referred to in Refs. [2, 12]. Bernheim's work covers the low vibrational values $(v < 25)$ for these states and does not include the shelf and second minimum regions. Song *et al.* [12] carried out an *ab initio* calculation for both states which cover the full range of internuclear distance. According to Song *et al*., the $^7Li_2$ $5^1\Sigma_g^+$ and $6^1\Sigma_g^+$ states approach the 2p+2p and 2s+3p atomic limits, respectively. We used Sylvie Magnier's *ab initio* curves for the $5^1\Sigma_g^+$ and $6^1\Sigma_g^+$ states because Magnier's curves [13] are smoother and are defined better for outer wells close to the dissociation limits.

Both BCONT and LEVEL programs require the input of transition dipole moment functions for calculation of lifetimes. The transition dipole moment functions [13] used in LEVEL 8.0 and BCONT programs to calculate the lifetimes are plotted in Figure 5.3.

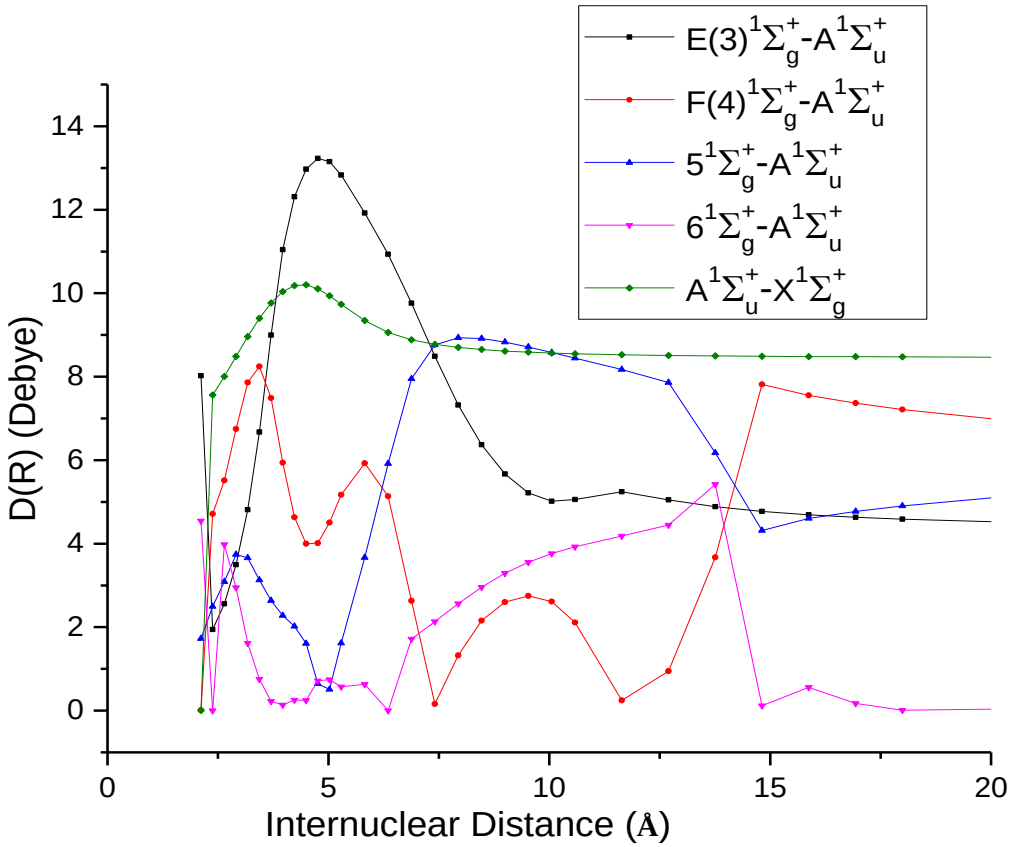

Figure 5.3 The transition dipole moment functions, D(R), of $^7Li_2$ ion-pair transitions [13].

5.3 Results and Discussion

As indicated in earlier chapters, one common way of obtaining molecular transition dipole moment matrix elements, Franck-Condon factors, and Einstein coefficients is by solving the radial Schrodinger equation numerically. LEVEL 8.0, a computational tool developed by Robert Le Roy [5], is used also here to calculate the bound-bound Einstein coefficients. Determining all Einstein coefficients leads to the knowledge of lifetimes. The problem with lithium dimer electronic states is that the electronic transitions between

certain states include significant bound-continuum contributions. LEVEL 8.0 can only handle bound-bound transitions. Bound-continuum transitions calculated by LEVEL 8.0 results in unphysical values for the transition probabilities. Therefore, the decay rates for bound-to-continuum transitions are calculated using the BCONT program [14]. The transitions corresponding to inner wells and lower lying vibrational levels do not have significant bound-continuum contributions so these transitions are calculated by LEVEL 8.0. For the bound-continuum high vibrational level transitions, we have combined the Einstein coefficients calculated by LEVEL 8.0 and BCONT to obtain an accurate physical lifetime behavior.

As can be seen in Figure 5.1, the $A^1\Sigma_u^+ \rightarrow X^1\Sigma_g^+$ transitions are bound-bound transitions only up to $v = 25$ of the $A^1\Sigma_u^+$ state after which the bound-continuum contribution becomes significant. Figure 5.4 shows that the Einstein coefficients contribution calculated by BCONT after $v = 25$ becomes significant and the brings the total lifetime curve down. The total lifetime values of $A^1\Sigma_u^+$ after $v = 25$ decrease slowly with increasing v.

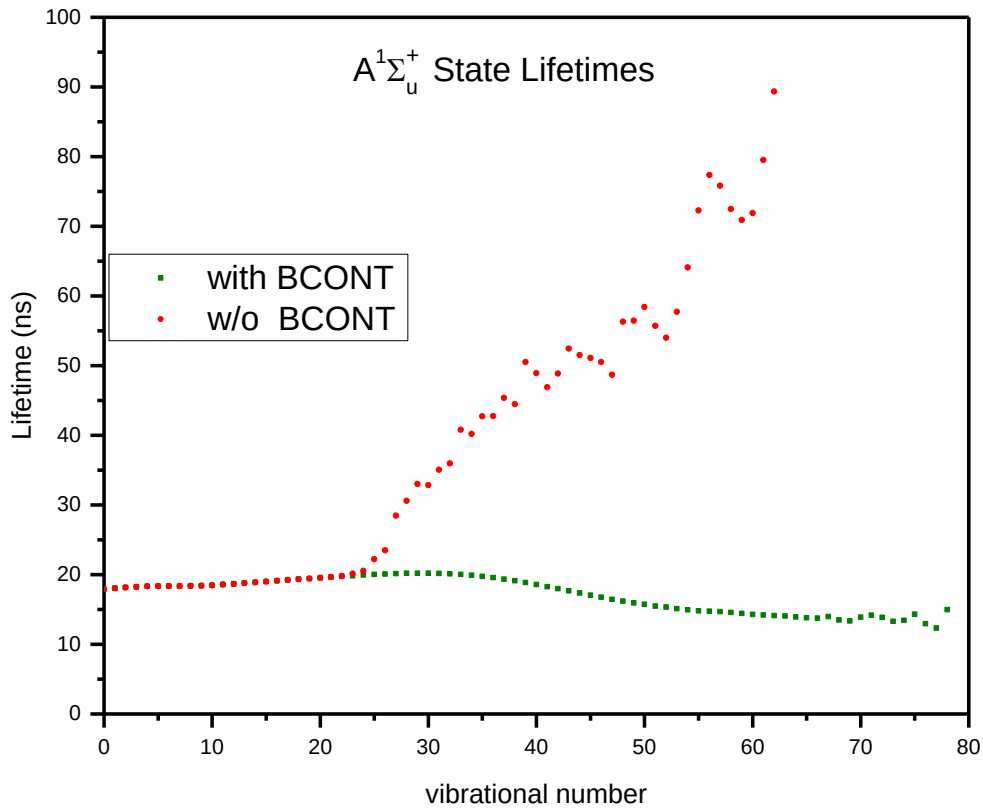

Figure 5.4 The $A^1\Sigma_u^+$ state lifetimes calculated with and without the bound- free contribution obtained using the BCONT program for $^7Li_2$.

The $E(3)^1\Sigma_g^+$ state has a second shallow well between 5.39-6.16Å. The effect of the Coulombic $1/R$ interaction on the potential is dominant in this region. The lifetime values experience a step increase at $v' = 13$ (Figure 5.5). The rotational constants right drops %30 as v' increases beyond 13 Figure 5.5 shows that $3^1\Sigma_g^+ \rightarrow A^1\Sigma_u^+$ transitions have bound-to-continuum components for transitions corresponding to larger internuclear distances. For the vibrational levels $v' > 37$ of the $3^1\Sigma_g^+$, the bound-unbound Einstein coefficients become significant and as shown in Figure 5.5. The lifetime values

calculated with inclusion of BCONT contributions are lower than those calculated with LEVEL neglecting the bound-continuum contributions.

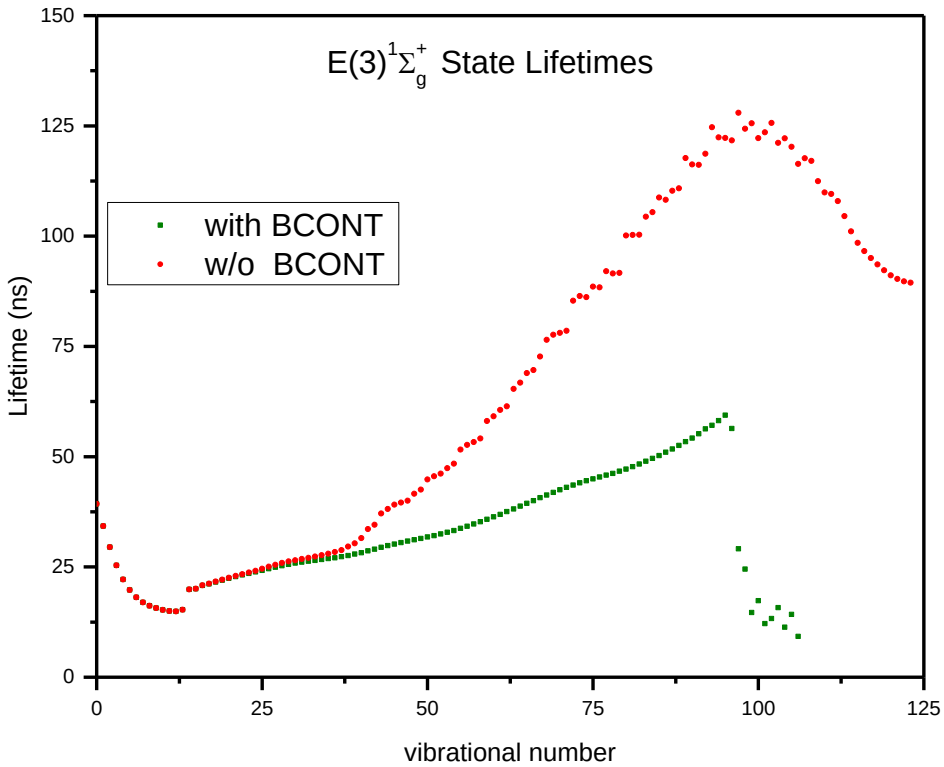

Figure 5.5 The $^7Li_2$ E(3)$^1\Sigma_g^+$ state lifetimes calculated with and without bound-free contributions obtained using the BCONT program.

The lifetimes of F(4)$^1\Sigma_g^+$ state show a step increase around vibrational number $v' = 39$. This is due to large shelf region of the F(4)$^1\Sigma_g^+$ state. Here the overlap integral of upper and lower states changes suddenly as v' changes resulting in a jump in the lifetime value. As it can be seen from Figure 5.6, the lifetime contribution due to bound-unbound transitions for the inner curve $v' < 39$ is not significant. For the outer well of

$F(4)^1\Sigma_g^+$ state, on the other hand, the gap between the total lifetimes (green curve) and the lifetimes calculated without including bound-continuum transitions (red curve) increases due to the increasing contribution of bound-to-continuum transitions to the total lifetime.

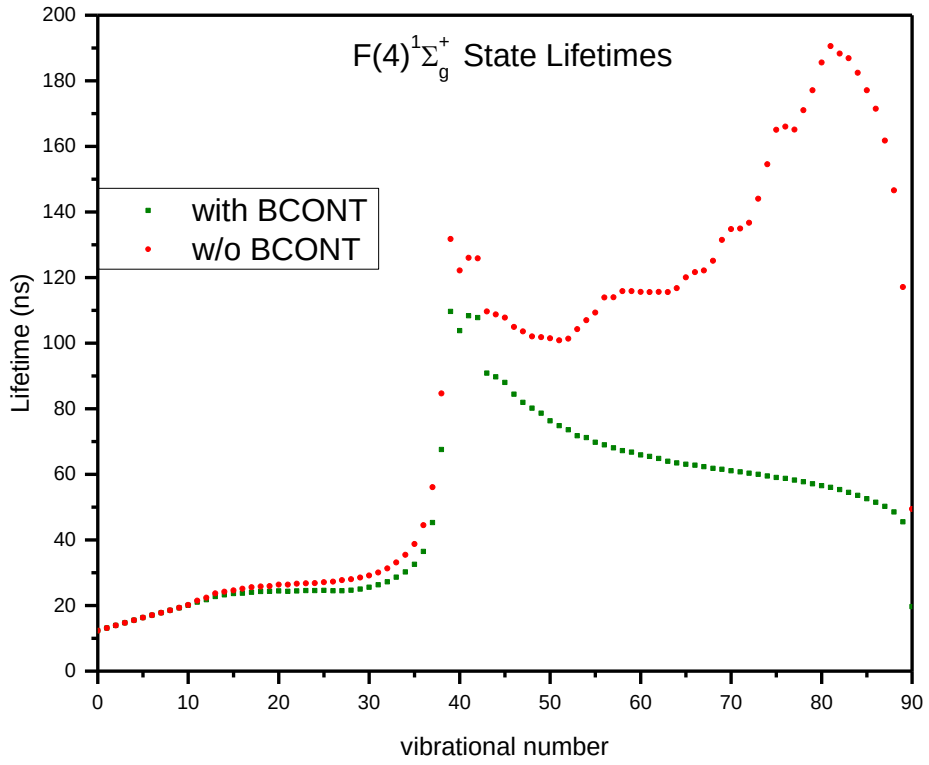

Figure 5.6 The $^7Li_2$ $F(4)^1\Sigma_g^+$ state lifetimes calculated with and without bound-free contributions obtained using the BCONT program.

The $5^1\Sigma_g^+$ state has a very shallow second well around vibrational level $v' = 12$. In Figure 5.7, it can be seen that the total lifetime is dominated by bound-bound transitions up to $v' = 12$. For $12 < v' < 30$, the bound-unbound contributions from the BCONT calculation are significant and shift the total lifetime curve down. For $v' > 30$, bound-unbound transitions again become insignificant and the two calculations agree.

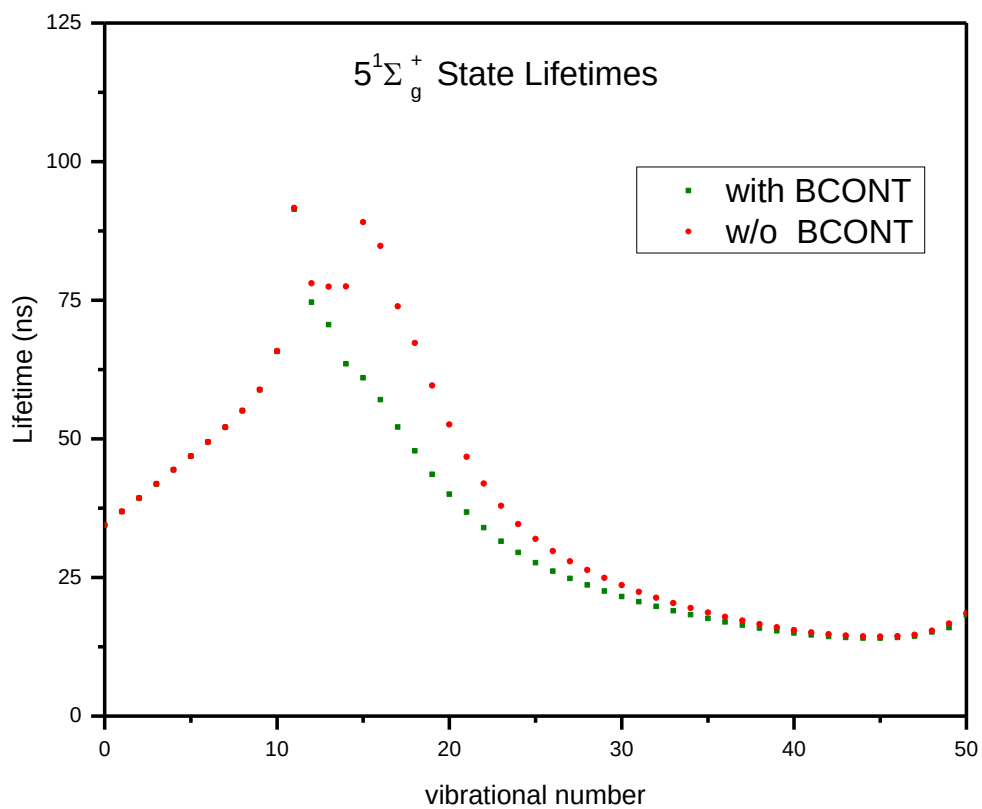

Figure 5.7 The $^7Li_2$ $5^1\Sigma_g^+$ state lifetimes calculated with and without bound- free contributions obtained using the BCONT program.

The theoretical $6^1\Sigma_g^+$ potential energy curve we use was calculated by Sylvie Magnier [13] and it has three potential minima which is quite unusual. The last minimum of the theoretical $6^1\Sigma_g^+$ potential occurs around 13Å. The BCONT program currently cannot handle a potential curve with three minima and we are currently working with Prof. Le Roy to address this issue.

The calculated total lifetime values for the ion-pair states of lithium dimer via LEVEL and BCONT programs are listed on Table 5.1. The transitions corresponding to the lower vibrational numbers are calculated by LEVEL whereas the higher vibrational numbers are calculated by BCONT.

Table 5.1 Total lifetimes for the $^7Li_2$ molecular states (lifetimes in nanoseconds). v is the vibrational quantum number. The calculations are carried out for the rotational number J=1.

Total Lifetimes for the Li_2 Molecular States (lifetimes in nanoseconds)					
v	$A^1\Sigma_u^+$	$E(3)^1\Sigma_g^+$	$F(4)^1\Sigma_g^+$	$5^1\Sigma_g^+$	$6^1\Sigma_g^+$
0	17.9117	39.2792	12.3350	34.4581	109.9584
1	18.0299	34.2441	13.1211	36.8950	98.0293
2	18.1412	29.5096	13.9316	39.3055	90.3364
3	18.2370	25.3688	14.7180	41.8644	85.1926
4	18.3101	22.1379	15.5086	44.4090	83.3262
5	18.3546	19.7584	16.2800	46.8868	84.4236
6	18.3657	18.1013	17.0417	49.4338	87.5683
7	18.3643	16.9787	17.7812	52.0977	91.1569
8	18.3749	16.2058	18.5339	55.0724	93.1837
9	18.4102	15.6640	19.3358	58.8795	91.6531
10	18.4793	15.2681	20.1741	65.8243	88.2432
11	18.5693	15.0038	21.4991	91.6678	85.7916
12	18.6746	14.9118	22.3622	78.0587	84.7568
13	18.7818	15.2842	23.7037	77.4407	86.2215
14	18.8902	19.9175	24.2088	77.4810	86.0888
15	19.0016	20.0750	24.6166	89.0893	91.0430
16	19.1148	20.8461	25.1093	84.8032	100.0754
17	19.2267	21.2008	25.5933	73.9164	99.7282
18	19.3342	21.6787	25.7698	67.3006	97.7449
19	19.4369	22.1241	25.9078	59.6389	97.5472
20	19.5384	22.5630	26.3690	52.6079	--
21	19.6592	22.9782	26.3628	46.7772	92.0603
22	19.7952	23.3616	26.6271	41.9534	47.1552
23	20.1517	23.7397	26.7495	37.9111	46.6771
24	20.5314	24.1391	26.7994	34.6393	49.8789
25	22.2065	24.5830	27.1268	31.9653	51.9719
26	23.5056	25.0466	27.2498	29.7494	54.1974
27	28.4702	25.4939	27.7001	27.9244	56.9314
28	30.5872	25.8959	28.0117	26.3548	60.2672
29	33.0090	26.2350	28.5377	24.9176	65.1124
30	32.8467	26.5251	29.1714	23.6088	92.6410

v	$A^1\Sigma_u^+$	$E(3)^1\Sigma_g^+$	$F(4)^1\Sigma_g^+$	$5^1\Sigma_g^+$	$6^1\Sigma_g^+$
31	35.0700	26.7933	30.0346	22.4238	72.6733
32	35.9598	27.0628	31.2972	21.3257	82.8523
33	40.7918	27.3512	33.0978	20.3716	92.6634
34	40.2101	27.6522	35.4570	19.4935	103.3279
35	42.7253	27.9966	38.7246	18.6670	121.3605
36	42.7556	28.3817	44.5024	17.9086	136.6780
37	45.3714	28.8147	56.0681	17.2152	97.4100
38	44.4725	29.6121	84.6706	16.6004	142.6975
39	50.5145	30.3410	131.7471	16.0237	158.5245
40	48.9298	31.5247	122.1834	15.5298	173.0099
41	46.9111	33.5751	125.9984	15.1077	198.8137
42	48.8660	34.5655	125.8794	14.7711	232.6331
43	52.4511	37.1131	109.6629	14.5237	144.7067
44	51.5130	38.1398	108.7730	14.3768	139.4032
45	51.1213	39.1257	107.8118	14.3412	262.9468
46	50.5016	39.5703	104.9443	14.4049	266.2999
47	48.6937	40.0277	103.5541	14.6494	273.1139
48	56.3140	41.5854	102.0681	15.4095	255.3443
49	56.4457	42.5218	101.8084	16.7009	262.5900
50	58.4152	44.8269	101.4665	18.5474	295.1729
51	55.7068	45.5728	100.8476		310.2723
52	54.0115	46.1554	101.3710		324.2372
53	57.7145	47.3656	104.2897		326.5158
54	64.0778	48.4246	106.9988		345.1753
55	72.2703	51.6181	109.3240		360.0658
56	77.3495	52.6751	113.9210		372.5047
57	75.8209	53.3266	113.9578		396.7436
58	72.4827	54.1074	115.8646		399.7465
59	70.9185	58.0761	115.8656		431.0772
60	71.8905	59.1669	115.5989		431.6276
61	79.5093	60.5845	115.5817		444.8876
62	89.3356	61.4224	115.6379		469.8345
63	108.7990	65.3562	115.5752		474.5302
64		66.7547	116.7665		502.9642
65		68.9355	120.0521		526.6458
66		69.6404	121.6465		536.0330
67		72.7066	122.1817		563.0725
68		76.4735	125.1369		599.8636
69		77.6320	131.4917		627.6997
70		78.0813	134.7876		692.8164

v	$A^1\Sigma_u^+$	$E(3)^1\Sigma_g^+$	$F(4)^1\Sigma_g^+$	$5^1\Sigma_g^+$	$6^1\Sigma_g^+$
71		78.5404	134.9543		817.9635
72		85.3383	136.6973		1131.8571
73		86.4414	144.0505		2107.3195
74		86.1647	154.5219		4349.3120
75		88.5579	165.0793		5323.5878
76		88.3694	165.9964		6301.1327
77		92.0513	165.1052		7137.2029
78		91.5445	171.0190		7864.4712
79		91.6674	177.0934		8496.2196
80		100.1439	185.5441		9040.5859
81		100.2561	190.5563		9514.5284
82		100.3086	188.3069		9940.8406
83		104.3877	186.8835		10337.7278
84		105.4170	182.4217		10713.9312
85		108.7590	177.0920		11076.4485
86		108.2330	171.4814		11438.2604
87		110.3046	161.7755		11817.2881
88		110.8548	146.5907		12204.5354
89		117.6823	117.0953		12579.9109
90		116.2588	49.4524		12948.1629
91		116.1462			13306.3267
92		118.6810			13658.3851
93		124.7009			14005.5491
94		122.3755			14339.5389
95		122.2750			14663.2150
96		121.6930			14979.2842
97		127.9817			15277.6063
98		124.3279			15579.1697
99		125.5797			15862.8895
100		122.2007			16135.9972
101		123.5328			16432.3992
102		125.6567			16691.4697
103		121.1524			16980.1322
104		122.1654			17248.4989
105		120.2629			17506.4022
106		116.3661			17805.8552
107		117.6632			18051.5857
108		117.0531			18357.1657
109		112.4365			18606.8862
110		109.8816			18880.5889

v	$A^1\Sigma_u^+$	$E(3)^1\Sigma_g^+$	$F(4)^1\Sigma_g^+$	$5^1\Sigma_g^+$	$6^1\Sigma_g^+$
111		109.5499			19154.4996
112		107.9510			19396.3072
113		104.5369			19699.6629
114		101.0688			19927.5935
115		98.4895			20233.6763
116		96.6152			20462.0286
117		95.0351			20737.8371
118		93.5677			20979.7411
119		92.2375			21218.4192
120		91.1261			21487.2092
121		90.2919			21700.2953
122		89.7422			21993.0522
123		89.4468			22194.4865
124					22490.6589
125					22689.5059
126					22964.9717
127					23169.3467
128					23411.4837
129					23630.6271
130					23841.6868
131					24084.2920
132					24275.1509
133					24536.1540
134					24717.1969
135					24989.1843
136					25167.0982
137					25436.3775
138					25614.1270
139					25868.0822
140					26046.9596
141					26278.2127
142					26459.4616
143					26667.1675
144					26852.3191
145					27040.8140
146					27231.2227
147					27407.5004
148					27603.7152
149					27775.0111
150					27976.3828

v	$A^1\Sigma_u^+$	$E(3)^1\Sigma_g^+$	$F(4)^1\Sigma_g^+$	$5^1\Sigma_g^+$	$6^1\Sigma_g^+$
151					28148.4948
152					28353.3085
153					28529.9412
154					28735.9611
155					28918.7844
156					29123.5873
157					29312.5224
158					29513.9409
159					29707.7783
160					29904.1146
161					30104.1474
162					30295.5854
163					30495.1074
164					30680.8126
165					30880.3374
166					31060.0014
167					31254.7391
168					31414.5499
169					31560.5716
170					31552.9308
171					31100.5510

References

[1] S. Kasahara, P. Kowalczyk, M.H. Kabir, M. Baba, H. Katô, The Journal of Chemical Physics 113 (2000) 6227-6234.

[2] N. Bouloufa, P. Cacciani, R. Vetter, A. Yiannopoulou, F. Martin, A.J. Ross, The Journal of Chemical Physics 114 (2001) 8445-8458.

[3] W. Jastrzębski, A. Pashov, P. Kowalczyk, The Journal of Chemical Physics 114 (2001) 10725-10727.

[4] K. Urbanski, S. Antonova, A. Yiannopoulou, A.M. Lyyra, W.C. Stwalley, J. Chem. Phys. 104 (1996) 2813.

[5] R.J. Leroy, University of Waterloo Chemical Physics Research CP-663, 2007.

[6] M. Musial, S.A. Kucharski, First Principle Calculations of the Potential Energy Curves of the Potential Energy Curves for Electronic States of the Lithium dimer, Journal of Theory and Computation 10 (2014) 1200-1211.

[7] B. Barakat, R. Bacis, F. Carrot, S. Churassy, P. Crozet, F. Martin, J. Verges, Chemical Physics 102 (1986) 215-227.

[8] R.A. Bernheim, L.P. Gold, P.B. Kelly, C. Tomczyk, D.K. Veirs, The Journal of Chemical Physics 74 (1981) 3249-3254.

[9] R.A. Bernheim, L.P. Gold, P.B. Kelly, T. Tipton, D.K. Veirs, The Journal of Chemical Physics 76 (1982) 57-60.

[10] R.A. Bernheim, L.P. Gold, C.A. Tomczyk, C.R. Vidal, The Journal of Chemical Physics 87 (1987) 861-868.

[11] S. Antonova, G. Lazarov, K. Urbanski, A.M. Lyyra, L. Li, G.-H. Jeung, W.C. Stwalley, The Journal of Chemical Physics 112 (2000) 7080-7088.

[12] M. Song, P. Yi, X. Dai, Y. Liu, L. Li, G.H. Jeung, Journal of Molecular Spectroscopy 215 (2002) 251-261.

[13] S. Magnier, Personal Communication, Lille University of Science and Technology.

[14] Robert J. Le Roy, G.T. Kraemer, BCONT 2.2 A computer Program for Calculating Bound to Continuum Transition Intensities for Diatomic Molecules, University of Waterloo, 2002.

CHAPTER 6

CONCLUSIONS

6.1 Summary of Work

In this dissertation, I included three main studies I carried out. The experimental study of transition dipole moments was explained at length in Chapter 3. It included determination of the transition dipole moment matrix elements for the $5^1\Sigma_g^+ \rightarrow A^1\Sigma_u^+$ and $6^1\Sigma_g^+ \rightarrow A^1\Sigma_u^+$ transitions of sodium dimer molecule. By combining the Autler-Townes and resolved fluorescence methods, I determined the absolute transition dipole moment matrix elements, carried out both R-Centroid and multivariable fits and constructed the transition dipole moment functions for both transitions depicting for the inner-well behavior. Chapter 4 focused on the calculation of radiative lifetimes and transition dipole moment matrix elements (TDMs) of ion-pair states of sodium dimer. This work has been published in the Journal of Chemical Physics **143**, 104304 (2015). Chapter 5 detailed my study on the lifetimes and transition dipole moment matrix elements calculations of lithium dimer molecule. In this work I have also counted the bound-to-continuum transitions by combining LEVEL 8.0 and BCONT 2.2 programs.